AN ABSTRACT OF THE DISSERTATION OF

Kyle J Gallagher for the degree of Doctor of Philosophy in Medical Physics presented on June 22, 2017.

Title: In Silico Clinical Trial Comparing Predicted Subsequent Malignant Neoplasms in Photon versus Proton Therapy of a Pediatric Cohort with Intracranial Tumors

Abstract approved: _____

Krystina M. Tack Phillip J. Taddei

Background: The leading cause of death 20 years after treatment for children surviving a cancer of the central nervous system was from a subsequent malignant neoplasm (SMN) (1) . Although it was been shown that proton therapy considerably reduces the risk of a fatal SMN in children receiving craniospinal irradiation compared to photon therapy, it has not been studied for intracranial tumors. We hypothesized that proton therapy in a high-income country would provide no benefit in reducing the risk of a fatal SMN in children with intracranial tumors compared to photon therapy in a low- to middle-income country.

Methods: We performed an *in silico* clinical trial comparing photon and proton treatments, in which we tested whether a cohort of 7 pediatric patients with intracranial tumors would not have a statistically-significant difference in the lifetime attributable risk, LAR_{Total}, of a fatal SMN. These pediatric patients, ages 3-12, were treated at the American University of Beirut Medical

Center (AUBMC) using photon 3DCRT and were retrospectively selected for this study. The selection criteria included the diagnosis of a low grade localized brain tumor, age of 2-14 years old, availability of computed tomography image sets, and treatment plans constructed between January 1, 2009 to September 30, 2011. For the photon therapy arm, plans were adjusted slightly to conform to the current standard of care and boost fields were removed. For the proton therapy arm, treatment planning was performed at the University of Texas MD Anderson Cancer Center according to the standard of care for passive-scattering proton therapy. The respective clinically-commissioned treatment planning systems (TPSs) were used to calculate the therapeutic dose from photon and proton therapies. Due to missing anatomy in the patients' computed tomography (CT) simulations, supplemental anatomy using a computational phantom was fused to each patient for calculation of stray radiation dose in out-of-field organs and tissues. To estimate stray radiation dose in photon therapy, we made measurements in an anthropomorphic phantom and derived a relationship between absorbed dose and distance from the field edge. For proton therapy, the stray radiation of greatest concern was neutrons, and only neutron doses were considered. To account for neutrons produced in the patient, an analytical model was trained and validated using previous Monte Carlo simulations of two children who received intracranial proton therapy fields. To account for neutrons generated in the treatment unit, an analytical model from the literature was adjusted for clinical realism and validated using data from previously-published Monte Carlo simulations of the same two children. Equivalent doses were estimated using the respective radiation weighting factors for photons, protons, and neutrons. The equivalent doses from stray and therapeutic radiation were summed, and the mean equivalent dose in each organ and tissue, T, at risk for SMN was calculated. Lifetime attributable risk of mortality, LAR_T, from a SMN was determined for each cancer site using a widely applied model from the literature. The ratio ($LAR_{proton}/LAR_{photon}$) of the combined LAR_T of all cancer sites, LAR_{total}, was used to compare the two modalities.

Results: We observed that supplement phantoms combined with analytical models were sufficient for estimating stray radiation in missing out-of-field anatomy. The analytical model used to estimate stray radiation in photon therapy reproduced the 12-year-old boy's in-anthropomorphic phantom measurements with a *RMSD* of 0.75 cGy Gy^{-1}, i.e., 6.6% of the dose at the field edge. Additionally, the equivalent doses estimated by the internal neutron model

that we developed were within 13.5% of the Monte Carlo for distances between 3 cm to 10 cm and were within a factor of two for distances between 10 cm to 20 cm. The equivalent doses estimated by the external neutron analytical model that we adjusted for clinical realism deviated by less than a factor of two from the Monte Carlo results of two children with intracranial tumors. We observed that both the internal and external neutron analytical models were of sufficient accuracy for estimating dose from stray neutrons. For photon therapy, the largest mean organ equivalent doses were found in in the red bone marrow, remainder, skin, and thyroid and were greater than 0.8 Sv. This was true for proton therapy as well except for the thyroid for which the average equivalent dose across all patients was 0.337 ± 0.154 Sv. The main result of these studies was that we found that proton therapy reduced the risk of developing a fatal SMN in these pediatric patients for which the ratio of LAR_{total} was 0.75 ± 0.22. This led to the rejection of the null hypothesis (H_0: ratio of LAR_{total} =1) with a p-value of 0.011. The primary contributors to LAR_{total} were leukemia and other solid tumors for which the ratio of LAR_T were 0.80 ± 0.27 and 0.76 ± 0.26, respectively. In general, the ratio of LAR_T was less than one except for bladder cancer in all the children, ovarian and uterus cancers in the girls, and prostate cancer in the boys. However, the LAR_T for each of these cancer sites was small, i.e., less than 0.02%. Other observations included that the LAR_{total} decreased as the age of the children increased.

Conclusions: We conducted an *in silico* clinical trial that disproved our hypothesis and implicated that children treated with intracranial photon fields in low- to middle-income countries would have a statistically-significant reduced risk of a fatal SMN if they were instead treated with intracranial proton fields. Additionally, our findings from these studies suggest that applying supplemental anatomy and contours from generic computational phantoms and models of out-of-field dose may be used to determine organ doses in clinical and research radiotherapy studies when the actual patients' anatomies are not available. Furthermore, our methods demonstrated the feasibility of using commercial TPSs combined with analytical models to quantify therapeutic and stray radiation in proton and photon therapy. This ability introduces the possibility of quickly comparing different modalities or optimizing treatment plans to minimize long-term morbidities, such as SMNs. The internal neutron model that we developed as part of this study was most accurate within 10 cm of the treatment fields where

the internal neutron dose contributes the most to overall exposures. This model combined with the external neutron model, can be used to estimate the equivalent dose from stray neutrons produce in proton therapy with sufficient accuracy. Future work includes programming the analytical models used in this study as add-ons for commercial TPSs.

In Silico Clinical Trial Comparing Predicted Subsequent Malignant Neoplasms in Photon versus Proton Therapy of a Pediatric Cohort with Intracranial Tumors

by

Kyle J Gallagher

A DISSERTATION

submitted to

Oregon State University

in partial fulfillment of

the requirements for the

degree of

Doctor of Philosophy

Presented June 22, 2017

Commencement June 2018

Doctor of Philosophy dissertation of Kyle J Gallagher presented on June 22, 2017

APPROVED:

Major Professor, representing Medical Physics

Head of the Department of Nuclear Science and Engineering

Dean of the Graduate School

I understand that my dissertation will become part of the permanent collection of Oregon State University libraries. My signature below authorizes release of my dissertation to any reader upon request.

Kyle J Gallagher, Author

ACKNOWLEDGEMENTS

First of all, I am grateful for my co-advisors, particularly Dr. Tack and Dr. Taddei, and my committee, Dr. Tanyi, Dr. Zhang, and Dr. Unsworth.

I am also grateful for the Department of Radiation Medicine at OHSU, the Achievement Rewards for College Scientists Foundation, and OSU for funding me during this dissertation.

I am thankful for the graduate students and staff at OHSU, OSU, and AUB who have been my friends and helped me along the way. Additionally, I am grateful for my roommates in Corvallis (Jacob and Chris), Portland (Risto, Tim, Austin, Taylor, and Ross), and Beirut (Tarek, TJ, and Matt) who have been encouraging. I am also thankful for the Taddei family who hosted me while I was in Lebanon.

I am very thankful for my encouraging family and especially my wife and best friend, Andrea.

I am also thankful for God who has given me this opportunity, allowed me to meet these incredible people, and has sustained me.

CONTRIBUTION OF AUTHORS

Dr. Taddei was involved in the original conception of the project and mentored me on each study.

For Manuscript 1, Dr. Youssef, Dr. Ayoub, and Ms. Faghali selected the patient cohort. Ms. Faghali adjusted the photon plans to meet the current standard of care at the American University of Beirut Medical Center. Dr. Youssef performed the contours of the red bone marrow and approved the treatment plans. Ms. Nabha and Mr. Tannous participated in the dosimetric measurements. Dr. Jalbout provided physics support and was involved with the conception of the study. Each author provided scientific expertise.

For Manuscript 4, Ms. Georges constructed the proton treatment plans. Dr. Mahajan approved the treatment plans and provided scientific expertise.

TABLE OF CONTENTS

TABLE OF CONTENTS (Continued)

Page

TABLE OF CONTENTS (Continued)

Page

TABLE OF CONTENTS (Continued)

Page

TABLE OF CONTENTS (Continued)

Page

TABLE OF CONTENTS (Continued)

LIST OF FIGURES

LIST OF FIGURES (Continued)

Figure Page

LIST OF TABLES

Table | Page

LIST OF TABLES (Continued)

Table Page

0.0 INTRODUCTION

0.1 Hypothesis

The objective of this dissertation was to test our hypothesis. The hypothesis was that passive-scattering proton therapy (PSPT) for children with low-grade localized brain tumors (LBTs) adhering to the standard of care in a high-income country (HIC) would not have a statistically-significant reduction in the lifetime attributable risk (*LAR*) of a fatal subsequent malignant neoplasm (SMN) compared to children receiving photon three-dimensional conformal radiation therapy (3DCRT) in a low- to middle-income country (LMIC). To test this hypothesis, we conducted a virtual clinical trial on pediatric patients who previously received photon 3DCRT at the American University of Beirut Medical Center (AUBMC) for low-grade LBTs. Specifically, we compared their predicted *LAR* of fatality from SMNs after undergoing 3DCRT at AUBMC versus the risks had they received PSPT at the University of Texas MD Anderson Cancer Center.

0.2 Motivation

Approximately 1 in 285 children in the United States will be diagnosed with cancer before the age of 20 (2). From 1975 to 2010, there have been major improvements in treating children with cancer for which the death rates for all childhood and adolescent cancers have declined by more than 50% (2). In 2014, the five year survival rate was estimated to be 81.3% for boys and 82.0% for girls ages 0-14 observed with cancer between 2003 and 2009 (2). Despite this encouraging increase in survival, many of the childhood cancer survivors face adverse late effects from the treatment of the primary cancer. Radiation therapy is often incorporated into the treatment regime, and has been a contributor to the long-term success of therapy. Unfortunately, it has also added to debilitating late effects such as late mortality, SMNs, obesity, cardiac dysfunction, pulmonary dysfunction, thyroid dysfunction and other chronic health issues for which SMNs are the greatest cause of death twenty to thirty years from the diagnosis of the primary cancer (3). Children are at an increased risk of radiation-induced late effects compared to adults due to their radiosensitive organs, smaller bodies causing their organs to be closer to the field of treatment, and longer life expectancy allowing for more time for adverse late effects to development. In comparison to adults, children are 5-10 times more likely to develop a SMN from the same absorbed dose (4). Therefore, establishing dose-response relationships and

predicting adverse late effects is essential for children with good long-term prognoses who might benefit from alternative treatment modalities. This is even more important for children who undergo radiotherapy in countries that lack medical resources, such as LMICs.

In this dissertation, we decided to study the disparity of treating children with cancer in a LMIC with photon therapy versus in a HIC with proton therapy. We were motivated by the global burden from cancer for which 84% of all childhood cancers occur in developing countries (5). Furthermore, 60% of all deaths from cancer take place in LMIC countries (2). In our study, the American University of Beirut Medical Center in Lebanon was selected to represent the institution located in the LMIC. Although AUBMC is considered a premiere research institution in the Middle East, medical resources are limited compared to a HIC. For example, neither this institution nor the Middle East has access to a proton facility.

Epidemiological studies that aim to establish does-response relationships for late-effects require accurate and efficient dosimetry methods to estimate the absorbed dose in organs and tissues at risk for late effects both inside and outside the primary field of radiation. However, in the treatment of the primary cancer, absorbed dose in organs inside and near the field of treatment are the major concern, generally neglecting the dose calculation of organs distant from the field of treatment. This can lead to missing or inaccurate estimates of absorbed dose in out-of-field organs for which accurate estimates are often necessary in long-term epidemiological studies. For example, the computed tomography (CT) simulation used for treatment planning and dose calculation is limited to only the relevant anatomy. This limitation is made to reduce the dose to the patient from the diagnostic procedure.

Additional and unique dosimetric challenges exist for both photon and proton therapies. In photon radiotherapy, even if the organ of interest is contained within the CT simulation images, the treatment planning system (TPS) has been shown to inaccurately determine the out-of-field dose, i.e. the region beyond the 50% isodose surface (6–13). In the study by Howell *et al* (7), the commercial TPS systematically underestimated the out-of-field dose by 40% on average. Similarly, Taddei *et al* showed the commercial TPS at two different institutions to systematically underestimate the out-of-field dose. Other dosimetric challenges occur for proton therapy. Most importantly, the dose from secondary neutrons are not

considered by the TPS and yet have been observed to be the most significant contributor to out-of-field dose (14–19).

In this dissertation, we have addressed these dosimetric challenges and presented a straightforward dose reconstruction method for clinical, scientific, and epidemiological studies. The goal of our study was to not only to test the hypothesis but also to motivate the need for new technologies and the improvement of current modalities in order to minimize the risk of late effects when treating children with cancer. Additionally, we aimed to provide clinicians with a more detailed patient risk profile to help guide decisions regarding the course of treatment.

0.3 Background

0.3.1 Photon therapy and sources of stray radiation

In this section, we will briefly discuss the production of high-energy therapeutic photons used in photon therapy and the sources of stray radiation. Modern linear accelerators are used to produce high-energy electrons. In photon therapy, the high-energy electron beam is magnetically steered into a target in which the bremsstrahlung interaction generates x-rays for therapeutic use. These high-energy x-rays are first collimated by primary collimators and then usually flattened by a flattening filter. The flattened beam is then collimated by secondary collimators. In three-dimensional conformal radiation therapy (3DCRT) the beam is further collimated by field-defining multi-leaf collimators (MLCs). These MLCs take on the shape of the target volume in the beams-eye view. Treatment plans usually require multiple beam angles in order to achieve the prescription dose while sparing healthy organs at risk of acute and late effects. Additional to the therapeutic photon beam is stray radiation. The sources of stray radiation include photon leakage through the head of the machine, scatter from the MLCs, and scatter from within the patient (20). For photon beam energies greater than 10 megavoltage (MV), neutron production occurs. In this dissertation, photon energies were below 10 MV, and therefore, neutrons were not considered in the dosimetry for stray radiation.

0.3.2 Proton therapy and sources of stray radiation

High-energy protons are accelerated using either a cyclotron or synchrotron. The therapeutic proton beam energies used in this dissertation varied between 140 to 200 MeV. The high-

energy proton beam can be delivered using several different techniques of which two are briefly discussed in this section. The first is a magnetic scanning delivery system for which the high-energy proton beam is magnetically steered in the axial plane and its energy is varied in ordered to cover the target volume. This technique is often referred to as pencil beam scanning proton therapy (PBSPT) in this dissertation. The second technique is called passive-scattering proton therapy (PSPT), for which the high-energy proton beam is scattered and its energy is modulated using a mechanism such as a range modulator wheel or ridge filter. In this dissertation, the first scattering device of the proton beam-line was a scattering-power-compensated range modulator wheel, which was followed by a second scatterer. Next, the beam is collimated laterally to conform to the shape of the target volume using a beam-specific aperture, and conformed to the distal edge of the target volume using a beam-specific compensator. Stray radiation is also a produced in proton therapy. In PSPT, the stray radiation of most concern is neutrons (14), which are generated within the machine, i.e., external neutrons, and within the patient, i.e., internal neutrons. In PBSPT, the stray radiation of main concern is internal neutrons because the proton beam has less beam-shaping devices to interact with, which are the primary source of external neutrons (21,22). In this dissertation, PSPT was implemented, and therefore, external and internal neutrons were considered.

0.3.3 Long-term risk from radiation exposure

In this section, the long-term risk of SMNs from cranial radiation exposures and the BEIR VII risk model, which we used to predict this risk, is discussed.

0.3.3.1 Epidemiological studies for cranial irradiation

Long-term follow-up studies are necessary for studying the impacts of SMNs because radiation-induced solid cancers typically do not appear until 10 years after treatment. Furthermore, it has been shown that the incidence of SMNs continued to increase at 40 years after treatment (23). However, no studies with sufficient follow-up periods have been conducted for proton therapy. Therefore, in this sub-section, long-term follow-up epidemiological studies are summarized for photon cranial irradiation of children with the findings of the rate of mortality from a SMN. This is because in this dissertation we projected the risk of a fatal SMN in children receiving intracranial irradiation.

Ron *et al* (24) observed 10,834 children who were treated with superficial x-rays for

tinea capitis, for whom the average intracranial dose was 1.5 Gy. The mean age of the cohort was 7.1 years old and the average follow-up length was 26 years. They found that the relative risk of mortality from leukemia and head and neck cancers were 2.3 and 3, respectively. Relative risk was the rate of disease in the exposed divided by the rate of disease in the unexposed. In the Childhood Cancer Survivor Study (CCSS), 2,881 patients under 21 years old were observed for 30 years after treatment of a central nervous system (CNS) cancer. In an analysis of this cohort, Armstrong (1) reported a 3.7% incidence of fatality from a SMN. Notably, of these childhood survivors of a CNS cancer, 1,085 received radiation to the cranium, for which 674 received only cranial irradiation without spinal irradiation. Although some of these children received chemotherapy, Armstrong's statistical analysis demonstrated that chemotherapy was not a significant source for the incidence of SMNs.

0.3.3.2 BEIR VII risk model

Since the results from long-term follow-up studies are not available for comparing proton and photon therapies, risk models are necessary to estimate the risk of SMNs. In this dissertation, the BEIR VII risk model was used. Therefore, it is important to have an understanding of the dose range for which the BEIR VII risk model is applicable. The risk of cancer induction and mortality is less known for low doses (<50 mSv) and high doses (>2 Sv) (Figure 1) (25–27).

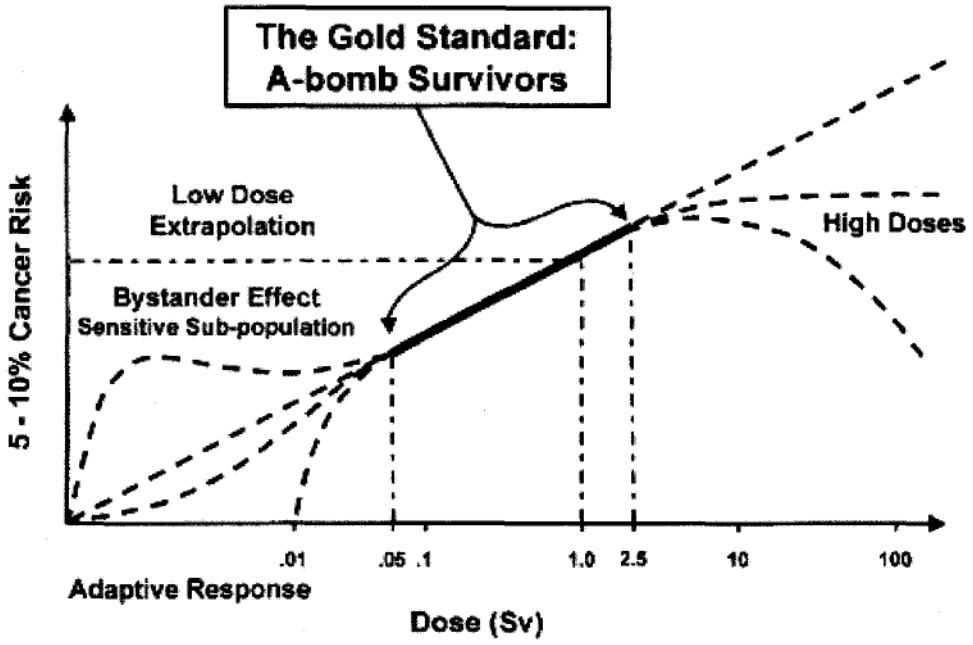

Figure 1. This figure is republished from Hall (2006) (25) with the permission of the publisher, and is illustrative in nature. It depicts the Life-Span Study (LSS) from the atomic bomb survivors as the "gold standard" data for cancer risk prediction. The dose-risk relationship is linear from 50 mSv to 2 Sv, but is unknown for low doses (<50 mSv) and high doses (>2 Sv). The dotted lines represent possibilities in the unknown regions. In the BEIR VII Report on Health Risks from Exposure to Low Levels of Ionizing Radiation, the National Research Council of the National Academies of Sciences has recommended the application of a linear no-threshold model for solid cancers and the linear-quadratic no-threshold model for leukemia as evidenced in the LSS (4). However, other theories including the bystander effect, adaptive response, and sensitive sub-populations implicate that the linear no-threshold model underestimates the risk of cancer. Contrasting theories, such as cell sterilization or dose threshold, imply that the linear no-threshold model overestimates the risk. The high dose region (>2 Sv) is also disputed where cell death begins to compete with cell mutation, which would cause the risk to plateau (i.e., some evidence for radiogenic lung and breast cancer reported by Sachs *et al* (28)) or exponentially decline (i.e., strong evidence at very high doses for radiogenic thyroid cancer reported by Diallo *et al* (29)). Nonetheless, clinical experience shows that most SMNs develop either in the near-field or in-field organs peripheral to the target volume (25,30,31).

The review and subsequent recommendations in the BEIR VII report utilized the atomic bomb survivor Life-Span Study (LSS) as the main source of data for assessing low doses of radiation and derivation of its recommended risk model (4) (Figure 1). They recommended a no-threshold linear model for solid cancers and a no-threshold linear-quadratic model for leukemia. These two models were fit with a dose range from 0 to 2 Sv by Preston *et al* (26). Outside of the specified dose range, the dose response relationship was less known and caution should be used for calculation of risk estimates. The atomic bomb survivor LSS was chosen by BEIR VII as its primary source of data because the LSS is viewed as the "gold standard" data set. This was because it included a large non-selected population of approximately 100,000 individuals consisting of a wide range of ages and both sexes. Additionally, a large subset of the individuals

(around 30,000) received low doses of radiation between 5 mSv to 100 mSv. Furthermore, the study quantified both cancer incidence and mortality for which the mortality follow-up was near completion for adult survivors and more than 50% complete for child survivors. Moreover, this ongoing study has continued for almost 70 years and received over 500 million dollars of funding.

0.3.3.2.1 Low dose region

The estimation of risk for low doses (<100 mSv) of radiation is less known. For acute low dose exposures, Brenner *et al* (27) has stated that statistically significant evidence for increased risk at low doses from human epidemiological data is available for doses above 50 mSv and reasonable evidence exists for doses above 5 mSv. They found that for protracted low dose exposures, statistically significant evidence exists for doses above 100 mSv and reasonable evidence exists for doses above 50 mSv. Preston *et al* (26,32) showed that the atomic bomb survivor LSS supports a linear no-threshold model for estimating the risk of mortality from solid cancers for low doses (0-150 mSv). Yet, for doses below 50 mSv, this model began to lose statistical significance (i.e., $p > 0.05$). This was shown in Figure 2 from Brenner *et al* (27). However, the uncertainty in the low dose region was less of a concern for this dissertation because the mean equivalent doses in organs at risk for SMNs in this study were generally above 100 mSv.

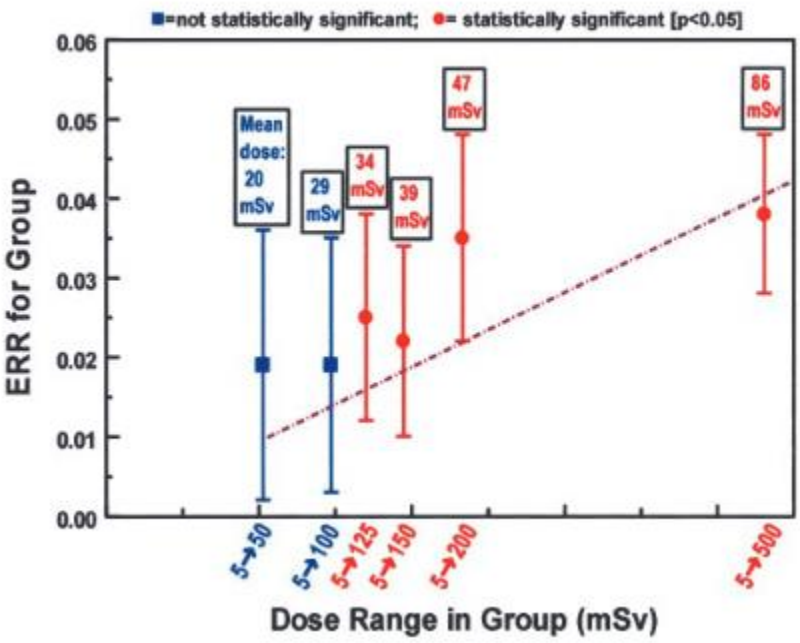

Figure 2. This figure is reprinted from Brenner *et al* (27) (Copyright [2003] National Academy of Sciences, U.S.A.). The estimated Excess Relative Risk (*ERR*) was plotted, with error bars representing ± 1 standard error, for fatality from solid cancers versus equivalent dose, observed from 1950-1997, in the atomic bomb survivor LSS cohort who were exposed to doses below 500 mSv (32). The *ERR* was the rate of disease in the exposed divided by the rate of disease in the unexposed subtracted by unity. The data was grouped into subsets such that increasingly larger maximum doses were incorporated. Above each group the mean dose was recorded. In the first two groups (blue), the correlation of the increased estimates of *ERR* with dose were shown not to be statistically significant when compared to the control cohort who were exposed to less than 5 mSv ($p = 0.15$ and $p = 0.3$). However, the remaining groups (red) estimates of *ERR* were shown to be statistically significant ($p < 0.05$). The dashed red line depicted the linear fit to all data from 5 to 4,000 mSv for which the higher doses were not shown in this graph.

0.3.3.2.2 High dose region

In terms of the less known dose-response relationship in the high dose region, >2 Sv, it was anticipated that the risk of cancer induction will not continue to increase with dose but will plateau or exponentially decrease (33). This was because cell killing will begin to compete with cell mutation which will prevent carcinogenesis. Nonetheless, Curtis *et al* (34) studied women who underwent radiotherapy for endometrial cancer and observed that the risk for leukemia did not plateau until doses of 4-8 Gy. Similarly, other studies did not show a downturn in the risk of leukemia until doses exceeded 5-8 Gy (35,36). In contrast, Hawkins *et al* (37) found the relative risk for leukemia to continue to rise with increasing dose, for which the relative risks were 2.1 (1-499 cGy), 4.4 (400-999 cGy), 9.4 (1000-1499), and 19.8 (>1500 cGy). Their study observed 16,422 patients in Britain who survived at least one year after diagnosis of a childhood neoplasm between 1962 and 1983.

Further evidence from the literature supports the continued increase in risk of radiation-induced second cancers above 2 Sv for solid tumors. Sigurdson *et al* (29) examined a subset of children from the CCSS who received radiotherapy to the head, neck or upper thorax and observed the risk of thyroid cancer continued to increase up to 30 Gy, but then declined at greater doses. Additionally, Neglia *et al* (38) analyzed the CCSS cohort and observed the risk of radiation-induced glioma, meningioma, and all cancers of the central nervous system (CNS) continued to increase with dose up to 45 Gy. Sachs *et al* (28) also found that the *ERR* for radiation-induced lung and breast cancers continued to increase up to 40 Gy but plateaued at higher doses (28). Furthermore, Inskip *et al* (39) performed a female case-control study on the CCSS cohort and demonstrated an increase in risk of radiation-induced breast cancer for exposures up to 40 Gy. Addressing very high therapeutic doses, Tucker *et al* (40) observed a factor of 38.8 increase in the risk of radiation-induced bone sarcoma at doses greater than 60 Gy absorbed at the site of the bone cancer. In a systematic review of the epidemiology data, Berrington de Gonzalez *et al* (41) concluded that "carcinogenesis from fractionated high-dose exposures [i.e., more than 5 Gy] are generally consistent with current theoretical models," that were predominantly determined from low dose exposures experienced in the Japanese atomic bomb survivor cohort.

In this dissertation, it was anticipated that mean organ equivalent doses would range from 0 to 10 Sv, but the dose in some voxels would reach a maximum of 54 Sv. Nonetheless, Berrington de Gonzalez *et al* (41) review of the epidemiological data and the other summarized studies support that the risk prediction methods outlined in the BEIR VII Report would be reasonably applicable over the dose ranges expected in this *in silico* experiment.

0.3.4 Literature review of related studies

In this section, an overview of studies related to the dissertation is presented for which absorbed dose was used to predict the risk of SMNs in children.

In a study conducted by the collaborative efforts of the Massachusetts General Hospital (MGH) and Harvard School of Medicine, the risk from photon intensity modulated radiation therapy (IMRT) versus proton therapy for intracranial tumors in six patients were compared (15,42–44). However, they only considered the out-of-field dose region. The six patients in the cohort consisted of a 9-month-old boy, 4-year-old girl, 8-year-old girl, 11-year-old boy, 14-year-

old boy, and 39-year-old male, and were represented by age- and sex-specific whole body voxelized computational phantoms (45,46). The results of their study are summarized in Table 1. Depicted in Table 1 are the *LAR* for the sixth intracranial field utilized to treat the 8-year-old girl and 14-year-old boy patient.

Table 1. The values in this table are from Athar *et al* (15) and illustrates the *LAR* (%) between PSPT, IMRT, and PBSPT for the sixth field of the 8-year-old girl/14-year-old boy treated with a prescription dose of 54 Gy(RBE) to the cranial lesion. The organs at risk are listed in order of increasing distance from the treatment field.

	***LAR* (%)**		
Organs	**Passive scattered proton therapy**	**IMRT**	**Proton beam scanning**
Larynx	0.08/0.14	0.04/0.12	0.02/<0.01
Thyroid	1.39/0.15	0.64/0.06	0.18/0.01
Bronchi	0.68/0.23	0.17/0.13	0.03/0.03
Breasts EAR	0.78/–	0.33/–	0.04/–
Breasts ERR	0.45/–	0.19/–	0.02/–
Lungs	0.39/0.14	0.16/0.14	0.04/0.02
Esophagus	0.04/0.07	0.01/0.05	0.01/
Liver	0.01/0.01	0.01/0.03	<0.01/<0.01
Pancreas	0.04/0.01	0.09/0.18	0.01/<0.01
Kidneys	0.01/0.01	0.04/0.08	<0.01/<0.01
Uterus/prostate	<0.01/<0.01	0.01/0.01	<0.01/<0.01
Ovaries/testes	<0.01/<0.01	0.02/0.02	<0.01/<0.01
Bladder wall	<0.01/0.01	0.04/0.02	<0.01/<0.01

A trend in the data showed IMRT to reduce the risk of SMNs close to the field-edge compared to PSPT, whereas farther from the field-edge PSPT had lower risk than IMRT. This trend was seen in the 8-year-old girl for whom the *LAR* of thyroid cancer was 1.39% and 0.64% for PSPT and IMRT, respectively. Yet, farther from the field-edge, PSPT produced a significantly lower *LAR* for cancer induction compared to IMRT where the *LAR* of bladder cancer was <0.01% and 0.04% for PSPT and IMRT, respectively. There were limitations in the experimental design of Athar *et al* (15), upon which we sought to improve in this dissertation. First, we did not completely replace the patients' anatomies with those of generic computational phantoms. Instead, in this dissertation, the extent of the patients' original anatomies included in their planning CT image sets were maintained and only their missing anatomies were supplemented

by matched patients for whom sufficient CT image sets existed. Second, the standard of care for localized brain tumors at the LMIC institution of AUBMC was 3DCRT as whereas Athar and Paganetti used IMRT in their study. It was anticipated that the out-of-field dose, and consequentially the risk of SMNs in out-of-field organs, from IMRT could be a factor of 2-3 times greater than 3DCRT due to the increased number of Monitor Units (MUs) (47). Athar *et al* (15) used Monte Carlo to calculate the dose from IMRT in the representative computational phantoms. In order to account for the increased radiation leakage and scatter from the multileaf collimators (MLCs) a factor of 3.5 was applied to the scattered portion of the beam (i.e., the region outside the primary beam). Three and a half was the assumed average increase in MUs compared to 3DCRT. In contrast, we used the clinically commissioned TPS at AUBMC to calculate the in-field therapeutic dose from photon 3DCRT, and a measurement-based analytical model to calculate the out-of-field stray dose, which was previously developed by Taddei *et al* (11). Finally, the Athar *et al* (15) study compared circular treatment fields whereas this dissertation will analyze clinically-realistic shaped treatment fields.

There were also considerable differences between Athar *et al*'s (15) methods to estimate the risk of SMNs based on organ doses versus the methods used in this dissertation. First, the Athar *et al* (15) study examined incidence. In this dissertation, we chose to examine the risk of mortality from SMNs for the following reason. In general, cancers such as thyroid cancer and non-melanoma skin cancer (NMSC) may have high rates of incidence but low rates of mortality. For example, the rates of survival for thyroid cancer and NMSC are 90% and 99.8%, respectively (48). Thus, reporting incidence values rather than mortality values may distract the reader from the most meaningful findings. Second, the risks of leukemia and other solid tumors (i.e., subsequent brain tumors, meningiomas) were not estimated by Athar *et al* (15), which we expect would be major sources of risk for mortality from SMNs because the brain and cranial red bone marrow were located in or near the treatment fields.

More recently, the same group at MGH and the Harvard School of Medicine has further investigated patients with cranial and central spine tumors for the increased risk of SMNs developed in the in-field organs. Moteabbed *et al* (49) examined six patients with central brain tumors and compared the risk of developing radiation-induced soft tissue sarcoma, soft tissue carcinoma, and bone sarcoma from PSPT, PBSPT, IMRT, and volumetric modulated arc therapy

(VMAT). Their results indicated that *LAR* values for proton plans were on average factors between 1.3 and 4.6 less than those of photon plans in terms of developing cancer in soft tissue and factors between 3.5 and 9.5 less than those for developing bone sarcomas. Furthermore, they compared two different risk models and demonstrated that the ratio of lifetime attributable risks (*RLAR*) for cancer incidence was minimally impacted by the choice of risk model. Some limitations in their approach were that not all in-field SMNs were accounted for, such as leukemia or non-melanoma skin cancer, resulting in an underestimation in *LAR* values of unknown magnitude. In a study by Paganetti *et al* (50), clinical treatment volumes from actual patients having optic gliomas were contoured by a physician onto 4-year-old girl and 14-year-old boy computational phantoms. Both proton and IMRT treatment plans were constructed and the *LAR* of soft tissue sarcoma, soft tissue carcinoma, and bone sarcoma were evaluated. The *LAR*s were a factor of 2 higher for the IMRT treatment plan compared to the 3-field proton treatment plan for the 4-year-old girl and a factor of 2.5 higher for the 14-year-old boy. Additional to the limitations mentioned in the study by Moteabbed *et al* (49), the Paganetti *et al* (50) study neglected stray neutrons in the proton treatment dose calculation. The magnitude of the impact of this was unknown, but portions of the brain and cranium were located in the out-of-field region where the dose from secondary neutrons has shown to dominate.

Other researchers have also calculated the in-field absorbed dose to predict the risk of SMNs. Winkfield *et al* (51) examined the in-field incidence of subsequent brain tumors following radiation therapy for pituitary adenoma. Treatment plans were constructed using either IMRT, photon stereotactic radiotherapy (SRT), 2-field 3DCRT, 3-field 3DCRT or proton therapy. The SRT treatment plans involved six arcs and utilized circular cones to collimate the radiation beam. For all treatment techniques they applied a risk model developed by Schneider *et al* (52) which utilized the Organ Equivalent Dose (OED) and was based on the dose-volume histogram of the whole brain. The authors acknowledged having large 95% confidence intervals and concluded the excess number of second brain cancers per prescribed radiation treatment were approximately 20 for IMRT, 25 for SRT, 10 for 2-field 3DCRT, 18 for 3-field 3DCRT and 5 for proton therapy per 10,000 patients per year. This dissertation differed in that the risk of mortality was determined by models described in the BEIR VII Report for both in-field and out-of-field organs. Additionally, our risk projection excluded the absorbed dose in the clinical

tumor volume (CTV), whereas Winkfield *et al* (51) did not specify negating the high absorbed dose in the CTV, but implied the use of the whole brain contour. Inclusion of the CTV would result in an increased risk estimate compared to this dissertation. In a subsequent study employing similar methods, Arvold *et al* (53) investigated the incidence of radiation-induced intracranial tumors after IMRT, 3DCRT, or proton therapy for a cohort of ten patients with benign meningiomas. They found that proton therapy halved the mean risk compared to photon therapy. Analogously, Dennis *et al* (54) studied a cohort of eleven patients treated with low grade gliomas and reported the excess risk of subsequent intracranial tumors for IMRT were a factor of 2.2 higher than proton therapy.

In a previous study, Miralbell *et al* (55) examined a 7-year-old boy with parameningeal rhabdomyosarcoma (RMS) in the left paranasal sinus, and predicted the risk of cancer induction for 3DCRT, IMRT, PBSPT, and intensity modulated proton therapy (IMPT). This was done by contouring the brain and bone, and applying risk prediction models outlined in ICRP Publication 60 (48). The extents of the bone contours were not specified. Additionally, the authors excluded the dose in the planning target volume (PTV) from the risk estimation calculation. They found a reduction in risk for developing leukemia and sarcoma of a factor of 2.4 for IMPT in comparison to 3DCRT. The main limitation of this study, as well as the other in-field studies previously mentioned, was that whole-body dosimetry was not performed, even though the risk model that was applied assumes whole-body dosimetry. Whole-body dosimetry is important as Diallo *et al* (30) showed that 50% of all SMNs developed in tissues that received an equivalent dose of less than 2.5 Sieverts in the radiation treatment of children with solid tumors or lymphomas. Furthermore, Miralbell *et al* (55) utilized the respective treatment planning systems (TPSs) for dose calculation, and therefore, stray radiation was not considered. Although limited to only small portions of the brain and bone contours, this will be a considerable limitation for calculating the out-of-field dose from photon therapy as conventional TPSs are prone to underestimating the out-of-field dose (6–13).

Yet to be established in the literature was the assessment of 3DCRT in a LMIC compared to PSPT in a HIC for children with localized brain tumors in terms of predicted fatality from all known in-field and out-of-field SMNs accounting for both therapeutic and stray radiation. Although it was perceived that PSPT may significantly reduce the risk of SMNs due to less

integral dose (56), the out-field-dose in 3DCRT is not heightened from the increased number of MUs as in IMRT nor is it convoluted by secondary neutrons as experienced in PSPT. For this reason, we hypothesized that PSPT compared to 3DCRT would not significantly reduce the risk of a fatal SMN for children with localized brain tumors. This warranted further investigation for which we estimated the risk of a fatal SMN induction from 3DCRT versus PSPT for a set of children with localized brain tumors.

0.4 Dissertation structure

The dissertation is a compilation of four manuscripts as shown in Figure 3.

<table>
<tr><th colspan="2">Photon Therapy</th><th>Proton Therapy</th></tr>
<tr><td colspan="2"><u>Manuscript 1</u>
Calculated therapeutic dose using the treatment planning system
Used TLD measurements to re-parameterize an analytical model to calculate stray dose
Calculated stray dose using the analytical model</td><td><u>Manuscript 2</u>
Developed and validated internal neutron model for proton therapy</td><td><u>Manuscript 3</u>
Validated external neutron model for proton therapy from literature and adjusted for clinical realism</td></tr>
<tr><td colspan="3"><u>Manuscript 4</u>
Applied analytical models from Manuscripts 2 & 3 to calculate stray dose from proton therapy
Calculated the therapeutic dose from proton therapy using the treatment planning system
Estimated and compared the risk for mortality of SMNs using the calculated equivalent doses from photon (Manuscript 1) and proton therapies</td></tr>
</table>

Figure 3. Depicted above is a chart of the structure of the dissertation.

0.4.1 Manuscript 1

Manuscript 1 was titled “Supplemental computational phantoms to estimate out-of-field absorbed dose in photon radiotherapy” and calculated the dose from therapeutic and stray radiation in the pediatric cohort from photon 3DCRT. This manuscript was presented at the 2015 American Association of Medical Physicists in Medicine annual conference as a distinguished electronic poster. Additionally, it was submitted to the journal of Physics in Medicine and Biology and is currently under review.

0.4.2 Manuscript 2

Manuscript 2 was titled “Internal neutron analytical model for proton therapy of pediatric patients with intracranial tumors,” which developed and validated an internal neutron analytical model for proton therapy. This manuscript was accepted at the 2017 American Association of Medical Physicists in Medicine annual conference as a poster. Additionally, it was submitted to the International Journal of Particle Therapy and is currently under review.

0.4.3 Manuscript 3

Manuscript 3 was titled “Independent validation of an analytical model for equivalent dose produced in a passive-scattering proton therapy treatment unit.” This manuscript validated an external neutron analytical model from the literature (57) and adjusted it for clinical realism. We plan to submit this manuscript to the journal of Biomedical Physics & Engineering Express.

0.4.4 Manuscript 4

Manuscript 4 was titled “*In silico* retrospective clinical trial comparing predicted subsequent malignant neoplasms in photon versus proton therapy of a pediatric cohort with intracranial tumors.” This manuscript applied the analytical models from Manuscript 2 & 3 to estimate the stray neutron equivalent dose from proton therapy in the pediatric cohort. The therapeutic dose from proton therapy was calculated directly by the clinical TPS. Additionally, the risk of mortality from a SMN was estimated using the BEIR VII risk model for both photon (Manuscript 1) and proton therapies used to treat the pediatric cohort. We intend to submit this manuscript to the journal of Radiotherapy & Oncology.

1.0 Manuscript 1 – Supplemental computational phantoms to estimate out-of-field absorbed dose in photon radiotherapy

Kyle J Gallagher[1,2], Jaad Tannous[3], Racile Nabha[3], Joelle Ann Feghali[3], Zeina Ayoub[3], Wassim Jalbout[3], Bassem Youssef[3], Phillip J Taddei[1,3,4]

(1) Oregon State University, Corvallis, Oregon, (2) Oregon Health and Science University, Portland, Oregon, (3) American University of Beirut Medical Center, Beirut, Lebanon, (4) The University of Texas MD Anderson Cancer Center, Houston, Texas

1.1 Abstract

The purpose of this study was to develop a straightforward method of supplementing patient anatomy and estimating out-of-field absorbed dose for a cohort of pediatric radiotherapy patients with limited recorded anatomy. A cohort of nine children, aged 2 to 14 years, who received three-dimensional conformal radiotherapy for low grade localized brain tumors (LBTs), were randomly selected for this study. Because the extents of their computed tomography simulation image sets were cranial only, they were matched for sex, height, and mass with patients from a previous study with larger extents and for whom contours of organs at risk for radiogenic cancer had already been delineated. Rigid fusion was performed between the LBT patients' data and those of the supplemental computational phantoms using commercial software and in-house codes. In-field dose was calculated with a clinically-commissioned treatment planning system, and out-of-field dose was estimated with a previously-developed analytical model that was re-fit with parameters based on new measurements for intracranial radiotherapy. Mean doses greater than 1 Gy were found in the red bone marrow, remainder, thyroid, and skin of the patients in this study. Mean organ doses between 150 mGy and 1 Gy were observed in the breast tissue of the girls and lungs of all patients. Distant organs, i.e., prostate, bladder, uterus, and colon, received mean organ doses less than 150 mGy. The mean organ doses of the younger, smaller LBT patients (0 to 4 years old) were a factor of 2.4 greater than those of the older, larger patients (8 to 12 years old). Our findings demonstrated the feasibility of a straightforward method of applying supplemental computational phantoms and

dose calculation models to estimate absorbed dose for a set of children of various ages who received radiotherapy and for whom anatomies were largely missing in their original computed tomography simulations.

1.2 Introduction

Patients who receive radiotherapy are at risk for radiogenic subsequent malignant neoplasms (SMNs) and other late effects that can result in morbidity or mortality. Children who receive radiotherapy are at increased risk for SMNs compared to adults who receive radiotherapy because, in general, they have longer remaining lifetimes, are more sensitive to side effects from radiation, and have organs that are in closer proximity to the treatment fields (25). The late effect of greatest concern for childhood cancer survivors is a SMN (58). To predict the risk of a SMN in the radiotherapy setting or associate effects recorded in epidemiological data to radiation dose, absorbed dose must be estimated throughout patients' bodies. Two challenges hinder the estimation of absorbed doses in organs and tissues at risk of SMNs from radiotherapy. First, in most radiotherapy cases, only the anatomy near the target region is represented in their computed tomography (CT) simulation image sets, and anatomy farther away from the target region is not imaged. Second, although clinical treatment planning systems (TPSs) accurately calculate the dose within the treatment fields (59), they have been shown to inaccurately estimate the absorbed dose outside of the field edge, i.e., beyond the 50% isodose surface (7,8). Therefore, additional methods are needed for estimating out-of-field dose in organs and tissues.

Some methods have been developed to overcome these challenges. To address the missing patient anatomy, previous research studies have replaced entire patients' anatomies with surrogate generic phantoms (16–18,60). Out-of-field dose estimations have been made using specialized Monte Carlo simulation codes (6,61–67), analytical models (11,68–71), and measurements (20,60,72,73). For large cohorts both in-phantom measurements and detailed Monte Carlo simulations can be time consuming. In an effort to balance speed, accuracy, and available resources, Taddei *et al* (11) created an in-anthropomorphic measurement-based analytical model to accurately estimate the out-of-field dose for children receiving craniospinal irradiation (CSI). They later applied this model in subsequent studies that compared risks of

SMNs in proton versus photon CSI (74,75). This approach was innovative in that a computationally inexpensive and fast method to calculate out-of-field dose could be applied to many patients if missing anatomy were made available. However, in these studies, whole or nearly-whole patient anatomies were available in the CT image sets. Yet to be established was a simple method for supplementing missing patient anatomy and applying a dosimetric model such that the out-of-field organ and tissue doses could be estimated.

The purpose of this study was to develop a straightforward method of supplementing patient anatomy and estimating out-of-field absorbed dose for a cohort of radiotherapy patients with limited recorded anatomy. For nine children who received localized external-beam radiotherapy for intracranial lesions, we applied this method to estimate the absorbed dose in their organs and tissues at risk for SMNs. We supplemented the patients' existing anatomies captured in their planning CT image sets with those of patients having similar age, height, and mass but more complete CT image sets. In-field organ doses were taken directly from the TPS. Out-of-field absorbed doses were estimated using a previously-developed analytical model for absorbed dose versus distance from the composite field edge. Parameters for the model were re-fit based on new in-anthropomorphic-phantom measurements.

1.3 Methods and materials

1.3.1 Patient cohort and treatment planning

A cohort of nine pediatric patients treated for intracranial lesions in our clinic were selected under protocol of the American University of Beirut Medical Center's (AUBMC's) Institutional Review Board. The patients were chosen using the systematic random selection method (76) of the first five females and four males, sampling backwards chronologically who met the following criteria:

1) Diagnosed with a low grade localized brain tumor (LBT) such that they had a moderate to good probability of long-term survival
2) Treatments performed according to the standard of care at AUBMC which follows the guidelines of the National Comprehensive Cancer Network
3) Treatment plans constructed between January 1, 2009 to September 30, 2011
4) Availability of radiotherapy planning CT image sets
5) Ages distributed between 2 to 14 years old

The intent of radiotherapy for these LBT patients was to eradicate the primary tumor or eliminate residual cancer cells following surgical resection of the tumor. The diagnoses, gross tumor volumes (GTVs), and radiotherapy prescriptions of the selected patients are listed in Table 2. All diagnoses were low grade (grades 1 or 2) with the exception of three patients with anaplastic ependymoma, which are high grade tumors (grade 3). We included them because the number of patients with purely low grade tumors was insufficient, and also because patients with anaplastic ependymoma, despite having high grade tumors, have an acceptable long term survival (77).

Table 2. Listed below is each patient's cancer diagnosis, gross tumor volume (GTV), and prescribed dose. Patient index denotes each patient's sex and age in years. For example, the 2-year-old male was indexed as 2yom. Heights and masses of each patient and matched computational phantom are listed.

Patient index	Height (cm)	Mass (kg)	Diagnosis	GTV (cm^3)	Prescribed dose (Gy)	Phantom height (cm)	Phantom mass (kg)
2yom	88	10	Anaplastic Ependymoma	62.61	41.4	101	12.8
2.5yof	87	12	Ependymoma	40.53	50.4	85	11.9
3yof	103	21.5	Ependymoma	100.61	54	115	26.9
3.5yof	104	16	Anaplastic Ependymoma	83.50	45	115	26.9
4yof	103	18	Glioma	93.64	54	115	26.9
4yom	94	12	Pilocytic Astrocytoma	28.29	54	101	12.8
8yom	133	28.4	Glioma	33.12	54	130	29.6
12yof	135	39	Supra Sellar Germinoma	62.72	30.6	147	42.6
12yom	144	40	Anaplastic Ependymoma	36.09	50.4	130	29.6

The CT simulation image set and radiotherapy treatment plan for each patient was collected retrospectively from archives and imported into AUBMC's clinical TPS. For CT imaging, each patient had been placed in the head-first supine position, and the extent of the image acquisition was from the top of the head to a level that varied between patients from the neck to the shoulders. 6-megavoltage (MV) three-dimensional conformal radiation therapy (3DCRT) treatment plans were created using a commercial TPS (Panther version 5.01, Prowess Inc.,

Concord, California) that had been commissioned for clinical service at AUBMC. Absorbed dose was calculated using the collapsed cone convolution superposition algorithm (78) with heterogeneity correction. Unlike routine clinical practice for these tumors, for this research study, boost fields were not considered. To maintain consistency between patients, the treatment plan for each patient was normalized to a prescription of 54 Gy in the planning target volume (PTV), where the PTV was covered by the 95% isodose surface.

1.3.2 Supplemental computational phantoms

To estimate dose in missing anatomy, supplemental computational phantoms were fused to the CT image sets of the LBT patients. Each supplemental phantom consisted of a CT image set and structure set of a pediatric patient from a previous CSI study (75). Supplemental phantoms spanned all ages and both sexes of young children. A supplemental phantom of matching sex, height, and mass was assigned to each LBT patient (Table 2). The CT image sets of the computational phantoms extended from the top of the head to variable locations between the mid-thighs and the feet. A secondary advantage of fusing matched CT image sets and structure sets from the CSI study was that organs and tissues at risk for SMNs had been contoured. The two CT image sets were geometrically aligned through rigid fusion (79) using a commercial software (MIM Maestro™, version 6.3.2, MIM Software, Inc., Cleveland, Ohio) (MIM Software Inc. 2017).

A final structure set for each patient was derived from both the primary (LBT) and secondary (CSI) structure sets in the following manner. Portions of structures that were in the primary CT image set were contoured using the TPS. Contours for anatomy partially or fully outside the primary CT image set were extracted from the secondary CT image set but cutoff at the inferior edge of the primary CT image set. The result was a hybrid phantom comprising upper anatomy (contours from the patient) and lower anatomy (contours from the computational phantom). The final structure set consisted of the body, brain minus GTV, thyroid, red bone marrow, remainder, skin, breast tissue, lungs, liver, stomach, uterus, ovaries, prostate, testicles, bladder, and colon, which included the rectum. Contours for the body, skin, red bone marrow, and remainder comprised upper portions from the patient and lower portions from the computational phantom. The upper portions were taken directly from the contours of

the primary CT image set, and the lower portions were generated by using a Boolean subtraction of the specified contour (i.e., body, skin, red bone marrow, or remainder) of the secondary CT image set and the body contour of the primary CT image set.

1.3.3 Estimation of absorbed dose

The absorbed dose in each voxel, D_v, was estimated in- and out-of-field for each patient's anatomy. The in-field D_v values (i.e., from therapeutic radiation) were calculated using AUBMC's clinically-commissioned TPS, so that the in-field D_v was calculated to an uncertainty of the acceptable limit for clinical operations, i.e., within 5% of the prescribed dose (80).

The out-of-field D_v values were calculated by a previously developed measurement-based analytical model (11). The model calculated D_v as a function of distance from the field edge. In order to apply the model to this cohort of LBT patients, we re-fit the parameters based on original measurements for intracranial fields. The measurements are described in section 2.4 and the model fitting is detailed in section 2.6.

1.3.4 In-anthropomorphic phantom measurements

A male anthropomorphic phantom (ATOM® Adult Male 701, Computerized Imaging Reference Systems [CIRS], Inc., Norfolk Virginia) loaded with 248 thermoluminescent dosimeters (TLDs) was treated as if it was a pediatric patient with an intracranial lesion. This phantom was designed to resemble an adult male and consisted of tissue equivalent epoxy resins, which simulated the electron densities of bone, spinal cord, spinal disks, soft tissue, inflated lung, and brain (81). First, the anthropomorphic phantom underwent CT simulation where the acquisition was identical to the LBT cohort except the scan length extended from the top of the head to the thighs. Second, the treatment fields of the 12-year-old boy with anaplastic ependymoma (Table 3) were applied to the base of skull of the phantom. This patient's fields were chosen for the fitting of the model because his size was of the closest match to that of the anthropomorphic phantom. Additionally, in the phantom's treatment plan, a field-weighting calculation point was placed at the center of the PTV in the location of a TLD plug. This was done to verify that the therapeutic dose was delivered in the prescription point for each measurement run, which are described later in this section. Shown in Figure 4 are axial, coronal, and sagittal images from the CT simulation of the anthropomorphic phantom along with the dose distribution generated

from the applied treatment fields.

Table 3. Description of the 12-year-old boy's treatment plan (7 fields, 6 MV photon, 3DCRT).

Field	1	2	3	4	5	6	7
Monitor units	960	631	631	421	127	913	772
Gantry angle (degree)	320	73	118	73	73	305	273
Couch angle (degree)	90	0	305	0	0	0	0
Collimator angle (degree)	90	0	350	0	0	145	0
X1 jaw (cm)	3.9	-1	-2.9	-1	-0.9	4.3	11.3
X2 jaw (cm)	4	10.7	13	10.7	10.8	5.8	-1.2
Y1 jaw (cm)	5.5	10.5	6	10.5	10	-2.5	10.5
Y2 jaw (cm)	4	-1	2.5	-1	-1	12	-1
Effective square (cm)	7	8.9	7.6	7.8	6.9	7.4	7.9
Source-to-surface distance (cm)	93.1	93.4	91.9	93.4	93.4	92.9	92.7
Water equivalent depth of calculation point (cm)	16.34	10.21	10.82	10.21	10.21	10.34	8.07

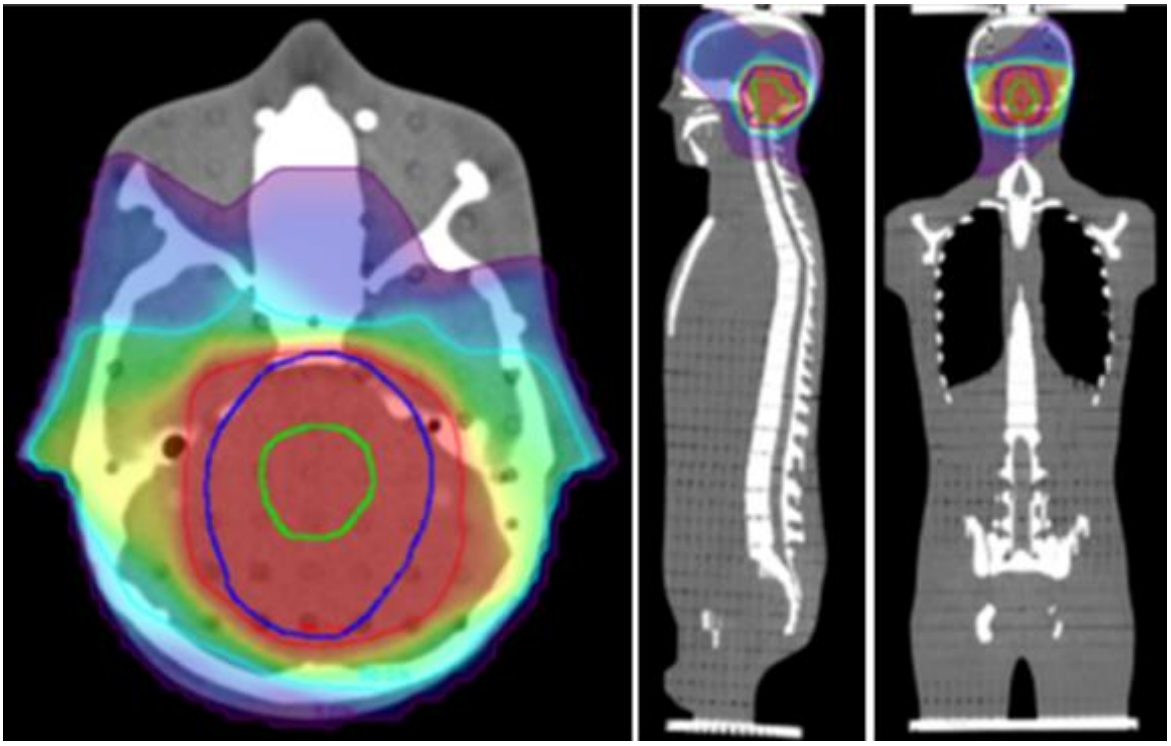

Figure 4. Dose distribution from applying the treatment fields of the 12-year-old boy to the anthropomorphic phantom, showing in axial (left), sagittal (middle), and coronal (right) planes superimposed on the CT images of the phantom. The colored lines depict the 95% isodose (red line), 50% isodose (light blue line), planning target volume (dark blue line), and gross tumor volume (green line) on the color wash.

The measurements were performed in two separate runs each delivered in a single setting. This was done to ensure that the dose readouts were within the range of high accuracy for the TLDs. Lithium fluoride TLD-100 powder capsules (Quantaflux Radiological Services, San Jose, California) were used and have been shown to be appropriate for measuring out-of-field absorbed dose in 6 MV photon radiotherapy with an uncertainty of less than 12% (11,82,83). In the first run, the monitor unit (MU) values calculated by the TPS were normalized to deliver 32.4 Gy in the calculation point, and TLDs were placed throughout and on the surface of the phantom. In the second run, in each location in which the dose fell below the useable dose range of the TLDs (i.e., below 25 cGy) a new TLD was placed, and the MUs were scaled to deliver 648 Gy at the calculation point (i.e., increased by a factor of 20). A photograph of the experimental setup is displayed in Figure 5. The TLDs were processed by certified technicians at MD Anderson's Imaging and Radiation Oncology Core and dose values were returned to us. Two or more background TLDs accompanied each set of irradiated TLDs from annealing to reading,

except that they were kept outside the treatment room while the others were irradiated. These TLDs were used to measure and subtract the background radiation. The absorbed dose in each TLD, $D_{TLD,i}$, in cGy at each location, i, was normalized to the prescription point dose of the associated run, D_{Rx}, in Gy, resulting in a TLD measurement at each location in terms of absorbed dose per therapeutic dose, $D_{TLD,i}/D_{Rx}$ in cGy Gy^{-1}. These measured data were the basis for the new fitting parameters for the double-Gaussian model.

Figure 5. The anthropomorphic phantom in the treatment position for the measurement.

1.3.5 Distance from the field edge for TLD measurements

To train our out-of-field dose model, measurements were made in a clinically-realistic scenario for a child receiving intracranial fields. The anthropomorphic phantom (ATOM® Adult Male 701, Computerized Imaging Reference Systems [CIRS], Inc., Norfolk Virginia) was designed to resemble an adult male with the height of 173 cm and mass of 73 kg. The phantom was divided

into 40 trans-axial slices each 2.5 cm thick. The trans-axial slices contained a matrix of 0.5 cm diameter detector plugs with 1.5 cm x 1.5 cm grid spacing. The phantom consisted of tissue equivalent epoxy resins which simulated the electron densities of bone, spinal cord, spinal disks, soft tissue, inflated lung, and brain (81). For the training of the analytical model, the phantom was treated as if it were one of the localized brain tumor patients. First, the phantom underwent CT simulation where the acquisition was identical to the localized brain tumor cohort except the scan length extended from the top of the cranium to the thighs. Second, the treatment fields of the 12-year-old boy with anaplastic ependymoma, as described in Table 3, were applied to the phantom.

1.3.6 Analytical model fitting

Following previously established methods (11), we used the new measured data to re-fit the parameters for 6 MV composite intracranial fields to the following equation:

$$D_v/D_{Rx} = \frac{\alpha_1}{\sqrt{2\pi\sigma_1}} e^{-\frac{(r-\mu_1)^2}{2\sigma_1^2}} + \frac{\alpha_2}{\sqrt{2\pi\sigma_2}} e^{-\frac{(r-\mu_2)^2}{2\sigma_2^2}}, \quad (1)$$

where μ_1 and μ_2 were the means of each Gaussian, σ_1 and σ_2 were the corresponding standard deviations of each Gaussian, and α_1 and α_2 were constants that scaled the corresponding magnitudes of each Gaussian. Least-squares fitting was performed using commercial software (Excel and the Solver Add-in, Microsoft, Redmond, Washington) where these six parameters were allowed to vary in order to minimize the root mean square deviation, *RMSD* (cGy Gy^{-1}), between the dose calculated by the model, $D_{model,i}$, and $D_{TLD,i}$ for n = 194 TLD locations. The equation for the *RMSD* is as follows:

$$RMSD = \sqrt{\frac{\sum_{i=1}^{n}\left(D_{model,i} - D_{TLD,i}\right)^2}{n}}. \quad (2)$$

All TLD locations outside of the composite field edge were included in the model with the following exceptions. First, TLDs near the field edge, r < 0.3 cm, where there is a large dose gradient, were excluded because the uncertainty in determining the TLDs' locations leads to higher uncertainties in dose. Second, due to the couch kick in the treatment plan, some TLDs that were located outside the composite 50% isodose surface received absorbed dose from the

primary beam. This would not have occurred in an actual patient's treatment plan, but it was an artifact from copying the patient's plan to the phantom. Therefore, we excluded these TLD data from the re-fitting procedure.

1.3.7 Correcting out-of-field dose in the dose matrices

For all voxels at distances where the out-of-field dose model more accurately estimated $D_{TLD,i}$ compared to the TPS's calculations, D_v calculated by the TPS was replaced with D_v calculated by the model, as had been done previously by Taddei *et al* (74). In this section, the methods are briefly described. First, the 50% isodose structure and the dose matrix were exported from the TPS as DICOM-RT Structure Set and DICOM-RT Dose files. Second, the dose value and Cartesian coordinates contained within each voxel of the dose matrix were read using in-house codes and commercial software (version R2014a, MATLAB, The MathWorks, Inc., Natick, Massachusetts) along with the coordinates of the vertices describing the polygon of the 50% isodose structure. Third, using parallel processing, the minimization of the Euclidean norm was used to determine the distance from the field edge and replace the TPS's calculated dose with the model's calculated dose for all distances where the model was resolved to be applicable. In the far out-of-field dose region, the TPS was inaccurate (11) and the model underestimated $D_{TLD,i}$; therefore, an average value from all TLDs in that range was applied.

1.3.8 Mean absorbed dose in organs, tissues, and target volumes

Mean absorbed dose, D_T, was determined for each organ and tissue, T, at risk for SMNs, the body, and each PTV. D_T was calculated directly for organs that were either completely in the primary or secondary CT image sets. For organs that were partially contained in both CT image sets (i.e., body, skin, red bone marrow, and remainder), D_T was determined using the volume-weighted average of the absorbed dose in the respective upper and lower contours. For organs that extended very far away from the treatment fields, at which portions were also not included in the supplemental anatomy—body, red bone marrow, remainder, and skin—the average absorbed doses were multiplied by the ratio of the mass of the CSI patient contained within the secondary CT image set and the LBT patient's actual mass at the time of CT simulation. This approximation assumes that the dose in these inferior regions is negligible compared to the superior anatomy.

1.3.9 Effective dose and risk of a SMN fatality

Effective dose, *E*, is a radiation protection quantity having tissue weighting factors, w_T, that relate to the proportional risk of stochastic effects, e.g., a radiation induced cancer fatality, as recommended by the International Commission on Radiological Protection (ICRP) (84). For each patient, the effective dose was calculated as

$$E = \sum_T w_T H_T \ \sum_T w_T w_R D_T, \quad (3)$$

where D_T was the mean absorbed dose from the given radiation type, *R*, in each tissue, *T*, and w_R was the radiation weighting factor (84). w_R accounts for the relative biological effectiveness of the given type of radiation and its energy, whereas w_T accounts for the given tissue's relative sensitivity to radiation. Because D_T was mainly from photon radiation incident on the patients' bodies, we applied the recommended w_R for photons of 1 (84). Values of w_T recommended by the ICRP for red bone marrow, lungs, breast tissue, colon (which includes the rectum), stomach, remainder, gonads (ovaries or testicles), thyroid, bladder, liver, esophagus, bone surface, skin, salivary glands, and brain are listed in Table 4 (84) and were applied directly to the organs and tissues in this study with the following exceptions. The first exception was that the normal brain tissue was defined as the brain minus the GTV in order to exclude cancerous tissue. The second exception was that the bone surface, salivary glands, and esophagus were included in the remainder volume and their w_T values were added to the w_T of the remainder.

Table 4. Tissue weighting factors, w_T, as defined by the ICRP in Publication 103 (84).

Organs and tissues	w_T
Bone marrow	0.12
Lung	0.12
Breast	0.12
Colon	0.12
Stomach	0.12
Remainder	0.12
Gonads	0.08
Thyroid	0.04
Bladder	0.04
Liver	0.04
Esophagus	0.04
Bone surface	0.01
Skin	0.01
Salivary glands	0.01
Brain	0.01

In order to put these quantities into perspective and motivate the need for further investigation, the excess lifetime risk of fatality from radiation-induced SMNs was estimated based on *E*. This was done by following the recommendation of the National Council on Radiation Protection and Measurements (NCRP) of 12.8% per Sv for girls and 8.1% per Sv for boys receiving these *E* (85).

1.4 Results

1.4.1 Analytical model fitting

The fitted analytical model is shown in Figure 6 along with $D_{TLD,i}/D_{Rx}$. Fitting parameters for the model are listed in

Table 5. The model was determined to be an improved estimation of $D_{TLD,i}/D_{Rx}$ compared to the

TPS for distances of 3 cm < $r \leq 50$ cm, in which the *RMSD* was 0.86 cGy Gy^{-1}, i.e., 7.6% of the dose at the field edge. At $r > 50$ cm, we applied an average $D_{TLD,i}/D_{Rx}$ of 0.0221 cGy Gy^{-1} rather than the model-determined value, which underestimated $D_{TLD,i}$ by 76%, on average. At $r \leq 3$ cm, the TPS value was applied (data not shown) because the model did not improve the estimate of $D_{TLD,i}/D_{Rx}$ near the field edge (11). Figure 6 depicts the applied analytical model for distances of 3 cm < $r \leq 50$ cm and the constant term of 0.0221 cGy Gy^{-1} for distances of $r > 50$ cm, which together produced a RMSD of 0.75 cGy Gy^{-1},i.e., 6.6% of the dose at the field edge. The distribution of D_v throughout the 8-year-old boy's anatomy and the computational phantom anatomy is shown in Figure 7. An example of an organ at risk in the moderate dose region is the thyroid, which is also shown in the figure. This image illustrates that in using the patient's original CT image set it was not possible to determine D_T in the thyroid, but after supplementing the anatomy below the inferior cutoff of the primary CT image set with that of the computational phantom, the thyroid dose could be estimated.

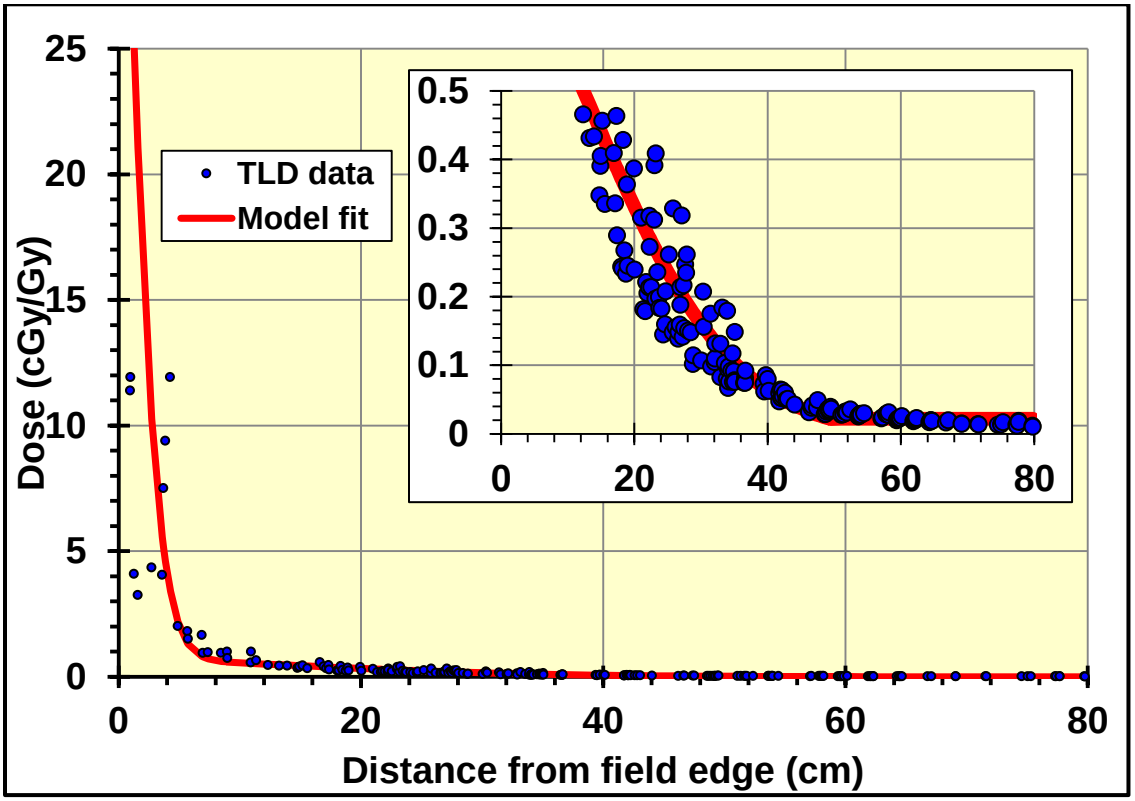
TLD data
Model fit
Dose (cGy/Gy)
Distance from field edge (cm)
0
5
10
15
20
25
0
20
40
60
80
0.1
0.2
0.3
0.4
0.5

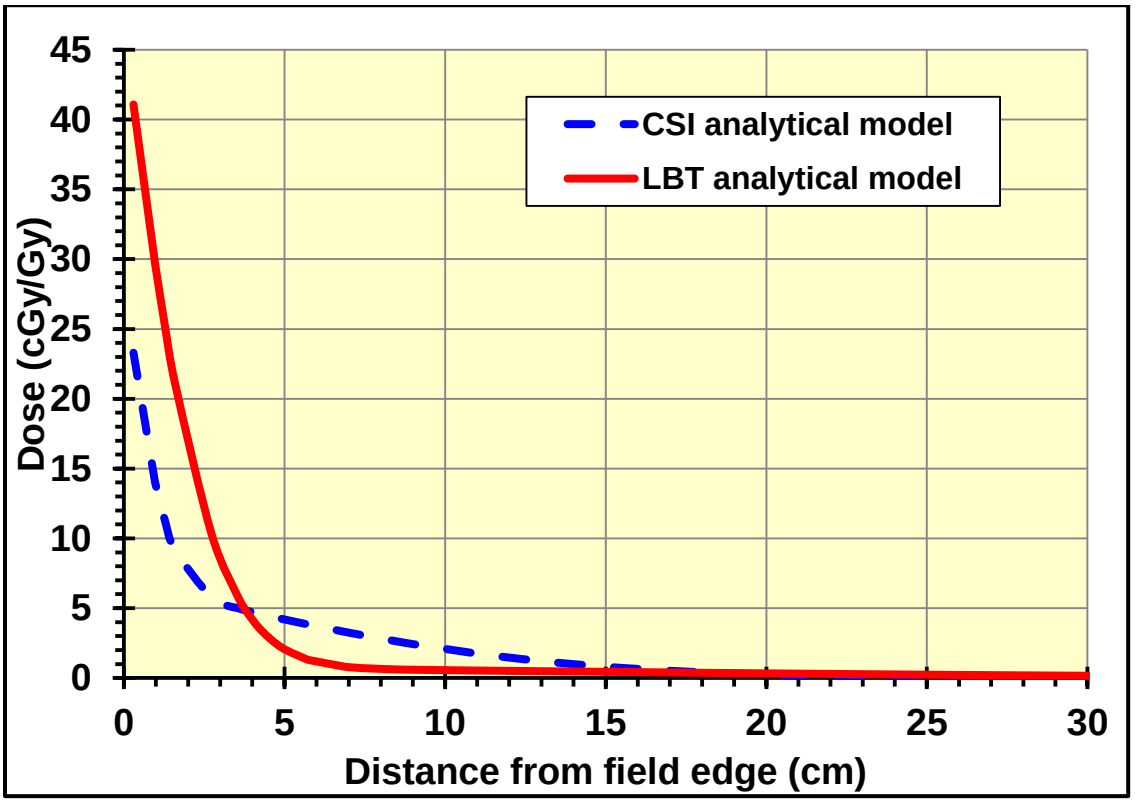
CSI analytical model
LBT analytical model
Dose (cGy/Gy)
Distance from field edge (cm)
0
5
10
15
20
25
30
35
40
45

Figure 6. The double-Gaussian model fit (red line) and the measured TLD data (blue circles) from the localized brain tumor treatment fields (upper). The analytical models of out-of-field dose versus distance to the field edge for the localized brain tumor (LBT) fields of the current study (solid line) and the craniospinal irradiation (CSI) fields of a previous study (75) (dashed line) (lower).

Table 5. Fitted parameters for the analytical model.

Parameter	Value
α_1 (cm cGy Gy^{-1})	771.6
μ_1 (cm)	-3.8
σ_1 (cm)	3
α_2 (cm cGy Gy^{-1})	46.3
μ_2 (cm)	-10
σ_2 (cm)	22

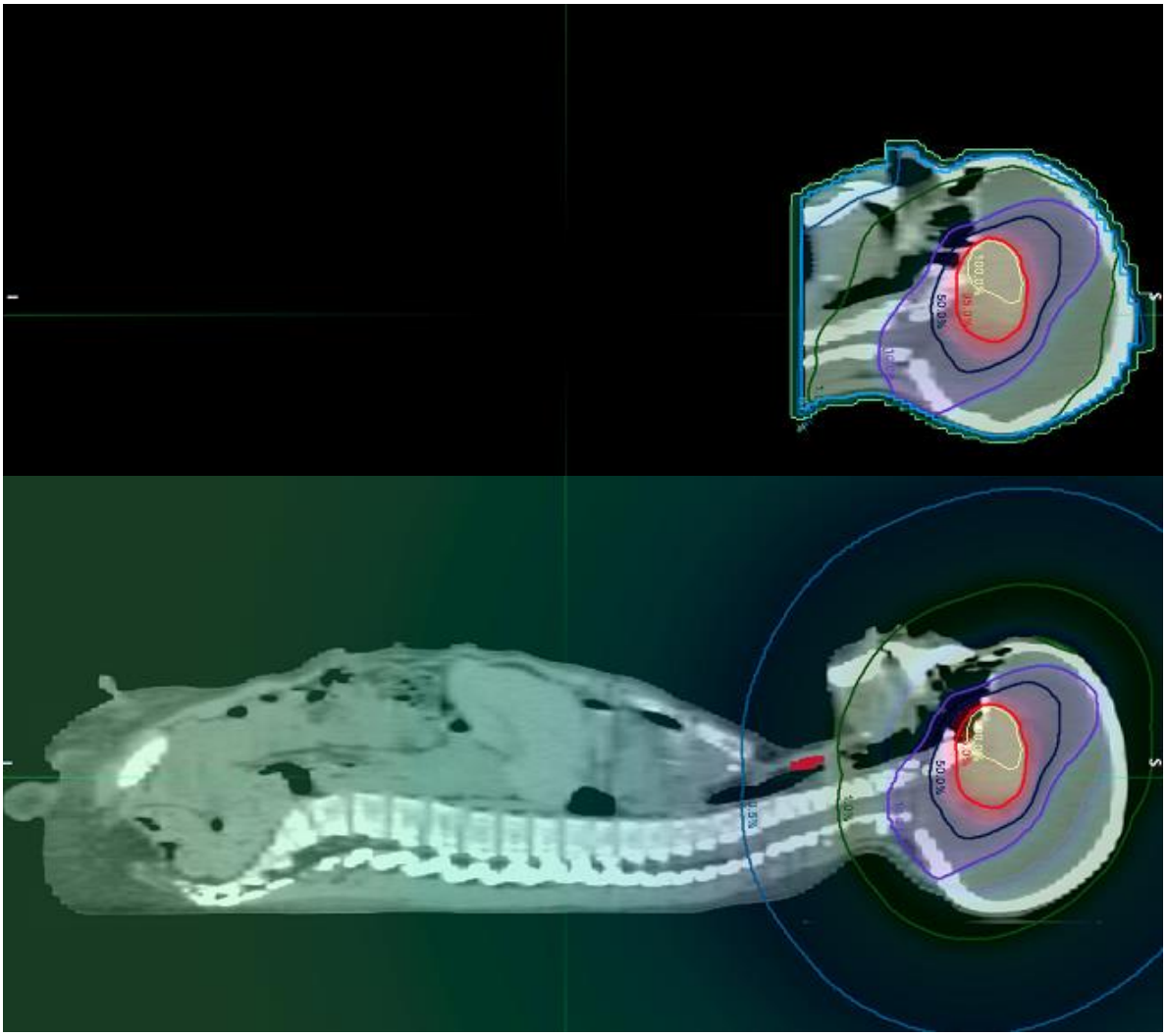

Figure 7. Shown are the sagittal views of the dose distribution from the primary fields of the 8-year-old boy on the original CT image set (upper), and the dose distribution from in-field (TPS) and out-of-field (model) components on the fused secondary CT image set (lower). The displayed isodose lines are 100% (yellow), 95% (red), 50% (black), 10% (purple), 1% (green), 0.5% (blue), and 0.1% (bright green). The location of the thyroid in the secondary image set is contoured in red (lower).

1.4.2 Mean absorbed dose in organs and tissues

Values of D_T are presented in

Table 6 along with the average D_T values across all nine patients. Mean doses greater than 1 Gy were found in the brain minus GTV, red bone marrow, remainder, thyroid, and skin of the patients in this study. Mean organ doses between 150 mGy and 1 Gy were observed in the breast tissue of the girls and lungs of all patients. Distant organs, i.e., prostate, bladder, uterus,

and colon, received mean organ doses less than 150 mGy.

Table 6. The mean absorbed doses (Gy) in organs and tissues at risk for SMNs for patients with localized brain tumors. These values were averaged across all localized brain tumor patients (Avg. LBT) and compared with those of a previous study of children who received craniospinal irradiation (Avg. CSI) (75). The doses were normalized to prescriptions of 54 Gy and 23.4 Gy for the LBT and CSI treatments, respectively.

Organs and tissues	2yom	2.5yof	3yof	3.5yof	4yof	4yom	8yom	12yof	12yom	Avg. LBT	Avg. CSI
Body	4.16	3.23	3.89	2.78	3.1	3.43	1.51	1.48	1.39	2.77	5.15
Bladder	0.06	0.07	0.02	0.03	0.02	0.06	0.01	0.01	0.02	0.03	2.12
Red bone marrow	5.57	7.56	5.72	5.52	8.22	7.18	6.38	4.2	1.59	5.77	5.84
Breast tissue	-	0.27	0.20	0.24	0.23	-	-	0.17	-	0.22	2.03
Liver	0.18	0.19	0.13	0.17	0.15	0.19	0.11	0.11	0.13	0.15	4.87
Lungs	0.29	0.28	0.19	0.24	0.21	0.3	0.2	0.21	0.23	0.24	3.76
Ovaries	-	0.07	0.02	0.03	0.06	-	-	0.01	-	0.04	1.72
Prostate	0.04	-	-	-	-	0.04	0.01	-	0.01	0.03	0.93
Remainder	2.04	1.49	1.09	1.09	0.8	2.06	0.45	0.67	0.9	1.18	5.76
Skin	1.21	1.37	1.86	0.86	1.11	1.14	0.52	0.64	0.5	1.02	2.67
Stomach	0.21	0.22	0.12	0.16	0.14	0.21	0.1	0.09	0.12	0.15	4.42
Thyroid	2.3	0.87	0.25	1.26	0.42	1.94	0.35	0.73	1.55	1.07	17.09
Uterus	-	0.07	0.02	0.03	0.02	-	-	0.01	-	0.03	1.5
Testicles	0.04	-	-	-	-	0.04	0.01	-	0.01	0.03	0.78
Colon	0.13	0.14	0.07	0.09	0.08	0.13	0.04	0.04	0.05	0.08	5.82
Brain minus GTV	23.49	17.43	27.72	20.06	30.86	18.42	21.66	27.48	17.79	22.77	-

On average, the mean organ doses of the girls in this study were a factor of 1.21 greater than the boys. Furthermore, the mean organ doses of the younger, smaller LBT patients (0 to 4 years old) were a factor of 2.4 greater, on average, than the older, larger patients (8 to 12 years old) in the cohort. For example, the average dose in the body was 3.43 Gy and 1.50 Gy for patients of 0 to 4 years old and 8 to 12 years old, respectively.

1.4.3 Effective dose

Values of *E* are listed in Table 7. *E* varied from 0.65 Sv to 1.60 Sv across all nine LBT patients. The average *E* for the girls was 1.31 Sv, and the average *E* for the boys was 1.21 Sv. In general, the average *E* was higher for the younger children of ages 0 to 4 years (1.44 Sv) than for the older children of ages 8 to 12 years (0.93 Sv).

Table 7. The effective dose in Sieverts (Sv) was calculated according to the recommended method of the International Commission on Radiological Protection (84) for each patient and averaged across all 9 patients.

Patient	Effective dose (Sv)
2yom	1.46
2.5yof	1.52
3yof	1.27
3.5yof	1.22
4yof	1.56
4yom	1.60
8yom	1.13
12yof	1.00
12yom	0.65
Average	1.27

1.5 Discussion

In this study, we applied supplemental anatomy, organ at risk contours, and a measurement-based model for out-of-field dose to a set of pediatric patients with LBT treatment plans to determine doses in organs and tissues at risk for SMNs. For these pediatric patients, we found that the mean organ doses to be non-negligible in the red bone marrow, remainder, thyroid, skin, breast tissue, lungs, and healthy brain tissue. Among these organs and tissues at risk for SMNs, the mean organ doses were highest in the red bone marrow, remainder, thyroid, skin, and healthy brain tissue. Additionally, we observed the younger, smaller patients in our study to have an increased D_T compared to the older, larger patients which is a consequence of the smaller patients' organs and tissues being inherently closer to the field of treatment. We also observed that the girls in this study experienced a higher D_T compared to the boys. This increase

in D_T for the girls could be because the girls were younger and smaller on average compared to the boys. The average age of the girls was 5 years old and their average height was 106.4 cm, whereas the average age of the boys was 6.5 years old and their average height was 114.8 cm.

We found for these children receiving localized brain radiotherapy for intracranial lesions, E was 1.27 Sv, on average. As a first approximation, the effective doses corresponded to an excess lifetime risk of radiation-induced fatal cancer of 16.8% for the girls and 9.8% for the boys. That is, among survivors, 168 out of every 1000 girls and 98 out of every 1000 boys who undergo 3DCRT for LBTs as described in this study would experience fatalities from radiation-induced SMNs. Although these risks are not small, the benefit of treatment far outweighs the risk of death from radiation-induced SMNs.

We compared the results of our study to those of a Monte Carlo study by Athar *et al* (43) who estimated the out-of-field mean organ doses in five children with intracranial tumors. These children received 6 MV intensity modulated radiation therapy (IMRT) where their radiation fields were designed to be circular to match proton treatment fields. For the mean organ doses of the 12-year-old female examined in our study, near-field and intermediate out-of-field organs such as the thyroid and lungs were an order of magnitude higher than the mean organ doses of the 8-year-old female studied by Athar *et al* (43). Conversely, for the distant out-of-field organs, such as the uterus, the mean organ doses were an order of magnitude higher for the 8-year-old female in the Athar *et al* (43) study. This latter result could be expected because the far out-of-field dose in IMRT should be higher than 3DCRT due to the increased MUs, and therefore, increased head leakage which dominates the dose profile at far distances. Yet, for the near and intermediate out-of-field distances where scatter from within the patient and scatter from the collimator of the machine dominate the dose profile, we would expect the mean organ doses to be more similar. Deviation could be due to differences in the location of the primary cancer and, subsequently, the field edge. It could also be attributed to the differences in dosimetry methods. Athar *et al* (43) used computational phantoms and Monte Carlo to calculate dose. Additionally, because the Monte Carlo did not account for the head leakage nor the increased scatter radiation emanating from the multileaf collimators due to the greater number of MUs in IMRT compared to 3DCRT, the authors applied a factor of 3.5 to the scatter

portion of the beam. We view our measurement-based analytical model as an improvement to these dosimetry methods, because the measurement-based model has increased accuracy in determining out-of-field dose while requiring vastly less computational resources compared to detailed Monte Carlo simulations.

The out-of-field dose calculations in this study were computed in approximately 8 hours for each patient on a single CPU. Consequently, a workstation with 64-cores would require approximately 10 minutes to calculate each patient. Therefore, these methods could be applied in a routine clinical setting for pediatric patients whose dose in organs at risk for SMNs are not typically calculated.

We also found the mean organ doses for these pediatric LBT treatments to be less than those of a previous CSI study. In

Table 6, the average absorbed dose across all nine LBT patients is compared to a previous study examining the absorbed dose in pediatric regional CSI, where doses were normalized to the prescription of 23.4 Gy (75). Surprisingly, the mean red bone marrow doses were comparable between the two treatment sites where the average red bone marrow dose was 5.77 Gy and 5.84 Gy for the LBT and CSI patients, respectively. Otherwise, the CSI patients received generally higher mean organ doses compared to the LBT patients. In particular, the average thyroid dose across all CSI patients was 17.09 Gy compared to 1.07 Gy for the LBT patients. As anticipated, the LBT patients had minimal dose to the colon (0.08 Gy) compared to the CSI patients who received a significant dose (5.82 Gy). Although the CSI patients had higher mean organ doses, the LBT patients still received non-negligible doses that have implications for the risk of SMN development.

Our fitted parameters for the analytical model apply only to similar clinical treatment sites and environments. For dissimilar radiotherapy treatment plans or environments, the fitting parameters should be recalculated. Nevertheless, the methods developed in this study can be applied to any treatment site. This is made evident in comparing our analytical model for 3DCRT of intracranial tumors to that of craniospinal irradiation. The bottom panel of Figure 6 compares the out-of-field dose (cGy Gy^{-1}) determined by the respective analytical models for the

CSI (75) and LBT treatments. For the near field region, $r < 4$ cm, the calculated dose was much higher for the LBT analytical model. However, for the intermediate out-of-field region, 4 cm ≤ r < 20 cm, the analytical model for the LBT treatment estimated lower dose compared to the analytical model of the CSI treatment. For distances beyond 20 cm, head leakage becomes the main contributor of the out-of-field dose, and thus, the normalized out-of-field dose (cGy Gy^{-1}) calculated by the respective analytical models for the CSI and LBT treatments converge.

The measurement-based analytical model can also be compared to the out-of-field measured data in Task Group (TG) 36 of the American Association of Physicists in Medicine (20). The data that most closely matches our clinical setup is the 6 MV, jaw delimited 5 x 5 cm^2 field size, which was either measured with diodes or TLDs in a water or polystyrene phantom. In general, there was good agreement between the dose calculated by our out-of-field analytical model and the TG 36 measured data, where the model's dose was greater than the measured data by 10% at 10 cm, 25% at 20 cm, and 60% at 30 cm. However, the model's dose was less than the TG 36 measured data by 45% at 50 cm and greater by 5% at 70 cm. Overall, this is excellent agreement considering the large variability in measured out-of-field dose (86). Discrepancies could be due to the differences in the measurement environment of the TG 36 dataset, such as the linear accelerator's shielding design, the lack of tertiary multileaf collimators, and the water equivalent medium used for measurement.

The methods used in this study were prototypical in nature and can be further developed for automation and clinical or research implementation. First, we anticipate being able to better match patients in the future by accruing more computational phantoms, i.e., anonymized patients with full CT simulation image sets and structure sets. This is possible because the feasibility of automatically anonymizing patients' DICOM-RT files while maintaining data integrity has been demonstrated by Newhauser *et al* (87). Additionally, it is possible to use automatized workflows in MIM, and other commercial software, to perform all Boolean operations immediately following the rigid fusion. This rapidly creates all new contours that are needed for supplementing missing anatomy with the computational phantom. Therefore, it would be feasible to apply these methods to a large number of patients. The potential for automation of our methods establishes the prospect of including stray radiation and

determining dose in organs at risk for late effects throughout low-dose regions of the body routinely, either in clinical or research studies. We perceive combining these methods with long-term patient follow-ups will improve risk prediction models and our understanding of dose-response relationships for children receiving radiotherapy.

This study had the following limitations. First, a systematic error could arise from an increased or decreased percent red bone marrow content in the cranium of the LBT patients compared to patients of similar age or those predicted by Cristy's mathematical model (88). Higher percent red bone marrow content in the cranium would result in an increased mean red bone marrow dose and an inflated predicted risk of leukemia. This is problematic for researchers who aim to use this cohort, or cohorts like it, to establish dose-response relationships, conjecture absolute risk estimates, or compare treatment modalities. To limit this potential systematic bias, the same physician contoured the CSI patients and the localized brain tumor patients using identical methods (Taddei *et al*, manuscript in preparation). We also compared the percent red bone marrow content in the cranium of the CSI patients to Cristy's mathematical model. We observed a slightly higher percent red bone marrow content in the cranium and mandible region for these patients. In a recent study, it was found using magnetic resonance imaging that a cohort of pediatric patients also had a similar higher percent red bone marrow content in the cranium and mandible compared to Cristy's mathematical model (Abu Gheida *et al*, manuscript in preparation). Second, we recognize the use of estimating risk based on effective dose is controversial and may not be applicable for medical applications (84,89) where the risk of developing SMNs has many factors including age at exposure, attained age, and sex. Furthermore, the NCRP risk coefficients used in this study (85) correspond to an age group of 0 to 19 years old whereas the oldest patient in this cohort was 12 years old. As younger children are at a higher risk of radiation-induced cancers (25), we would anticipate that these risk predictions are an underestimation of the true risk. Therefore, further investigation is warranted to more precisely quantify the risk of developing treatment related SMNs and motivates the need for new treatment techniques to reduce the radiation dose to these children.

1.6 Conclusions

We developed a straightforward method of applying supplemental computational phantoms and dose calculation models to estimate absorbed dose for a set of children of various ages who received radiotherapy and for whom anatomies were largely missing in their original CT simulations. These methods could be applied to any treatment site. Similar methods of applying supplemental anatomy and contours from generic computational phantoms and models of out-of-field dose may be used to determine organ doses in clinical and research radiotherapy studies when the actual patients' anatomies are not available.

1.7 Acknowledgements

We are grateful to the staff of MIM Software, Inc., for their technical support. Funding was provided in part by the Fogarty International Center (award K01TW008409), the Naef K. Basile Foundation, and the Portland Chapter of the Achievement Rewards for College Scientists. The content is solely the responsibility of the authors and does not necessarily represent the official views of the sponsors.

2.0 Manuscript 2 – Internal neutron analytical model for proton therapy of pediatric patients with intracranial tumors

Kyle J Gallagher[1,2] and Phillip J Taddei[3,4]

(1) Oregon State University, Corvallis, Oregon, (2) Oregon Health and Science University, Portland, Oregon, (3) American University of Beirut Medical Center, Beirut, Lebanon, (4) The University of Texas MD Anderson Cancer Center, Houston, Texas

2.1 Abstract

Purpose: To develop and test a universal analytical model to estimate for pediatric patients with intracranial tumors the equivalent dose from neutrons originating in their bodies during proton therapy.

Materials and Methods: We fit an analytical model to previously published internally-produced neutron equivalent dose (in mSv) per therapeutic absorbed dose (in Gy) as a function of distance from the field edge. The previous data were for three intracranial proton fields of a 9-year-old girl of nominal energies of either 160 MeV or 180 MeV. The model consisted of two components, each having double-Gaussian terms, one for lower energy (less than or equal to 160 MeV) and one for higher energy (greater than 160 MeV). Then we tested the model against similar previous data for a 10-year-old boy. As a figure of merit, we compared mean equivalent doses in organs at risk for subsequent malignant neoplasms between the analytical model result and those of the previously-published Monte Carlo calculations.

Results: The double-Gaussian relationship between equivalent dose and distance from the field edge was observed, having a root mean square deviation of 0.22 mSv/Gy for either the lower or higher energy component. In general, the model reproduced the neutron equivalent dose in the 10-year-old boy with sufficient accuracy. For distances between 3 cm to 10 cm, on average, the analytical model result was within 13.5% of the Monte Carlo. For 10 cm to 20 cm, the model overestimated the Monte Carlo by approximately a factor of two, and became less accurate

beyond 20 cm. Overall, the model provided a conservative estimate of the mean organ doses.

Conclusion: Our findings indicated that a computationally-efficient analytical model can be used with sufficient accuracy to estimate the equivalent dose from secondary neutrons originating inside children's bodies during proton therapy of intracranial tumors.

2.2 Introduction

By 2015, more than 131,000 patients had been treated with proton therapy worldwide (90). For certain treatment sites, proton therapy is becoming the modality of choice for pediatric patients. Across the United States between 2010 and 2012, among radiotherapy patients, the number of children treated with protons increased by 33% (91). The motivation of proton therapy for children is both to mitigate acute effects and lessen the risk or detriment of late effects in organs near the fields.

For children with intracranial or other tumors, among the late-effects of greatest concern are radiation-induced subsequent malignant neoplasms (SMNs) because of their associated morbidity and mortality. The Childhood Cancer Survivor Study found that fatalities after 20 to 30 years following the cancer treatment were attributed primarily to SMNs (3). SMNs emerge not only inside but outside the treatment field, where doses from stray (i.e., non-therapeutic) radiation dominate (30,92). Therefore, to estimate and ultimately design treatments to minimize these effects, it is essential to quantify the dose from stray radiation in organs and tissues at risk for SMNs.

In proton therapy, stray neutrons have enhanced damage capability because of their higher relative biological effectiveness (RBE) of detrimental effects, for example, carcinogenesis (93). These neutrons can be internally-produced in the bodies of patients (i.e., "internal neutrons") or in the treatment apparatus (i.e., "external neutrons"). Because they focus on accuracy within the treatment fields, modern treatment planning systems (TPSs) in the proton clinic currently do not account for the equivalent dose from stray neutrons. Detailed Monte Carlo simulations have been developed to quantify the equivalent dose from stray neutrons in certain environments (16,17,22,44,94–96). However, because it is computationally expensive, Monte Carlo has failed to be universally embraced, in particular, for estimating stray radiation

doses. Consequently, analytical models may be advantageous for estimates of stray radiation doses that are rudimentary but accurate and computationally inexpensive. Much work by others has gone into developing an analytical model for external neutrons in proton therapy (57,97–99). In contrast to external neutron models, which are highly dependent on the treatment apparatus and environment, an internal neutron model may be independent of environment and applied universally. To our knowledge, an analytical model for estimating dose from internal neutrons in proton therapy has not been developed.

The purpose of this study was to develop a computationally-efficient analytical model to estimate the equivalent dose from internal neutrons in proton therapy of children with intracranial tumors. To train and test our model, we used available Monte Carlo simulations from the literature of a 9-year-old girl and a 10-year-old boy who received passively-scattered proton radiotherapy for brain tumors (95,96). Our internal neutron model was trained using the Monte Carlo dataset of the girl, and for validation, the model was applied to the boy, where the results were compared to the respective Monte Carlo simulations. This model was not intended to be universal in all cases of proton therapy, but it is independent of treatment facility. We targeted the most common pediatric proton therapy treatment such that the model would apply in a large number of pediatric proton therapy cases (91).

2.3 Materials and methods

2.3.1 Prescription and treatment planning

The treatment plans of the 9-year-old girl and the 10-year-old boy were for intracranial boost fields to deliver a total of 23.4 Gy-RBE (100), or 21.3 Gy, in the clinical target volume using a passive scattering treatment unit. Their relevant field characteristics are summarized in Table 8. Because the girl's plan contained three fields and the boy's plan contained two fields and each field contributed equally, the prescribed absorbed dose for each field, D_{Rx}, was 7.09 Gy for the girl and 10.64 Gy for the boy. These treatment fields were similar to those of patients treated for low-grade localized brain tumors, such as astrocytomas and gliomas. Information regarding the computed tomography (CT) simulations, treatment plans, and Monte Carlo techniques were published previously (95,96). First, we trained the model based on data from the 9-year-old girl (see section 2.3). Then we tested the model based on data and results from the 10-year-old boy

(see section 2.4).

Table 8. Proton beam characteristics for the intracranial boost fields for the 9-year-old girl and 10-year-old boy in the previous study (95,96).

	Girl			Boy	
Pre-nozzle proton energy (MeV)	160	180	160	160	140
Beam orientation	LPO	PA	RPO	LPO	LL
Gantry angle (°)	97	180	263	130	90
Range in patient (cm of water H_2O)	12	13.5	12	11.3	9.2
SOBP width (cm)	8	8	8	7	6
Collimated field, major axis (cm)	6.6	7	6.3	11.8	11.6
Collimated field, minor axis (cm)	6.3	6.3	6.3	5.5	5.4
Air gap (cm)	23	29	23	2	2
Aperture thickness (cm)	4	6	4	4	4

Abbreviations: RPO (right posterior oblique), PA (posterior anterior), LPO (left posterior oblique), and LL (left lateral)

2.3.2 Distance from the field edge

The distance between the field edge (i.e., 50% isodose surface) and each out-of-field voxel, *r*, was determined prior to the fitting of the model. First, data in the Digital Imaging and Communications in Medicine (DICOM) standard format was read using in-house codes and commercial software (version R2016b, MATLAB, The MathWorks, Inc., Natick, Massachusetts). Next, for each field, the field edge was defined as the Cartesian coordinates corresponding to voxels with therapeutic absorbed dose, *D*, between $0.5\times D_{Rx}$ - 0.1 Gy and $0.5\times D_{Rx}$ + 0.1 Gy. Then, voxels in which *D* was less than $0.5\times D_{Rx}$ (3.55 Gy for the girl and 5.32 Gy for the boy) were defined as out-of-field. The Cartesian coordinates of these out-of-field voxels were recorded. Finally, we calculated the shortest distance between each out-of-field voxel and the field edge, *r*, using the Euclidean norm.

2.3.3 Training of the analytical model

Our proposed analytical model was trained using the previously-reported Monte Carlo data for the 9-year-old girl. The model had two components: One for lower energy fields having nominal energy, *E*, less than or equal to 160 MeV and one for higher energy fields having *E* greater than 160 MeV, for which *E* referred to the energy of the most distal Bragg peak of the multi-energetic beam. The lower energy and higher energy components were trained separately by data from

intracranial proton fields that were lower energy and higher energy, respectively. Each component was a double-Gaussian function that related the voxel's internal neutron equivalent dose, *H*, (in mSv) per D_{Rx} (in Gy) as a function of *r* (cm),

$$H/D_{Rx} = \begin{cases} \frac{\alpha_{L1}}{\sqrt{2\pi\sigma_{L1}^2}} e^{-\frac{(r-\mu_{L1})^2}{2\sigma_{L1}^2}} + \frac{\alpha_{L2}}{\sqrt{2\pi\sigma_{L2}^2}} e^{-\frac{(r-\mu_{L2})^2}{2\sigma_{L2}^2}}, & E \leq 160\ MeV \\ \frac{\alpha_{H1}}{\sqrt{2\pi\sigma_{H1}^2}} e^{-\frac{(r-\mu_{H1})^2}{2\sigma_{H1}^2}} + \frac{\alpha_{H2}}{\sqrt{2\pi\sigma_{H2}^2}} e^{-\frac{(r-\mu_{H2})^2}{2\sigma_{H2}^2}}, & E > 160\ MeV \end{cases}, \quad (1)$$

where the lower (L) and higher (H) energy components denoted the means, μ_1 and μ_2, standard deviations, σ_1 and σ_2, and amplitudes, α_1 and α_2, of each Gaussian term.

To train the model, least squares fitting was performed on each component by the commercial software, with all six fitting parameters varying to minimize the root mean square deviation, *RMSD*. Data for beams having nominal energies less than or equal to 160 MeV (i.e., right posterior oblique and left posterior oblique) were concatenated to create one dataset for the fitting procedure. Only voxels with $r \leq 49$ cm were used to fit the model parameters for the following reasons. Beyond this imposed upper limit, a large percentage of voxels were located at or near the girl's skin in her arms. Near the skin, volume averaging between tissue and air caused an artificial overestimation of H/D_{Rx}. In addition, before the artificial overestimation from volume averaging, the H/D_{Rx} values were very small (on average less than 0.009 mSv/Gy) at 49 cm from the field edge.

The following further considerations were made in training the model. To determine where to apply the model, we made new observations of the previously-published Monte Carlo results. Specifically, for these passively-scattered fields, we related equivalent dose per D_{Rx} versus *r* from each type of radiation, i.e., therapeutic protons, internal neutrons, and external neutrons, which were determined from the previous Monte Carlo simulations. For ease in viewing, the Monte Carlo data were averaged into 1-mm bins of *r*. Because two of her fields were of the same *E*, we combined the data for these two fields. We defined a lower limit of application of the model as the region for which H/D_{Rx} became meaningful, at greater than 25% of the therapeutic proton equivalent dose per D_{Rx}.

2.3.4 Preliminary validation of the analytical model

The fitted analytical model was tested as a preliminary validation against the previously-reported internal neutron Monte Carlo data of the 10-year-old boy. Then, the analytical model result was compared to the Monte Carlo result by averaging, as a figure of merit, the out-of-field H_T/D_{Rx} in organs and tissues at risk for a SMN, T, H_T/D_{Rx}, for the patient's treatment. T were selected based on the recommendations of the International Commission on Radiological Protection (ICRP) (48). For this out-of-field dose comparison, only organs beyond 3 cm from the field edge were considered. These T comprised out-of-field portions of the thyroid, esophagus, lungs, stomach, liver, colon (which included the rectum), bladder, and gonads.

2.4 Results

2.4.1 New observations of previously-published Monte Carlo results

The Monte Carlo data for the E = 160 MeV proton beams and the E = 180 MeV beam of the girl are plotted in Figure 8. For the 160 MeV and 180 MeV beams, therapeutic protons contributed the most to the total dose for $0 < r \leq 3.55$ cm and $0 < r \leq 3.85$ cm, respectively. Beyond these distances external neutrons were the main contributors. Beyond r = 3 cm, H_T/D_{Rx} values from internal neutrons exceeded 25% of the equivalent dose from therapeutic protons per D_{Rx}. For $r >$ 49 cm, where all voxels were from the girl's arms, volume averaging strongly influenced the H/D_{Rx} data. Only data for $r \leq 49$ cm were used to fit the model parameters (see section 2.3). Thus, the applicable region of the model was found to be 3 cm $< r \leq 49$ cm.

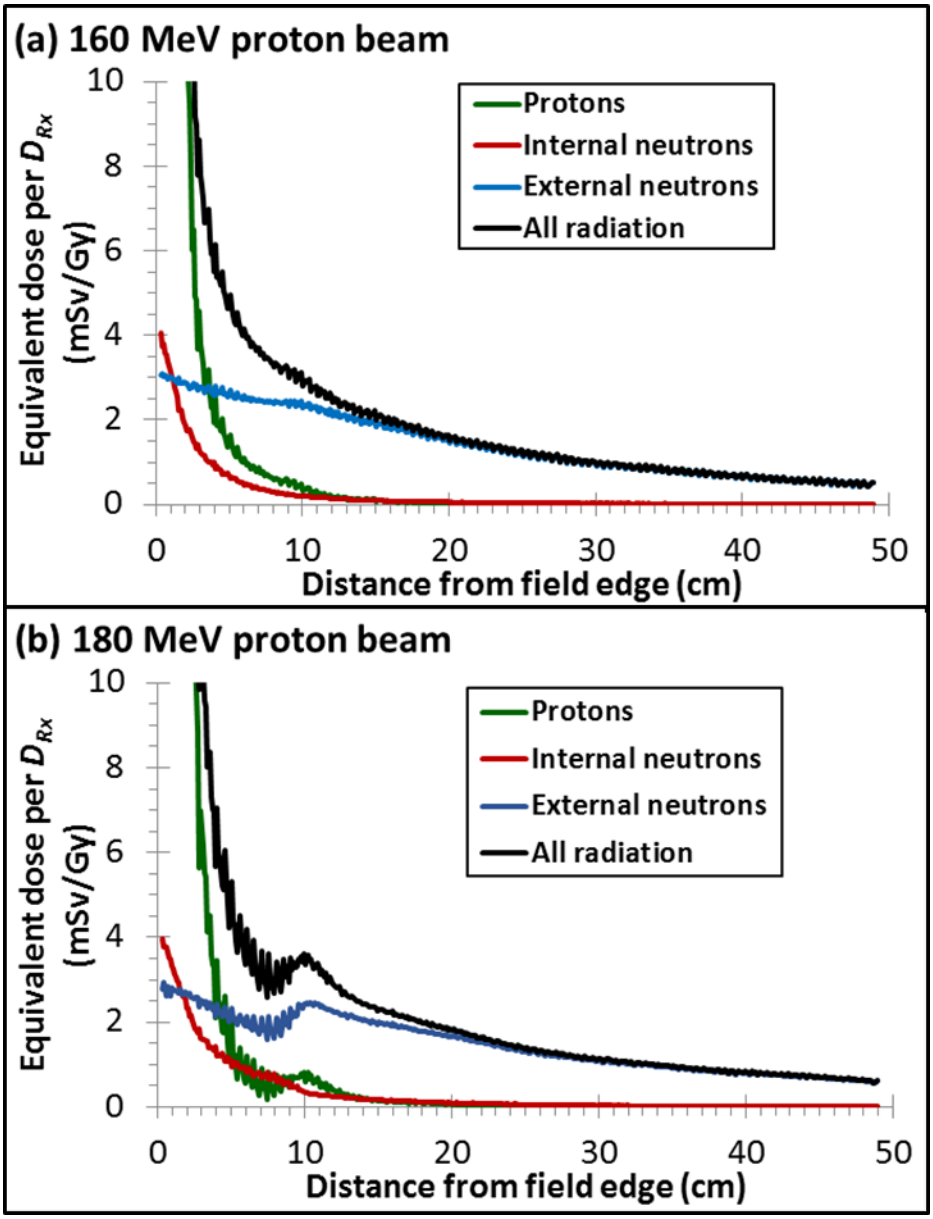

Figure 8. Equivalent dose per D_{Rx} from therapeutic protons (blue line), internal neutrons (red line), external neutrons (green line), and all radiation types (black line) for the Monte Carlo data that trained the lower energy component (a) and higher energy component (b) of the model. For clarity in viewing, the Monte Carlo data was averaged in 0.1-mm bins. Monte Carlo data were from Taddei *et al* (95).

2.4.2 Training of the analytical model

The double-Gaussian parameters were fit to the measured data separately for each component of the model. Parameter and *RMSD* values are listed in Table 9. We observed that the best fits resulted in each mean less than zero and both narrow and wide standard deviations. The *RMSD*

values were small, corresponding to less than 5.8% of the average H/D_{Rx} at the field edge.

Table 9. Fitted values of the parameters for the lower and higher energy components of the analytical model. Also listed for each component are the *RMSD* between the model values and the Monte Carlo values for each component.

Lower energy component		Higher energy component	
Parameter	**Value**	**Parameter**	**Value**
α_{H1} (cm mSv Gy^{-1})	1.080×10^5	α_{H1} (cm mSv Gy^{-1})	3.348×10^5
μ_{L1} (cm)	-36.08	μ_{H1} (cm)	-62.97
σ_{L1} (cm)	9.553	σ_{H1} (cm)	15.82
α_{L2} (cm mSv Gy^{-1})	3.739×10^5	α_{H2} (cm mSv Gy^{-1})	7.538×10^5
μ_{L2} (cm)	-201.1	μ_{H2} (cm)	-247.4
σ_{L2} (cm)	47.24	σ_{H2} (cm)	56.77
RMSD (mSv Gy^{-1})	0.2224	*RMSD* (mSv Gy^{-1})	0.2248

For the training data of the girl, the analytical model is plotted in Figure 9 along with the corresponding Monte Carlo data for internal neutrons. For easier viewing, the plots are shown on linear-linear and logarithmic-linear axes and the Monte Carlo data were averaged into bins. The Monte Carlo data matched the analytical model very well. For $3 < r < 10$ cm, the analytical model followed the Monte Carlo H/D_{Rx} closely as they decreased from 1.21 mSv/Gy to 0.19 mSv/Gy and 1.63 mSv/Gy to 0.40 mSv/Gy for the lower and higher energy components, respectively. For 20 cm $< r <$ 41 cm, both the analytical model and Monte Carlo data reduced from 0.05 mSv/Gy to 0.007 mSv/Gy and 0.09 mSv/Gy to 0.013 mSv/Gy for the lower energy and higher energy components, respectively. For $r \geq 41$ cm, the higher energy component underestimated the Monte Carlo data. However, H/D_{Rx} was very small beyond 41 cm (< 0.014 mSv/Gy), implying that the accuracy of the model was less critical in that region compared to $r <$ 41 cm. Everywhere in the applicable region of the model, $3 < r \leq 49$ cm, the higher energy component H/D_{Rx} was at least 30% higher than the lower energy component H/D_{Rx} .

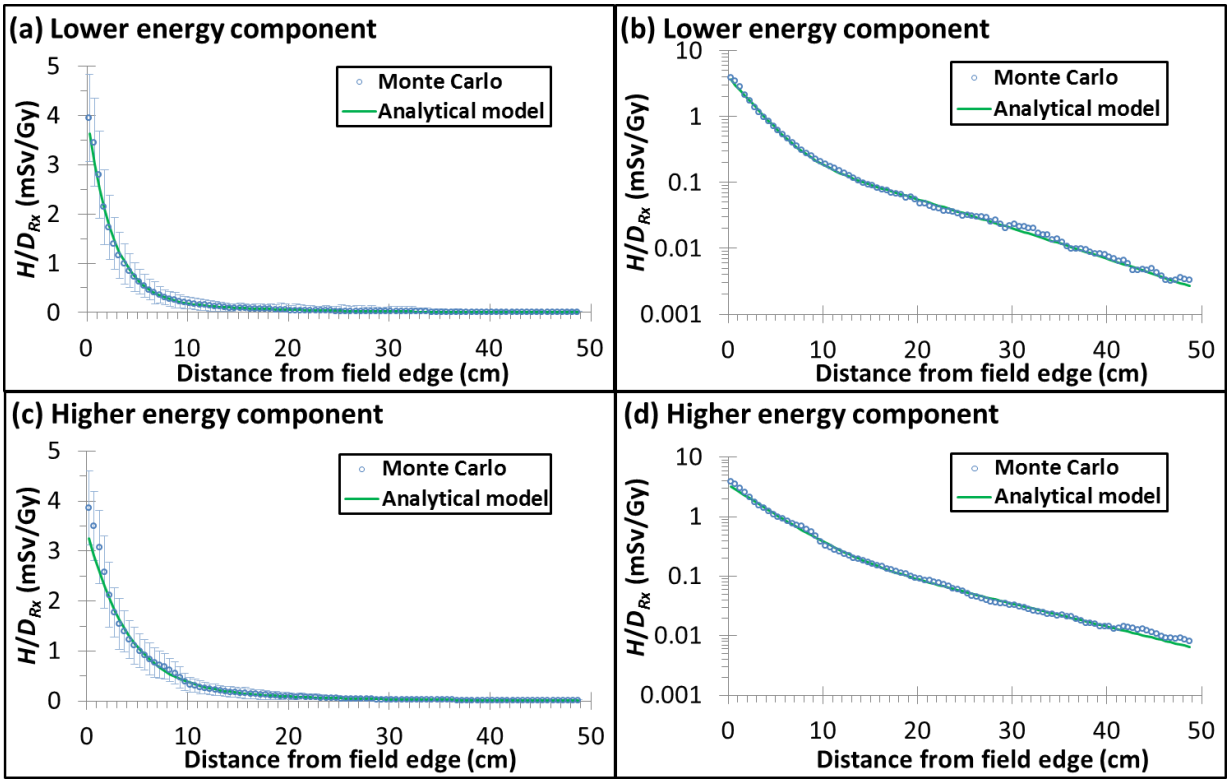

Figure 9. For intracranial fields of the girl, H/D_{Rx} versus r for the analytical model (green line) and the training Monte Carlo data (blue circles). These plots are for internal neutrons only and are separated into the lower energy (a and b) and higher energy (c and d) components. Monte Carlo data were from Taddei *et al* (95) and were averaged in 5-mm bins for viewing, with error bars as one standard deviation of the mean of each bin.

2.4.3 Preliminary validation of the analytical model

For the validation data of the boy, the analytical model estimation is plotted in Figure 10 against the Monte Carlo data for internal neutrons. From 3 cm to 10 cm from the field edge, the model estimated the Monte Carlo H/D_{Rx} very well, with average differences of -6.9% and 13.4% for the 160 MeV and 140 MeV beams, respectively. This was the most important region because of the much higher H/D_{Rx} values compared to those beyond 10 cm. More specifically, for 3 cm < r < 10 cm, the binned H/D_{Rx} data spanned from 0.13 mSv/Gy to 1.28 mSv/Gy, and, for $r \geq 10$ cm, the binned H/D_{Rx} data were less than 0.15 mSv/Gy. For 10 cm ≤ r ≤ 20 cm, the model overestimated the Monte Carlo result by approximately a factor of 2. For r > 20 cm and to the bounds of the model training, where H/D_{Rx} was less than 0.03 mSv/Gy, the model overestimated the Monte Carlo result by roughly 130%. For r > 49 cm, data was not shown because it was beyond the distance of the model training and the model systematically overestimated the Monte Carlo

result. In that region, the Monte Carlo data was less than 0.001 mSv/Gy.

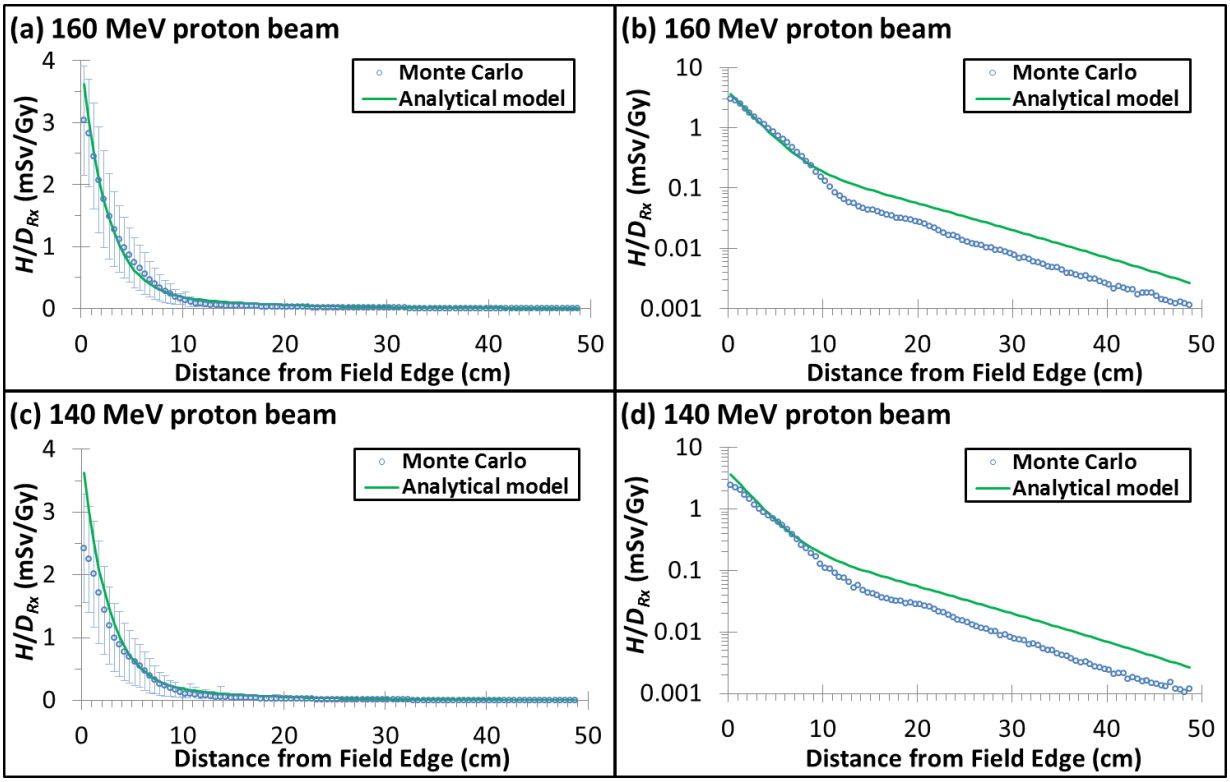

Figure 10. For intracranial fields of the boy, H/D_{Rx} versus *r* for the analytical model (green line) and the validating Monte Carlo data (blue circles). These plots are for internal neutrons only and show the 160 MeV (a and b) 140 MeV (c and d) nominal energy beams. Monte Carlo data were from Taddei *et al* (96) and were averaged in 5-mm bins for viewing, with error bars as one standard deviation of the mean of each bin.

We compared H_T/D_{Rx} of the boy's fields between the analytical model and Monte Carlo data (Figure 11). These data were summed with equal weighting between his fields of nominal energies of 140 MeV and 160 MeV, both in in the range of the lower energy component of the model. The model overestimated H_T/D_{Rx} simulations for all organs and tissues. Thus, the model provided a conservative estimate of equivalent dose from secondary neutrons produced in the patient's body. The model results were within a factor of two of the Monte Carlo result for organs whose voxels had an average distance of less than 20 cm from the field edge. For organs farther from the field edge, where H_T/D_{Rx} was less than 0.025 mSv/Gy, the model increasingly overestimated the internal neutron equivalent dose by more than a factor of 2.

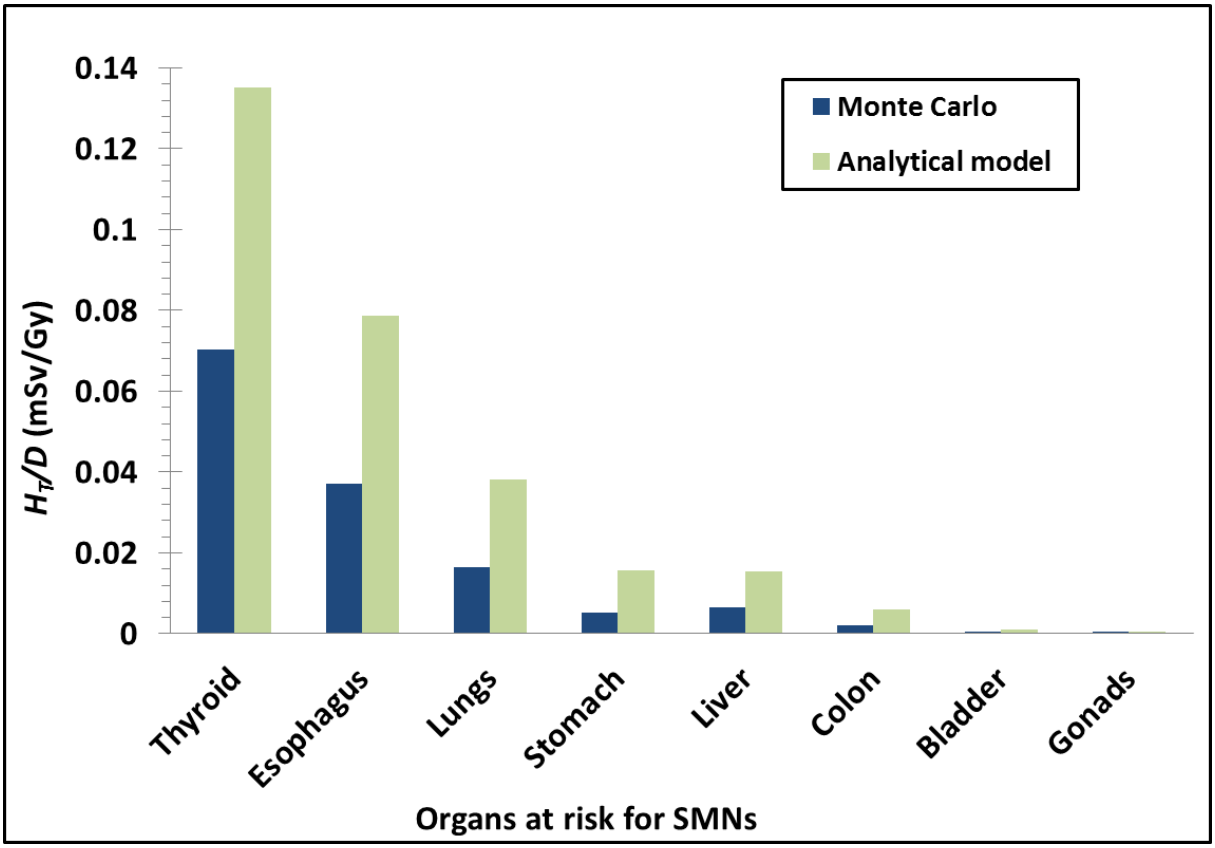

Figure 11. H_T/D_{Rx} determined by the analytical model (blue) and the Monte Carlo (light green). The Monte Carlo data were from Taddei *et al* (96).

2.5 Discussion

In this study, we developed a computationally-efficient analytical model to estimate the equivalent dose from internal neutrons produced in proton therapy of intracranial tumors. We tested our model for the fields of a boy who received intracranial proton therapy. We found the model was most accurate from 3 cm to 10 cm from the field edge, adequate from 10 cm to 20 cm (within a factor of 2), and less accurate beyond 20 cm (systematic overestimation). However, beyond 20 cm, the internal neutron equivalent dose was very small, below the quantity for which the carcinogenic dose-response relationship has known statistical significance (27). Thus, our model provided an adequate but slightly conservative estimation of equivalent dose throughout the boy's body. The recommended application of our internal neutron H_T/D_{Rx} model is for 3 cm < r ≤ 49 cm in pediatric intracranial proton therapy, where internal neutrons were shown to account for more than 20% of the equivalent dose.

As a figure of merit, we compared H_T/D_{Rx} for organs and tissues at risk for SMNs estimated by our model versus those calculated in previously-published Monte Carlo simulations. H_T/D_{Rx} calculated by the model and the Monte Carlo simulations differed by less than a factor of two for organs and tissues close in close proximity to the fields and more than a factor of two for those far from the field edge, e.g., the stomach and colon. However, in these far out-of-field organs the absolute equivalent doses from internal neutrons were small. The modeled H_T/D_{Rx} values of the analytical model were greater than those of the Monte Carlo in all organs and tissues. It is notable that one of the boy's beams was of lower nominal energy than the girl's beams that were used to train the model, and internal neutron equivalent dose increases with proton beam energy. Data were lacking in the literature for additional comparison for the higher energy component of the model. To address this, we also compared our H_T/D_{Rx} in the thyroid versus those of a roughly similar E = 168.2 MeV field of an 8-year-old girl in a study by Zacharatou Jarlskog *et al* (44). The result of our analytical model, at 0.70 mSv/Gy, was higher than theirs, at 0.31 mSv/Gy. This difference may have been attributable to their differing definition of radiation weighting factor.

The strength of the analytical model is its fast application to account for stray neutron radiation in proton therapy, in which internal neutrons contribute to the potential risk of late effects, for example radiation-induced necrosis and cancer. The newest proton therapy facilities have adopted pencil-beam scanning and older facilities are being retrofitted for this delivery technique. As pencil-beam scanning largely mitigates external neutron production, internal neutron doses will emerge as the stray radiation of primary concern for patients receiving proton therapy. In our analysis, in the absence of external neutrons, internal neutrons accounted for 20% and 56% of the equivalent dose at 3 cm and 15 cm from the field edge, respectively.

Our model does not account for external neutrons, which vary greatly by beam characteristics, facility design, and treatment delivery apparatus. To account for neutrons produced outside the patient, for example in treatment units for which the fields are partially or fully shaped by scattering or modulating components during delivery, a separate model should be applied. One model that had been developed extensively to estimate patients' external

neutron exposure was that of Schneider *et al* (57). These analytical models, combined with the proton dose calculated by the clinical TPS and extended anatomical imaging and organ delineation (Gallagher *et al* manuscript 1 in preparation), have the potential for fast generation of a whole-body dosimetric map with limited computational overhead. Fast full body dosimetry may enable the estimation of long-term side effects for clinical decisions or the relating of dose and effects for epidemiological studies, most importantly for pediatric patients.

The chief limitation of this study was that the model is only applicable for similar pediatric intracranial tumors. For different treatment sites, the double-Gaussian model may be valid but would require re-parameterization. Future studies are underway to expand the model to become more broadly encompassing to include other treatment sites and various energies of beams and sizes of irradiated volumes. The latter would account for spread out Bragg peaks and aperture sizes. A second important limitation of the study was that only one patient's Monte Carlo simulations were available for validation. This was due to a shortfall of available data for comparison. Another limitation was that, the validation fields were in the range of the lower energy component only and not the higher energy component, which we were not able to validate against existing published data. For these reasons, we classified our validation as 'preliminary.' A factor of two uncertainty would be unacceptable for therapeutic doses. However, for out-of-field neutron doses, for which other large uncertainties exist—e.g., relative biological effectiveness, radiation weighting factor, dose and dose rate effectiveness factor, and measurement uncertainties—a factor of two inaccuracy is acceptable (93). On this basis, the application of this simple analytical model to evaluate out-of-field dose from internal neutrons is a sizable step forward from the current clinical practice of disregarding these doses.

In conclusion, we trained our analytical model for a child receiving intracranial proton therapy and found that it adequately, and somewhat conservatively, estimated out-of-field internal neutron dose in a second child. The model was most accurate within 10 cm of the treatment fields, where the internal neutron dose contributes the most to overall exposures. It may be applied for similar proton therapy fields to estimate internal neutron equivalent dose, regardless of treatment unit design or clinical environment. Notably, our findings also demonstrated the feasibility of using analytical models rather than complicated and

computationally-expensive Monte Carlo simulations to generate estimates of neutron doses in patients receiving proton therapy.

2.6 Acknowledgements

We are grateful for the scientific counsel of John Eley, Jatinder Saini, Robert Stewart, and Wayne Newhauser. Funding was in part by the Fogarty International Center (award K01TW008409), the Naef K. Basile Cancer Institute, and the Portland Chapter of the Achievement Rewards for College Scientists. The content is solely the responsibility of the authors and does not necessarily represent the official views of the sponsors.

3.0 Manuscript 3 – Independent validation of an analytical model for equivalent dose produced in a passive-scattering proton therapy treatment unit

Kyle J Gallagher, B.A.[1,2] and Phillip J Taddei, Ph.D.[3,4]

(1) Oregon State University, Corvallis, Oregon, (2) Oregon Health and Science University, Portland, Oregon, (3) American University of Beirut Medical Center, Beirut, Lebanon, (4) University of Washington School of Medicine, Seattle, Washington

3.1 Abstract

Purpose: To independently validate an analytical model for equivalent dose from neutrons produced in a passive-scattering proton therapy treatment unit (i.e., "external neutrons"), H.

Methods: To accomplish this objective, we applied the previously-published model to treatment plans of two pediatric patients. Their model accounted for external neutrons generated from a pristine Bragg peak and closed-aperture. To apply this model to a clinical setting, we adjusted the model to account for the area of the collimating aperture, range modulation, air gap, and radiation weighting factor. We applied the slightly adjusted model to estimate H per prescribed proton absorbed dose, D_{Rx}, for the passive-scattering proton therapy beams of two children, a 9-year-old girl and 10-year-old boy, who each received intracranial boost fields as part of their treatment. In organs and tissues at risk for radiation-induced subsequent malignant neoplasms (SMNs), T, we calculated the mass-averaged H, H_T, per D_{Rx}. Finally, we compared H_T/D_{Rx} values to those of Monte Carlo simulations of these patients' fields from the literature.

Results: H_T/D_{Rx} values of the adjusted external neutron model deviated from the Monte Carlo result on average for all the organs by 20.8 ± 10.0% and 44.2 ± 17.6% for the girl and boy, respectively. The adjusted model underestimated the Monte Carlo result in all T of each patient, with the exception of the girl's bladder, for which the adjusted model overestimated H_T/D_{Rx} by 3.1%. The adjusted model provided a better estimate of H_T/D_{Rx} than the unadjusted model, for

which the deviation from the Monte Carlo result was reduced by approximately 37.0% and 46.7% for the girl and boy, respectively.

Conclusion: In our validation, we found that that the previously-published analytical model, combined with adjustment factors to enhance its clinical applicability predicted H_T/D_{Rx} in out-of-field organs and tissues at risk for SMNs with acceptable accuracy. This finding suggests that the analytical model may be used by clinicians and researchers to routinely calculate equivalent dose from external neutrons in passive-scattering proton therapy.

3.2 Introduction

Nontherapeutic stray neutrons are produced in the delivery of proton therapy beams. These neutrons are of concern because of their high and uncertain relative biological effectiveness (RBE) for late effects such as carcinogenesis (101–104). Neutrons produced in the patient are unavoidable, but neutrons generated in the treatment unit, i.e., "external neutrons," may be attenuated before reaching the patient (18,105). In passive-scattering proton therapy (PSPT), the final collimating aperture is the chief source of patient exposures to neutrons generated in the treatment unit (i.e., "external neutrons") (21,22). Because commercial treatment planning systems (TPSs) in proton therapy do not calculate the equivalent dose from external neutrons, *H*, a vast number of research studies into *H* have applied detailed Monte Carlo simulations (16,17,22,44,74,94–96,106). However, these Monte Carlo simulations are time consuming and, therefore, not currently used in a clinical setting. Analytical models, on the other hand, may offer faster computations of *H* with acceptable accuracy.

Schneider *et al* (57) enhanced an analytical model to calculate *H* based on the previous work of Zhang *et al* (99) and Pérez-Andújar *et al* (98). The result of their model was a fast and accurate calculation of *H* (in mSv) per prescribed proton absorbed dose, D_{Rx}, (in Gy) in water. However, the authors noted that their analytical model was limited in its translation to clinical practice, specifically, in that it lacked range modulation, i.e., it was for single proton energies that generate pristine Bragg peaks. Furthermore, it assumed a closed-aperture of 8 cm thickness, a 15 cm air gap, and a radiation weighting factor (w_R) that was less conservative than previous studies (95,96). In a subsequent study, Eley *et al* (97) adjusted the model to account for clinical proton beam characteristics—specifically, range modulation to create a spread-out

Bragg peak (SOBP), the area of the aperture to account for field size, and heterogeneity in tissues. After integrating their model into a TPS, they estimated *H* in the thyroid of a woman treated for Hodgkin Lymphoma with PSPT beams within 40% of the Monte Carlo result. The results of their study demonstrated the feasibility of an accurate calculation of *H* with significantly reduced computation time versus that of Monte Carlo. All of these studies were performed within the same research group, and to date, a validation by independent researchers had not been performed.

The purpose of this study was to independently validate the model developed by Schneider *et al* by using it to quantify out-of-field *H* in PSPT of children with intracranial tumors. Similarly to Eley *et al*, we adjusted the model for the clinical setting. However, in a different approach, we used factors from previous Monte Carlo studies to account for the aperture area, SOBP, air gap, and w_R. Then we applied the adjusted model to the intracranial PSPT fields of a 9-year-old girl and a 10-year-old boy. As a figure of merit, we compared average H/D_{Rx} in organs and tissues at risk for subsequent malignant neoplasms (SMNs), *T*, H_T/D_{Rx}, to the values calculated by previously-published Monte Carlo simulations (95,96).

3.3 Methods

3.3.1 Patient selection

Because Monte Carlo simulations had already been performed, treatment fields of the 10-year-old boy of Taddei *et al* (96) and the 9-year-old girl of Taddei *et al* (95) were selected for this study. In each study, Monte Carlo calculations were performed using the Monte Carlo N-Particle eXtended code version 2.6b (107) to estimate the absorbed dose from external neutrons in each voxel, D_v, of the patients' simulated bodies. Each study applied the recommendations of the International Commission on Radiological Protection (ICRP) in Publication 92 (108) to estimate the radiation weighting factor, w_R. With these parameters, they determined *H* in each voxel, *v*, using the following equation:

$$H_v = w_R \cdot D_v. \quad (1)$$

Each patients' plan included intracranial boost fields. These fields were similar in design to those of treatments for localized brain tumors, such as astrocytomas, ependymomas, and

gliomas. Determining and minimizing out-of-field *H* for pediatric patients with brain tumors such as these is critical because they may have good long-term prognoses and are therefore at risk of developing late-effects of which SMNs are the chief concern (3).

3.3.2 Patient diagnosis, prescription, and treatment planning

In the previous study, treatment plans for a girl and a boy diagnosed with primitive neuroectodermal tumors were considered. Their treatments included intracranial boosts of 23.4 Gy-RBE, or 21.3 Gy (100) prescribed to the clinical target volumes (CTVs) using PSPT. For the girl, the intracranial boosts comprised three fields of energies either 160 MeV or 180 MeV. The boy's two intracranial boost fields were similarly designed to deliver 23.4 Gy-RBE to the CTV using PSPT but of slightly lower energies, at 140 MeV and 160 MeV. The beam characteristics of the intracranial boost fields for these two children are summarized in Table 10. Further details of the computed tomography simulations, treatment plans, and Monte Carlo techniques used for dose calculation can be found in the previous publications.

Table 10. Summary of the treatment parameters for the intracranial proton boost fields of the girl and boy in this and the previous studies (95,96). Abbreviations of beam orientations include left posterior oblique (LPO), posterior-anterior (PA), right posterior oblique (RPO), and left lateral (LL).

	Girl			Boy	
Beam	1	2	3	1	2
Beam orientation	LPO	PA	RPO	LPO	LL
Gantry angle (degree)	97	180	263	130	90
Nominal beam energy (MeV)	160	180	160	160	140
Maximum range in patient (cm H_2O)	12.0	13.5	12.0	11.3	9.2
SOBP width (cm)	8.0	8.0	8.0	7.0	6.0
Collimated field, major axis (cm)	6.6	7.0	6.3	11.8	11.6
Collimated field, minor axis (cm)	6.3	6.3	6.3	5.5	5.4
Air gap (cm)	23.0	29.0	23.0	2.0	2.0
Aperture thickness (cm)	4	6	4	4	4

3.3.3 Translation of the analytical model to a clinical setting

The analytical model previously developed by Schneider *et al* to estimate *H* characterized four different external neutron energy regimes, contained 22 fitting parameters, and was continuous with proton beam energy from 100 to 250 MeV. We adjusted the model for translation to a

clinical setting. Specifically, the adjustments accounted for the w_R, SOBP, aperture size, and air gap. Each of these factors were based on previous publications of this research laboratory (109,110), which were all performed using the same PSPT clinic as a model. The equation for the adjusted model was written as,

$$H_v/D_{Rx} = F_{wR} \cdot F_{SOBP} \cdot F_{as} \cdot F_g \cdot H_{S,v}/D_{Rx}, \quad (2)$$

where F_{wR}, F_{SOBP}, F_{as}, and F_g were the adjustment factors for w_R, SOBP, aperture size, and air gap, respectively. $H_{S,v}/D_{Rx}$ was H_v/D_{Rx} calculated by the external neutron analytical model developed by Schneider *et al*.

Because the w_R used to determine H by Schneider *et al* was significantly lower than the w_R used in the previous Monte Carlo datasets of the boy and girl, we adjusted the w_R values to make a better comparison between the results of the analytical model and those of the Monte Carlo simulations. We calculated F_{wR} as the ratio of the Monte Carlo studies' w_R values to the values applied by Schneider *et al*. The w_R values were not given by Schneider *et al*, so we approximated their values by using equation 5 from their previous study (98). This equation 5 calculated w_R as a function of depth and off-axis distance. The Monte Carlo studies' determined w_R at isocenter for various proton beam energies based on ICRP Publication 92 (108) (Figure 5a of Zheng *et al* (110)). The w_R for the respective proton beam energies of the intracranial boost fields were used to calculate F_{wR} for which F_{wR} varied for each voxel.

An SOBP adjustment factor was created to account for the lack of modulation in the analytical model. F_{SOBP} was taken directly from Zheng *et al* (110). In these studies, Zheng *et al* performed Monte Carlo simulations comparing the ambient equivalent dose per proton therapeutic dose at isocenter, $H^*(10)/D_{iso}$, from a 250 MeV proton beam for various SOBP widths normalized to a pristine Bragg peak in Figure 9a of Zheng *et al* (110). The factor reflecting the relative increase in $H^*(10)/D_{iso}$ of the medium field size for the respective SOBP width was directly used for F_{SOBP} (Table 1) and applied to each intracranial boost field.

We adjusted the model for the varying size of the aperture in the clinical treatment fields in our study. We derived F_{as} based on the results of the previous Monte Carlo studies.

Similar to SOBP, Zheng *et al* performed Monte Carlo simulations comparing $H^*(10)/D_{iso}$ for various aperture sizes and a closed-aperture in Figure 8 of Zheng *et al* (110). However, this Figure 8 was not normalized to a closed-aperture; therefore, F_{as} was determined as $H^*(10)/D_{iso}$ of the medium field size for the respective aperture area of each intracranial boost field divided by $H^*(10)/D_{iso}$ of the medium field size for the closed-aperture (Table 1).

To account for air gap, F_g was derived from the previous Monte Carlo studies. Zheng *et al* (109) conducted Monte Carlo simulations to study the effect of distance from the treatment snout on H per the therapeutic absorbed proton dose, D_p, for medium and large fields of a 250 MeV proton beam (Figure 7 of Zheng *et al* (109)). In our study, the air gap, g, was calculated as the snout position (i.e., distance from snout to isocenter) minus the upstream radius of the tally volume in their study. F_g was calculated as the ratio of H/D_p of the snout position that equated to the air gap of the intracranial fields and H/D_p of the snout position that equated to the air gap used by Schneider *et al* to train the model, i.e, 15 cm. Thus, air gaps larger than 15 cm, e.g., those of the girl's fields, would result in F_g values less than 1, and air gaps smaller than 15 cm, e.g., those of the boy's fields, would result in F_g values greater than 1. The air gap of the boy's fields was only 2 cm, which is very rare in clinical applications but was maintained in our study so that we could compare our results with those of the previous publications. A 2-cm air gap was less than the smallest air gap studied by Zheng *et al* and required extrapolation beyond the scope of their data, i.e., snout position that equated to a 14 cm air gap. This was done by fitting the data points to a logarithmic function to the following equation:

$$\mathrm{H_Z}\big/\mathrm{D_p} = -11.81 \ln \mathrm{g} + 50.767, \tag{3}$$

for which H_Z/D_p was H/D_p calculated in Figure 7 of Zheng *et al* (109) and g was the air gap (cm) calculated from the snout position. To verify the fitted function, previous Monte Carlo simulations estimating the neutron equivalent dose of the left posterior oblique (LPO) field of the girl were compared to the similar LPO field of the boy. The main difference between the two fields was the air gap, where the air gap was 23 cm for the girl and 2 cm for boy. The neutron equivalent dose decreased by a factor of 2.7 to 3 when increasing the air gap from 2 cm to 23 cm, which was consistent with the prediction of the fitted function. Therefore, the fitted

function was used to determine the F_g for the boy. As a result, field-specific w_R, SOBP, aperture size, and air gap of the clinical fields were all considered in our adjustments to the analytical model developed by Schneider *et al*.

We implemented the adjusted model into in-house codes and commercial software (version R2014a, MATLAB, The MathWorks, Inc., Natick, Massachusetts) to calculate H_v/D_{Rx}. These H_v/D_{Rx} values were used along with the contours for *T* from the previous publications for the girl and boy to compute mass-averaged H_T/D_{Rx} for out-of-field *T* at risk for SMNs for each patient. These organs and tissues comprised the esophagus, thyroid, heart, lungs, liver, small bowel, colon, stomach, kidneys, bladder, breast tissue, ovaries, testicles, and prostate. H_T/D_{Rx} was determined for each individual adjustment of the model and for all adjustments. These values were compared to the respective previous Monte Carlo results of the girl and boy.

3.4 Results

3.4.1 Validation of the previous analytical model

The adjustment factors used to account for SOBP, aperture area, air gap, and w_R of each intracranial beam are summarized in Table 11. Unlike the other adjustment factors, w_R varied for each voxel and therefore, the average F_{wR} was reported. The largest adjustment factors for the girl were F_{SOBP} and F_{wR}. The adjustment factors for the boy were similar to that of the girl except for F_{as}. F_{as} was the largest adjustment factor for the boy which increased H_v/D_{Rx} by 122%. Conversely, F_{as} for the girl decreased H_v/D_{Rx} by 36.3%. The w_R for each field of the Monte Carlo dataset was also included in Table 11 and were within 3% on average of those determined from Zheng *et al* (110). The w_R used by Schneider *et al* (57) was consistently a factor of approximately 1.7 lower than those of the Monte Carlo dataset of the girl and boy.

Table 11. Adjustment factors used to translate the model developed by Schneider *et al* (57) for use with clinical beams. Because F_{wR} varied for each voxel, the average is reported. Additionally, w_R of the Monte Carlo datasets of the girl and boy are reported (95,96).

	Girl			Boy	
Beam	1	2	3	1	2
F_{as}	0.930	0.930	0.930	0.900	0.890
F_{SOBP}	1.800	1.800	1.800	1.750	1.690
F_g	0.680	0.550	0.680	2.220	2.220
F_{wR}	1.710	1.750	1.710	1.730	1.700
w_R of the datasets of the girl and boy	9.410	9.410	9.430	9.540	9.730

The resulting H_T/D_{Rx} were compared to the previous Monte Carlo simulations in Figure 12 for the girl. Before we applied any adjustment factors to the model, H_T/D_{Rx} calculated by the model was less than the Monte Carlo results for all organs. More specifically, H_T/D_{Rx} calculated for all organs by the model was 57.4 ± 4.8% on average lower than the Monte Carlo results. After applying all corrections, H_T/D_{Rx} calculated by the model was less than the Monte Carlo results for all organs with the exception of the bladder for which the model overestimated H_T/D_{Rx} by 3.0% compared to the Monte Carlo results. Otherwise, H_T/D_{Rx} calculated for all organs by the model was 20.8 ± 10.0% on average lower than the Monte Carlo results. The maximum deviation of the model from the Monte Carlo result was in the breast tissue, for which H_T/D_{Rx} calculated by the model underestimated the Monte Carlo result by 39.0%.

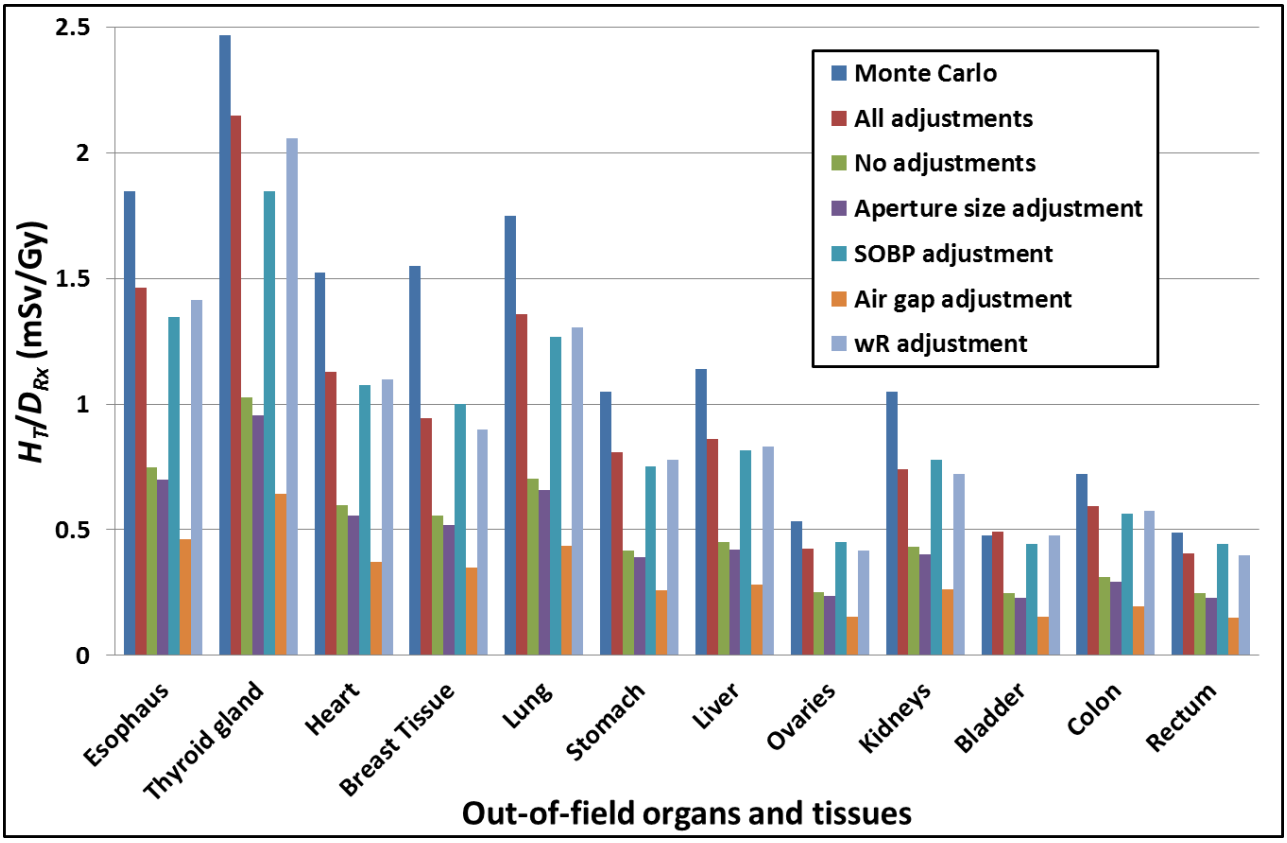

Figure 12. Bar graph of H_T/D_{Rx} from external neutrons for the composite of the intracranial boost fields used to treat the girl. The mean organ doses are estimated by Monte Carlo simulations (blue), the model with all adjustments (red), the model with no adjustments (green), the model with the field size adjustment (purple), the model with the SOBP adjustment (teal), the model with the air gap adjustment (orange), and the model with the radiation weighting factor (w_R) adjustment (gray).

Similar to the girl, the resulting H_T/D_{Rx} were compared to the previous Monte Carlo simulations for the boy in Figure 13. Before we applied any adjustment factors to the model, H_T/D_{Rx} estimated by the model was less than the Monte Carlo results for all organs. H_T/D_{Rx} calculated by the model underestimated the Monte Carlo results by 91.4 ± 2.9% on average for all the organs. After applying all corrections, H_T/D_{Rx} calculated by the model still underestimated the Monte Carlo results for all organs for which the model underestimated H_T/D_{Rx} by 44.2 ± 17.6% on average for all the organs. The girl was also differed from the boy, in that H_T/D_{Rx} estimated in organs near the treatment field was generally closer to the Monte Carlo result than organs further from the treatment field. For example, H_T/D_{Rx} estimated by the model for the esophagus, thyroid, heart, lungs, stomach, liver, and kidneys were 31.7 ± 10.8% on average lower than the Monte Carlo result. In comparison, H_T/D_{Rx} estimated by the model for the

prostate, bladder, colon, rectum, and testicles were 61.7 ± 5.1% on average lower than the Monte Carlo result. The model's maximum deviation from the Monte Carlo result was in the rectum, for which H_T/D_{Rx} estimated by the model underestimated the Monte Carlo result by 65.9%.

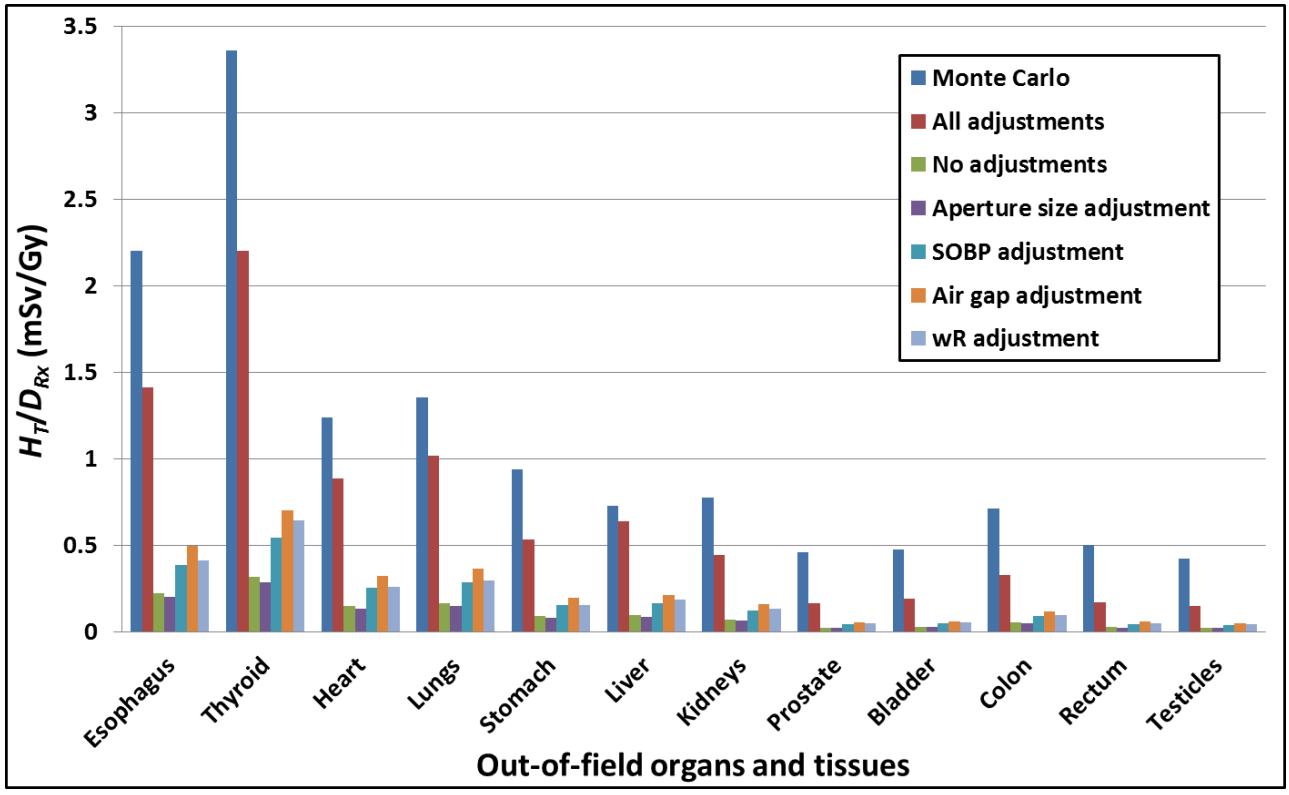

Figure 13. Bar graph of H_T/D_{Rx} from external neutrons for the composite of the intracranial boost fields used to treat the boy. The mean organ doses are estimated by Monte Carlo simulations (blue), the model with all adjustments (red), the model with no adjustments (green), the model with the field size adjustment (purple), the model with the SOBP adjustment (teal), the model with the air gap adjustment (orange), and the model with the radiation weighting factor (w_R) adjustment (gray).

3.5 Discussion

In this study, we confirmed the accuracy of a model developed by Schneider *et al* to estimate out-of-field *H* for two pediatric patients with intracranial tumors. This validation was performed by researchers that were independent from the authors that developed the model. To improve its accuracy, we slightly adjusted the model to account for SOBP, aperture area, air gap, and w_R. After these adjustments, the model generally predicted H_T/D_{Rx} within a factor of two.

Our aim was to demonstrate the feasibility of using a fast and reasonably simple

analytical model to estimate external neutron equivalent dose with an acceptable level of accuracy but without the computational overhead and complexity of Monte Carlo. Similar accuracy was achieved when validating Monte Carlo results (the gold standard for dose calculations) against measurements (109,111,112). Moreover, given the high uncertainty in the RBE of neutrons for carcinogenesis (101–104), this adjusted model provided adequate accuracy. The adjusted analytical model gives clinicians the opportunity to routinely calculate equivalent dose from external neutrons and make clinical decisions to choose proton treatment plans that limit the stray neutron equivalent dose and effectively lower the risk of SMNs for these pediatric intracranial cases.

Adjusting the model for clinical fields proved to be more important for the boy's plan than for the girl's. Before applying the adjustment factors to the model, H_T/D_{Rx} estimated by the model was a factor of 13 on average less than the Monte Carlo result. After adjusting the model, H_T/D_{Rx} estimated by the model was generally within a factor of two of the Monte Carlo result. The main reason for this difference was the very small 2-cm air gap applied in the treatment boy of the boy, which, in proton therapy is much smaller than the 15 cm air gap used to train the model developed by Schneider *et al* and the 23 to 29 cm air gap to treat the girl. The considerable deviation in the length of the air gap at treatment compared to the training data, created a large adjustment factor of 2.22 for the boy's fields while the adjustment factor for the girl's fields were closer to 1 (average $F_g = 0.64 \pm 0.08$) and lowered the overall adjustment to the model. The limitation of the extrapolation beyond Zheng *et al*'s work was not belabored because we propose to apply this model to PSPT of pediatric patients with less extreme air gaps, such as the girl.

The results of our implementation of the model developed by Schneider *et al* may be compared to those of Eley *et al* (see section 1). The implementation of the model by Eley *et al* overestimated the Monte Carlo result in the thyroid of the Hodgkin Lymphoma patient by 39% whereas in our study the adjusted model underestimated the Monte Carlo result by 13% and 34% in the thyroid for the girl and boy, respectively. Nonetheless, the magnitude of the percent difference in Eley *et al* was similar to those found in this study for both the boy and the girl. Differences in the model predictions between the two studies may be attributed to the different

methods of translation to the clinical setting. Eley *et al* accounted for SOBP, aperture area, and heterogeneities whereas we accounted for SOBP, aperture area, air gap, and w_R.

The methods we used to adjust the model had several limitations. Although we addressed four limitations of the Schneider *et al* model to approach clinical realism, not all limitations were accounted for in our adjustments. Unlike Eley *et al*, we did not account for heterogeneities within the patient. Instead, we considered the patient to be water. Accounting for heterogeneities would be a major improvement for the model because neutrons interact by nuclear interactions which are dependent on the composition of the material. Another possible improvement to the model that we did not address would be to compensate for other complexities the model lacked, such as assuming a single point source of neutrons on the distal edge of the final collimating aperture rather than the real scenario in which neutrons are generated throughout the aperture blocks. Furthermore, Zheng *et al* (109) demonstrated a 17.5% decrease in the external neutron equivalent dose when using a collimator thickness of 8 cm versus 10 cm for 250 MeV protons. We did not take into account, for example, the self-shielding of neutrons, which could be approximated by integrating over point source positions within the aperture block, which vary in thickness and size, as well as the beam shape incident on the aperture. The latter conditions may be an avenue to applying the model to magnetic scanning delivery systems that use an aperture to improve the penumbra of the beam. This omission may have contributed to the general underestimation of H_T/D_{Rx} values from our adjusted model compared to those of Monte Carlo simulations. Finally, a limitation of our adjustments to the model was that we applied multiplicative factors based on data from studies of 250 MeV nominal energy proton beams rather than a variety of energies. Future developments of a more generalized analytical model may test and, if necessary, account for the effect of these various physical aspects of a modern clinical proton beam.

In conclusion, we validated independently a fast and simple analytical model developed by Schneider *et al* by applying clinically-relevant adjustment factors to estimate the equivalent dose from neutrons generated in a PSPT treatment unit. The model provided satisfactory estimates of equivalent dose from external neutrons in out-of-field organs and tissues for two realistic pediatric intracranial therapy cases. This independent validation suggests that clinicians

and researchers may use this model to understand and minimize neutron exposures and SMN risks in children treated for intracranial tumors with PSPT at the proton treatment facility used in this study.

3.6 Acknowledgements

Funding details will be added after completion of the peer review process.

4.0 Manuscript 4 - *In silico* retrospective clinical trial comparing predicted subsequent malignant neoplasms in photon versus proton therapy of a pediatric cohort with intracranial tumors

Kyle J Gallagher[1,2], Bassem Youssef[3], Rola Georges[4], Anita Mahajan[4], Joelle Ann Feghali[3], and Phillip J Taddei[3,4,5]

(1) Oregon State University, Corvallis, Oregon, (2) Oregon Health and Science University, Portland, Oregon, (3) American University of Beirut Medical Center, Beirut, Lebanon, (4) The University of Texas MD Anderson Cancer Center, Houston, Texas, (5) University of Washington School of Medicine, Seattle, Washington

4.1 Abstract

Hypothesis: It was our hypothesis that pediatric patients treated with intracranial photon fields in a low- to middle-income country (LMIC) would not have a statistically significant elevated risk of developing a fatal subsequent malignant neoplasm (SMN) versus if they were treated with proton therapy in a high-income country (HIC).

Methods: We conducted an *in silico* clinical trial to test our hypothesis. The sample set of seven pediatric patients were collected from the clinical database of the American University of Beirut Medical Center. Retrospective sampling criteria were the following: all patients with available CT images and treatment plans, of ages between 2 to 14 years at diagnosis, diagnosed with low-grade brain tumors (e.g., ependymoma), and who were treated with three-dimensional conformal radiation therapy between January 1, 2009 to September 30, 2011in a LMIC academic institution. These patients' CT images and organ and target contours were de-identified and sent to a HIC academic hospital for proton therapy treatment planning. Treatment planning systems (TPSs) of the hospitals were used to calculate absorbed dose from the therapeutic fields. Analytical models from the literature were applied to calculate stray radiation doses. Equivalent dose from both therapeutic and stray radiation was determined as the product of the absorbed dose and radiation weighting factor for each type and energy of radiation. To determine dose outside the extents of the patients' original CT images, supplemental

computational phantoms were fused to each patient. The lifetime attributable risk of mortality, *LAR*, from SMNs was determined for each known radiogenic cancer site, *T*, using a dose-effect model from the literature. As a figure of merit, we calculated the ratio ($\underline{LAR_{proton}}/LAR_{photon}$) of the total LAR_T for any cancer site, LAR_{total}, to compare the two modalities.

Results: The average ratio of LAR_{total} was 0.75 ± 0.22 (one standard deviation of the mean) for the set of patients which lead to the rejection of the null hypothesis (H_0: average ratio of LAR_{total} =1) with a p-value of 0.011.

Conclusions: For this set of seven pediatric patients, proton therapy in a HIC would have reduced the risk of developing a fatal SMN compared to the photon therapy that they received in a LMIC. Our findings suggest that proton therapy would reduce the risk of a fatal SMN in pediatric patients with intracranial tumors if it were made available in LMICs.

4.2 Introduction

High survival rates of children with cancer have increased the need for research of late-effects. The survival rate of children with cancer Among children of age 14 years old or younger who received cancer treatment between 2003 and 2009 in the United States, Siegel and Jemal (2) reported a 5 year survival rate of 84% and 82% for girls and boys, respectively. Despite these high survival rates, many of these children will develop adverse late-affects due to their radiation therapy (23) which is often incorporated into the course of treatment. Unfortunately, radiation therapy has also contributed to the adverse late-effects experienced by survivors of childhood cancer. The most concerning late effect is a subsequent malignant neoplasm (SMN). SMNs have been shown to be the leading cause of death twenty years after childhood radiation treatments (1).

One promising avenue to reduce the risk of SMNs is proton radiotherapy. In order to triage resources, assessing whether proton therapy would be of benefit is of particular importance for patients who would require travel to a proton center such as those in a low- to middle-income country (LMIC), where proton therapy is not available. Taddei *et al* (manuscript in preparation) conducted a virtual clinical trial of a cohort of children receiving craniospinal irradiation from proton therapy in the United States and photon therapy in Lebanon. They

found that proton therapy reduced the risk of fatal SMNs by 41%. However, no comparison between proton and photon therapies has been performed for the projected risk of fatal SMNs in a cohort of children receiving intracranial external beam therapy.

We hypothesized that proton therapy in a high-income country (HIC) would provide no benefit to reducing the risk of a fatal SMN in children with intracranial tumors compared to photon therapy in a LMIC. We tested our hypothesis by performing an *in silico* clinical trial on a sample set of 7 pediatric patients with intracranial tumors. Equivalent dose in organs and tissues for each modality were calculated using the respective clinical treatment planning system (TPS) to estimate therapeutic radiation. Stray radiation was estimated using analytical models from the literature. The lifetime attributable risk of a fatal SMN was predicted for each patient and radiogenic cancer site using a dose-effect model from the literature.

4.3 Methods

4.3.1 Patient sampling and contouring

Seven pediatric patients of ages 3 to 12 years old who were treated for intracranial tumors at a LMIC institution, American University of Beirut Medical Center (AUBMC), were retrospectively selected under Institutional Review Board protocol. This cohort was treated with 6-megavoltage (MV) three-dimensional conformal radiation therapy (3DCRT) treatment plans. Due to the computed tomography (CT) simulation image sets of the patients missing large portions of the patients' bodies, each patient was matched and fused with a supplemental computation phantom of similar size. These phantoms were of anonymized patients who underwent craniospinal irradiation and for whom organs and tissues at risk for SMNs were contoured previously (Taddei *et al* manuscript in preparation).

The contours used in this study were from Gallagher *et al* (manuscript 1 in preparation) with three exceptions. To avoid overestimation in the risk projection, the red bone marrow, remainder, and skin contours were subtracted by the treated volume, i.e., the 95% isodose volume (113), for both photon and proton therapies. The treated volume was used instead of the target volume because proton and photon therapies had different size target volumes due to differing standards of care in applying margins to the clinical target volume to account for

uncertainty in the treatment. To maintain consistency between the two modalities the treated volume was used instead of the target volume. The final structure set consisted of the thyroid, red bone marrow, remainder, skin, breast tissue, lungs, liver, stomach, uterus, ovaries, prostate, testicles, bladder, and colon which included the rectum. Further information concerning the contours, the implementation of the supplemental phantoms, and the selection criteria are given by Gallagher *et al* (manuscript 1 in preparation). For comparison with proton therapy, each patient's CT image sets and structure sets were anonymized, encrypted, and securely transferred to the HIC academic institution, University of Texas MD Anderson Cancer Center.

4.3.2 Treatment planning and dosimetry

The dosimetry for photon therapy used in this study was published previously (Gallagher *et al* manuscript 1 in preparation) and is briefly described in this paragraph. The photon 3DCRT treatment plans were collected from the LMIC institution. Some plans were adjusted to meet the standard of care at the LMIC institution and were approved by an attending radiation oncologist. A clinically-commissioned commercial treatment planning system (Panther version 5.01, Prowess Inc., Concord, California) was used to calculate the in-field therapeutic radiation. An analytical model from the literature was re-parameterized with new measurements to estimate the out-of-field stray radiation. Equivalent dose, H, was calculated by multiplying the absorbed dose, D, by a radiation weighting factor, w_R, of 1 (84) in each voxel. Mean equivalent dose, H_T, in each organ or tissue, T, at risk for SMNs was calculated in each patient and their fused supplemental phantom.

We conducted the dosimetry for proton therapy as part of this study. At the HIC institution, passive-scattering proton therapy (PSPT) treatment plans were constructed by a proton radiotherapy dosimetrist using a commercial treatment planning system (Eclipse version 8.9; Varian Medical Systems, Palo Alto, CA) and approved by an attending pediatric radiation oncologist. The treatment planning system was used to calculate D from therapeutic protons. To determine H from therapeutic protons, the mean quality factor of 1.1 was used as an estimate for w_R (48,114). To account for H from stray neutrons produced in the patient and in the treatment unit analytical models from the literature were applied (Gallagher and Taddei manuscript 2 in preparation, manuscript 3 in preparation). For internally-produced neutrons, a

previously-published function between equivalent dose and distance from the therapeutic field edge (i.e., 50% isodose line) (Gallagher and Taddei manuscript 2 in preparation) was applied to all voxels farther than 3 cm from the composite field edge. For externally-produced neutrons, an analytical model developed by Schneider *et al* (57) was implemented with adjustment factors for clinical realism from Gallagher and Taddei (manuscript 3 in preparation). The total equivalent dose was determined by summing *H* from therapeutic and stray radiation in each voxel. H_T was calculated as the mass-averaged mean of the total equivalent dose for each organ or tissue at risk for SMNs inside each patient and their fused supplemental phantom. For simplicity, because the boost fields for each modality were of small dose compared to the initial fields, boost fields were neglected in this study. The initial fields were renormalized to deliver a prescribed dose, D_{Rx}, of 54 Gy and 54 Gy-RBE (100) in photon and proton therapy, respectively.

4.3.3 Risk of mortality from SMNs

The lifetime attributable risk of mortality, LAR_T, for each SMNs was determined using previously-published methods (Taddei *et al* in manuscript preparation) that are briefly summarized below. For all solid cancer sites specific to *T* the linear-no-threshold model recommended by National Research Council of the National Academies (NRCNA) (4). Specifically,

$$\mathrm{LAR_T} = \frac{\mathrm{M_T}}{\mathrm{H_{ref}}}\mathrm{H_T}, \quad (1)$$

where M_T was the age- and sex-specific risk coefficient for mortality of *T* and H_{ref} was the reference equivalent dose. M_T was linearly interpolated between values in Table 12D-2 of the BEIR VII Report for H_{ref} = 0.1 Sv. This table lacked values for non-melanoma skin cancer (NMSC) and thyroid cancer. For M_{NMSC}, we applied sex- and age-averaged values from International Commission on Radiological Protection (ICRP) Publication 60 (48) that we also adjusted for sex and age following methods described previously (95). For $M_{thyroid}$, we derived $M_{thyroid}$ by multiplying the interpolated risk coefficients for incidence by a lethality factor of 0.1, recommended in ICRP Publication 60. $H_{remainder}$ was used to estimate the risk of other solid tumors.

To estimate $LAR_{leukemia}$ methods described by Taddei *et al* (in manuscript preparation) were implemented as well as recommendations by the NRCNA. The NRCNA recommended

using the no-threshold linear-quadratic model as a function of dose, $D + \theta D^2$, where θ was the degree of curvature equal to 0.88 Sv^{-1}. However, this model was developed on the basis of mostly low to moderate doses, i.e., 0 to 2 Gy. Therefore, for doses exceeding 2 Gy, modified linear-quadratic model was implemented to avoid overestimating $LAR_{leukemia}$ where H was high as described by Taddei *et al*. Their modified linear-quadratic model removed the quadratic term for which their equation for predicting $LAR_{leukemia}$ was,

$$\mathrm{LAR}_{\mathrm{leukemia}} = \begin{cases} \mathrm{M}_{\mathrm{leukemia}} \left(\frac{\mathrm{H}_{\mathrm{RBM}} + \theta \mathrm{H}_{\mathrm{RBM}}{}^2}{\mathrm{H}_{\mathrm{ref}} + \theta \mathrm{H}_{\mathrm{ref}}{}^2}\right), \text{ for } \mathrm{H}_{\mathrm{RBM}} \leq 2 \text{ Sv} \\ \mathrm{M}_{\mathrm{leukemia}} \left(50.7 + \frac{\mathrm{H}_{\mathrm{RBM}} - 2 \text{ Sv}}{\mathrm{H}_{\mathrm{ref}}}\right), \text{ for } \mathrm{H}_{\mathrm{RBM}} > 2 \text{ Sv} \end{cases} . \quad (2)$$

The BEIR VII and ICRP Publication 60 reports recommended applying dose and dose-rate effectiveness factors (DDREFs) to M_T. These DDREFs were implemented to account for a reduction in risk for low dose and low dose-rate exposures. In this study, the children's organs received high dose and fractionated or moderate dose rate exposures for which the recommended DDREFs were 2 for NMSC risk estimates (48) and 1.5 for all other solid tumor risk estimates (4). The DDREFs were not applied to $M_{leukemia}$ because it was already accounted for in the model. The final values for M_T used in this study are displayed in Table 12.

Table 12. Values for M_T (% per 0.1 Sv) for each patient in this study. Values were applied to the linear-no-threshold model for all cancer sites except leukemia, for which we applied a linear-quadratic model for H_{RBM} less than or equal to 2 Gy and linear model for H_{RBM} greater than 2 Sv.

Patient	**1**	**2**	**3**	**4**	**5**	**6**	**7**
Age	3.0	3.5	4.0	4.0	8.0	12.0	12.0
Sex	Female	Female	Female	Male	Male	Female	Male
SMN site	M_T **(%)**						
Stomach	0.052	0.051	0.050	0.035	0.032	0.038	0.028
Colon	0.092	0.091	0.089	0.144	0.126	0.069	0.110
Liver	0.022	0.021	0.021	0.038	0.033	0.016	0.029
Lung	0.578	0.567	0.556	0.275	0.237	0.412	0.204
Breast	0.238	0.232	0.226	-	-	0.152	-
Uterus	0.010	0.010	0.010	-	-	0.008	-
Ovary	0.050	0.049	0.049	-	-	0.037	-
Prostate	-	-	-	0.015	0.013	-	0.011
Bladder	0.054	0.053	0.053	0.039	0.034	0.040	0.030
Thyroid	0.051	0.048	0.046	0.008	0.006	0.024	0.004
NMSC	0.003	0.003	0.003	0.001	0.001	0.002	0.001
Other solid	0.369	0.348	0.328	0.284	0.222	0.204	0.185
Leukemia	0.052	0.052	0.052	0.071	0.071	0.053	0.071

The total lifetime risk of any SMN mortality, LAR_{total}, was determined using the following method to avoid attributing a fatality to multiple SMNs, the probability of surviving from all SMNs, S_{total}, was determined as

$$\mathrm{S_{total}} = \prod_{\mathrm{T}}(1 - \mathrm{LAR_T}). \quad (3)$$

LAR_{total} was then calculated as,

$$\mathrm{LAR_{total}} = 1 - \mathrm{S_{total}}. \quad (4)$$

This method assumed that the probability of surviving one cancer was independent of surviving the other cancers.

To compare the risk between proton and photon modalities, the ratio of *LAR*, *RLAR*, was calculated as

$$\mathrm{RLAR} = \frac{\mathrm{LAR(proton\ therapy)}}{\mathrm{LAR(photon\ therapy)}}, \quad (5)$$

for LAR_T and LAR_{total} resulting in $RLAR_T$ and $RLAR_{total}$, respectively. *RLAR* was used as a figure of merit to compare the modalities because of the lessened uncertainty than absolute risk (49,106,115–117). One-sided t-tests were performed using $RLAR_{total}$ to test whether proton therapy reduced the LAR_{total} compared to photon therapy (H_0: $RLAR_{total}=1$, H_A: $RLAR_{total}<1$, and $\alpha=0.05$). To convey the variation in the sample, one standard deviation of the mean was reported.

4.4 Results

4.4.1 Dosimetry

Values for H_T for photon and proton therapies are presented in Table 13 and Table 14, respectively, for each patient along with average values. For photon therapy, these data were from a previously-published study by Gallagher *et al* (manuscript 1 in preparation) except for the red bone marrow, skin, and remainder for which the treated volume was subtracted. The photon therapy treatment plans resulted in H_T of more than 0.8 Sv in the red bone marrow, remainder, skin, and thyroid. In proton therapy, only the red bone marrow, remainder, and skin received H_T of more than 0.8 Sv. H_T values ranging from 0.2 Sv to 0.8 Sv were observed in the breast tissue of the girls and the lungs of all children who received photon therapy. In proton therapy, only H_T in the thyroid fell into this interval.

Table 13. H_T (in Sv) for photon therapy for each patient along with the mean (Avg.) and standard deviation of the mean (St. dev.) averaged across all patients (Gallagher *et al* manuscript 1 in preparation).

Organs and tissues	3yof	3.5yof	4yof	4yom	8yom	12yof	12yom	Avg.	St. dev.
Bladder	0.017	0.027	0.021	0.060	0.014	0.013	0.019	0.024	0.016
Red bone marrow	3.500	2.825	5.682	4.495	6.400	3.204	1.087	3.885	1.802
Breast tissue	0.203	0.242	0.228	-	-	0.173	-	0.212	0.030
Liver	0.127	0.167	0.147	0.186	0.107	0.108	0.131	0.139	0.030
Lungs	0.188	0.239	0.210	0.300	0.197	0.205	0.229	0.224	0.038
Ovaries	0.016	0.027	0.060	-	-	0.013	-	0.029	0.022
Prostate	-	-	-	0.042	0.013	-	0.014	0.023	0.017
Remainder	2.643	1.767	1.710	3.072	1.380	1.069	1.072	1.816	0.772
Skin	1.613	0.892	1.114	1.302	0.518	0.644	0.497	0.940	0.424
Stomach	0.121	0.162	0.138	0.207	0.102	0.093	0.125	0.135	0.039
Thyroid	0.246	1.256	0.423	1.935	0.352	0.727	1.546	0.926	0.658
Uterus	0.016	0.027	0.021	-	-	0.013	-	0.019	0.006
Colon	0.065	0.092	0.076	0.129	0.039	0.038	0.052	0.070	0.032

Table 14. H_T (in Sv) for proton therapy for each patient along with the mean (Avg.) and standard deviation of the mean (St. dev.) averaged across all patients.

Organs and tissues	3yof	3.5yof	4yof	4yom	8yom	12yof	12yom	Avg.	St. dev.
Bladder	0.023	0.036	0.038	0.057	0.027	0.021	0.047	0.036	0.013
Red bone marrow	2.292	4.030	5.204	2.821	1.586	2.428	0.750	2.730	1.491
Breast tissue	0.093	0.187	0.162	-	-	0.132	-	0.143	0.040
Liver	0.059	0.115	0.101	0.123	0.075	0.092	0.118	0.098	0.024
Lungs	0.076	0.194	0.134	0.191	0.127	0.171	0.213	0.158	0.048
Ovaries	0.019	0.036	0.034	-	-	0.025	-	0.029	0.008
Prostate	-	-	-	0.050	0.024	-	0.046	0.040	0.014
Remainder	1.167	2.105	1.564	1.804	0.745	0.936	0.857	1.311	0.521
Skin	1.522	1.646	1.001	0.839	0.253	0.535	0.516	0.902	0.526
Stomach	0.055	0.104	0.094	0.111	0.062	0.081	0.106	0.088	0.022
Thyroid	0.155	0.346	0.302	0.252	0.251	0.631	0.422	0.337	0.154
Uterus	0.018	0.036	0.033	-	-	0.024	-	0.028	0.008
Colon	0.042	0.068	0.068	0.078	0.041	0.044	0.069	0.059	0.016

4.4.2 Risk prediction

Values of LAR_T and LAR_{total} for each patient are given for photon and proton therapies in Table 15

and Table 16, respectively. Additionally, the average LAR_T for photon and proton therapies are depicted in Figure 14. The cancer sites with the highest LAR_T were other solid tumors and leukemia, for which the average LAR_T values were 5.35 ± 3.11% and 3.98 ± 1.74%, respectively, for photon therapy and 3.86 ± 2.21% and 3.03 ± 1.21%, respectively, for proton therapy. For photon therapy, LAR_T values between 0.1% and 1% were found for fatal lung and thyroid cancer in each child and fatal breast cancer in the girls. In proton therapy, the same was true for fatal lung cancer in each child and fatal breast cancer in the girls. The average LAR_T for the remaining cancer sites were below 0.1% for both proton and photon therapies.

Values of LAR_{total} were compared in terms of sex and age. The average LAR_{total} values for the older children (i.e., 8 to 12 years old) were 6.94 ± 3.08% in photon therapy and 4.44 ± 1.43% in proton therapy. The average LAR_{total} of the younger children (i.e., 3 to 4 years old) were higher than those of the older children at 13.17± 1.72% for photon therapy and 10.16 ± 1.93% for proton therapy. In comparing between sexes, we did not observe a difference in the average LAR_{total} for photon therapy of the girls (11.15 ± 3.25%) and boys (9.64 ± 5.42%). However, there was a larger difference in the average LAR_{total} between the sexes in proton therapy, for which the average LAR_{total} values were 9.17 ± 2.93% and 5.76 ± 3.58% for girls and boys, respectively.

Table 15. LAR_T (%) for each radiogenic cancer site and LAR_{total} (%) of any fatal cancer displayed for photon therapy for each patient along with the means (Avg.) and standard deviations (St. dev.) averaged across all patients.

SMN site	3yof	3.5yof	4yof	4yom	8yom	12yof	12yom	Avg.	St. dev.
Bladder	0.01	0.01	0.01	0.02	0.00	0.01	0.01	0.01	0.01
Leukemia	3.44	3.08	4.57	5.37	6.72	3.30	1.38	3.98	1.74
Breast	0.48	0.56	0.52	-	-	0.26	-	0.46	0.13
Liver	0.03	0.04	0.03	0.07	0.04	0.02	0.04	0.04	0.02
Lung	1.09	1.36	1.17	0.82	0.47	0.85	0.47	0.89	0.34
Ovary	0.01	0.01	0.03	-	-	0.00	-	0.01	0.01
Prostate	-	-		0.01	0.00	-	0.00	0.00	0.00
Other solid cancers	9.74	6.15	5.61	8.72	3.06	2.18	1.98	5.35	3.11
NMSC	0.05	0.03	0.03	0.02	0.01	0.01	0.00	0.02	0.02
Stomach	0.06	0.08	0.07	0.07	0.03	0.04	0.03	0.06	0.02
Thyroid	0.12	0.61	0.20	0.16	0.02	0.17	0.07	0.19	0.19
Uterus	0.00	0.00	0.00	-	-	0.00	-	0.00	0.00
Colon	0.06	0.08	0.07	0.19	0.05	0.03	0.06	0.08	0.05
LAR_{total}	14.51	11.55	11.81	14.80	10.14	6.71	3.99	10.50	3.96

Table 16. LAR_T (%) for each radiogenic cancer site and LAR_{total} (%) of any fatal cancer are displayed for proton therapy for each patient along with the average (Avg.) and standard deviation (St. dev.) averaged across all patients.

SMN site	3yof	3.5yof	4yof	4yom	8yom	12yof	12yom	Avg.	St. dev.
Bladder	0.01	0.02	0.02	0.02	0.01	0.01	0.01	0.02	0.01
Leukemia	2.81	3.71	4.32	4.18	2.48	2.89	0.81	3.03	1.21
Breast	0.22	0.43	0.37	-	-	0.20	-	0.31	0.11
Liver	0.01	0.02	0.02	0.05	0.03	0.01	0.03	0.03	0.01
Lung	0.44	1.10	0.74	0.53	0.30	0.71	0.44	0.61	0.27
Ovary	0.01	0.02	0.02	-	-	0.01	-	0.01	0.00
Prostate	-	-	-	0.01	0.00	-	0.01	0.01	0.00
Other solid cancers	4.30	7.33	5.13	5.12	1.65	1.91	1.58	3.86	2.21
NMSC	0.05	0.05	0.03	0.01	0.00	0.01	0.01	0.02	0.02
Stomach	0.03	0.05	0.05	0.04	0.02	0.03	0.03	0.04	0.01
Thyroid	0.08	0.17	0.14	0.02	0.02	0.15	0.02	0.08	0.07
Uterus	0.00	0.00	0.00	0.00	0.00	0.00	0.00	0.00	0.00
Colon	0.04	0.06	0.06	0.11	0.05	0.03	0.08	0.06	0.03
LAR_{total}	7.81	12.48	10.53	9.81	4.50	5.84	2.98	7.71	3.45

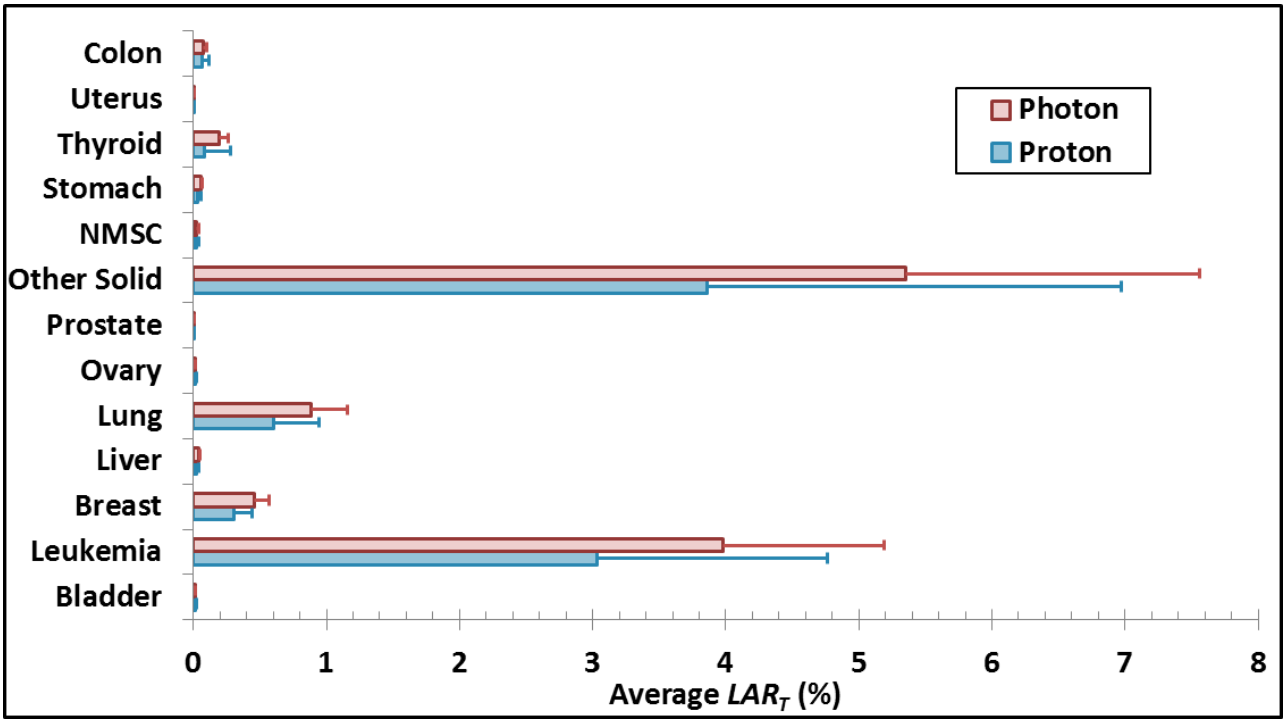

Figure 14. Mean LAR_T values for photon (red) and proton (blue) therapies for each cancer sites averaged across all patients. One-sided error bars signify one standard deviation of the mean.

The values for $RLAR_T$ and $RLAR_{total}$ are listed in Table 17. $RLAR_{total}$ was less than one for each patient except the 3.5-year-old girl, for whom $RLAR_{total}$ was 1.08. The mean $RLAR_T$ values, averaged across all seven patients, are shown for each T in Figure 15. The smallest mean $RLAR_T$ was 0.51 ± 0.28 for thyroid cancer. In general, the mean $RLAR_T$ was less than one for all cancer sites, with four expectations. These cancer sites consisted of bladder cancer in all the children, ovarian and uterus cancers in the girls, and prostate cancer in the boys. However, the absolute LAR_T values for these cancer sites were very small, i.e., less than 0.02%. In summary, $RLAR_{total}$ was 0.75 ± 0.22 for which the one-sided t-test resulted in the rejection of the null hypothesis (H_0: $RLAR_{total}$=1) with a p-value of 0.011.

Table 17. $RLAR_T$ values and and $RLAR_{total}$ for each patient along with the means (Avg.) and standard deviations of the means (St. dev.) averaged across all patients.

SMN site	3yof	3.5yof	4yof	4yom	8yom	12yof	12yom	Avg.	St. dev.
Bladder	1.36	1.32	1.79	0.96	1.98	1.70	2.45	1.65	0.49
Leukemia	0.82	1.20	0.95	0.78	0.37	0.88	0.59	0.80	0.27
Breast	0.46	0.77	0.71	-	-	0.76	-	0.68	0.15
Liver	0.47	0.69	0.69	0.66	0.70	0.85	0.90	0.71	0.14
Lung	0.40	0.81	0.64	0.64	0.65	0.83	0.93	0.70	0.17
Ovary	1.18	1.34	0.56	-	-	2.01	-	1.27	0.59
Prostate	-	-	-	1.20	1.90	-	3.20	2.10	1.01
Other solid cancers	0.44	1.19	0.91	0.59	0.54	0.88	0.80	0.76	0.26
NMSC	0.94	1.85	0.90	0.64	0.49	0.83	1.04	0.96	0.43
Stomach	0.46	0.64	0.68	0.54	0.60	0.86	0.85	0.66	0.15
Thyroid	0.63	0.28	0.71	0.13	0.71	0.87	0.27	0.51	0.28
Uterus	1.08	1.34	1.58	-	-	1.93	-	1.48	0.36
Colon	0.65	0.73	0.90	0.61	1.04	1.15	1.34	0.92	0.27
$RLAR_{total}$	0.54	1.08	0.89	0.66	0.44	0.87	0.75	0.75	0.22

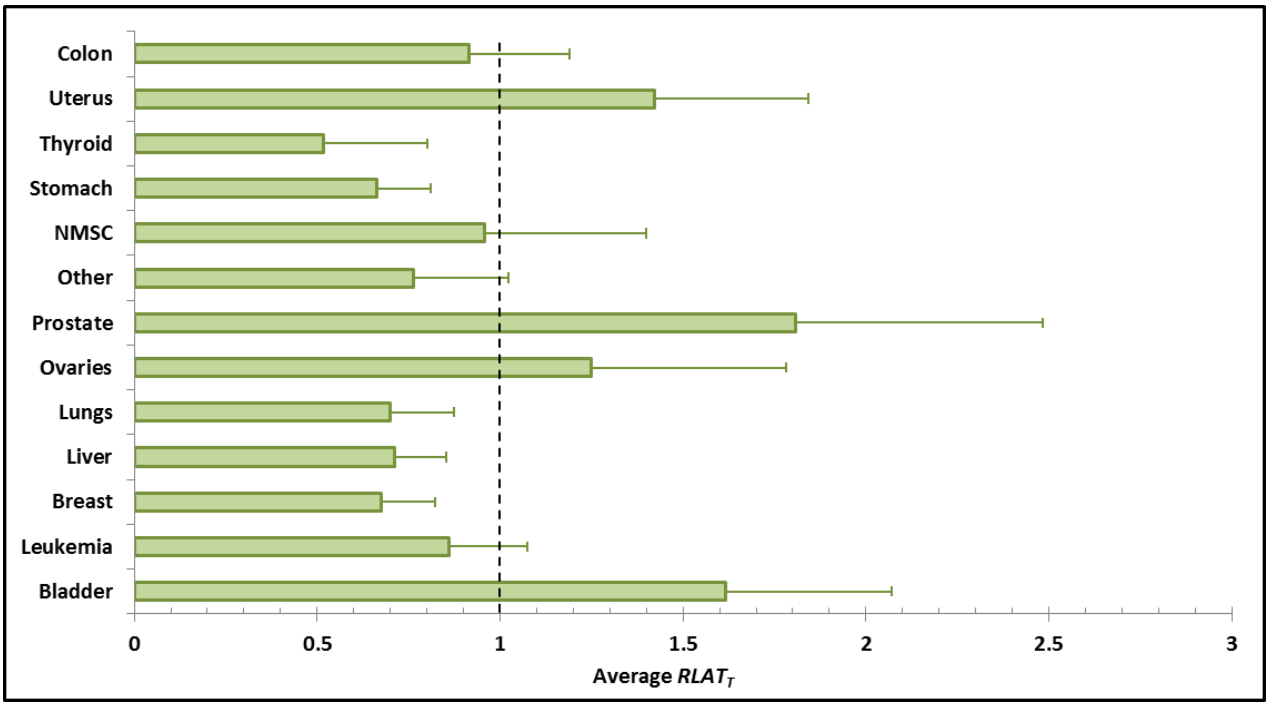

Figure 15. Mean $RLAR_T$ values for each cancer site averaged across all patients. One-sided error bars signify one standard deviation of the mean.

4.5 Discussion

In this *in silico* virtual clinical trial, we tested whether pediatric patients with intracranial tumors treated in a LMIC with photon therapy would have incurred a lesser risk of developing a fatal SMN had they been instead treated in a HIC with proton therapy. Our hypothesis that no significant difference would be observed was rejected. Specifically, our results showed that proton therapy was associated with 25% less risk than photon therapy for these children with intracranial tumors. The SMNs of greatest concern in both photon and proton therapies were leukemia and other solid tumors for which the $RLAR_T$ were 0.80 ± 0.27 and 0.76 ± 0.26, respectively. Therefore, if a regional proton therapy center were made available to these patients in the Middle East, then pediatric localized brain tumor patients would benefit.

The thyroid received the greatest relative benefit from proton therapy for which the predicted lifetime risk of a fatal SMN was reduced by 48%. Even though thyroid cancer risk was reduced considerably, the absolute reduction in the $LAR_{thyroid}$ for proton therapy was small because the lethality factor for thyroid cancer is low. Other cancer sites that received considerable reductions in LAR_T from proton therapy were other solid tumors (24%), leukemia (20%), and lung cancer (30%), which were the three primary contributors to LAR_{total}.

The risk projections in our study can be approximately compared to epidemiological studies. Although there have been no long-term follow-up studies for proton therapy, there have been several for photon therapy. First, Ron *et al* (24) observed 10,834 children treated with x-rays for tinea capitis with a mean age of 7.1 years and average follow-up of 26 years. They found that the relative risk of mortality from leukemia was 2.3. Using the baseline lifetime risk estimates for cancer reported in BEIR VII, this relative risk corresponded to an absolute risk of 1.43%, which was on the order of the average risk of fatal leukemia, 3.98%, projected in our study. One explanation for the higher predicted risk of leukemia in our study than their historical risk data was that the mean red bone marrow dose in their study was a factor of 100 smaller than in our study. Second, the Childhood Cancer Survivor Study reported a 3.7% incidence of fatality from a SMN after 30 years of follow-up in 2,881 patients under 21 years old who were initially treated for a CNS cancer (1). Of these children with a CNS cancer, 1,085 received radiation to the cranium for which 674 received only cranial fields with no spinal fields.

Although, some of the cohort received chemotherapy, Armstrong's analysis showed that chemotherapy was not a statistically significant source for the incidence of SMNs. In comparison to Armstrong's study we observed an average projected LAR_{total} of 10.50 ± 3.96% for the patients treated with photons. Differences could be attributed to the short follow-up where the risk of SMNs continues to increase over the patient's lifetime. Additionally, the CCSS cohort was older in age compared to the children in our study, and we found that younger children were at higher risk than older children. Direct comparison with epidemiological studies is difficult but the results in our study were generally in agreement with the literature.

The results of this study can be compared to a similar *in silico* study. Taddei *et al* (manuscript in preparation) projected the lifetime risk of fatality from SMNs for a cohort of nine pediatric patients who received either proton craniospinal irradiation (CSI) in a HIC or photon in a LMIC. They observed that proton therapy provided the most benefit for girls and younger patients. These trends were not clearly observed in this study due to the limited sample size. As a result, their LAR_{total} values of CSI (41.4% and 26.2% on average for photon and proton therapies, respectively) were approximately a factor of 3 to 4 larger than our averages for localized fields.

One of the novelties of our study was the method we used for estimating equivalent dose. For these patients for whom CT imaging extended only from the top of the head to the neck, we were able to estimate organ doses throughout their bodies. This demonstrated the feasibility of applying automated methods to computer codes that could attach to commercial proton and photon therapy TPSs to supplement the existing therapeutic doses with stray radiation dose estimates. Compared to Monte Carlo simulations, running analytical models would greatly reduce the computational expense of the estimates, allowing researchers and clinicians to routinely compare different modalities or optimize treatment plans to minimize long-term morbidities, for example, SMNs for pediatric patients. By extending the anatomies of the patients and applying these analytical models, we were able to estimate dose and predict risk for all radiogenic cancer sites throughout the children's bodies.

Our study had the following limitations. First, the target volume used for treatment planning for the 3.5-year-old girl was much larger for proton therapy compared to photon

therapy. It is notable that this was the only patient for whom $RLAR_{total}$ was not less than 1. The larger the target volume, the more integral dose is deposited. In addition, the expanded field edge put other organs and tissues in closer proximity, resulting in a higher dose in those organs and tissues. Second, the overall uncertainty for the projection of the lifetime risk of a fatal SMN was unknown and large. The uncertainty was attributable mainly to the risk model that we chose and not the physical dose calculation. Some sources of uncertainty in the risk model included the sampling variability in the model's parameter estimates, the transfer between populations (Japanese to American or Lebanese populations), DDREF, and the relevance of applying the model, which was based mainly on immediate low doses (i.e., less than 2 Gy), to fractionated high doses (i.e., more than 2 Sv) (4). Nonetheless, a systematic review of the epidemiology data by Berrington de Gonzalez *et al* (41) revealed that risk models derived from the Japanese atomic bomb survivor cohort were generally in agreement with carcinogenesis from fractionated high-dose exposures. As others have done previously, to minimize the effect of these uncertainties on our comparative study, we used the ratio of the risk projection to test our hypothesis.

In conclusion, our findings suggest that proton therapy in a HIC reduced the risk of a fatal SMN compared to photon therapy in a LMIC for pediatric patients with intracranial tumors. Our methods which use TPSs, analytical models, and supplemental phantoms to estimate the equivalent dose from therapeutic and stray radiation should enable more studies of this type as well as inform cancer survivors and their care team to understand and minimize long-term side-effects in childhood cancer survivors.

4.6 Acknowledgements

Funding was in part by the Fogarty International Center (award K01TW008409), the Naef K. Basile Cancer Institute, and the Portland Chapter of the Achievement Rewards for College Scientists. The content is solely the responsibility of the authors and does not necessarily represent the official views of the sponsors.

5.0 Discussion

In this dissertation we set out to address the hypothesis that for a sample set of seven pediatric patients with intracranial tumors proton therapy in a high-income country would not significantly reduce the risk of a fatal SMN compared to photon therapy in a low- to middle-income country. In performing a virtual clinical trial on seven pediatric patients, we found that proton therapy reduced the risk of a fatal SMN by 25%, and our hypothesis was invalidated. The cancer sites that were of greatest concern were leukemia and other solid tumors for which proton therapy reduced the risk of a fatal SMN by 20% and 24%, respectively.

We also demonstrated for the first time the use of analytical models to calculate internal and external neutrons in a cohort of patients receiving PSPT. Analytical models have the potential to reduce computational resources and time compared to Monte Carlo simulations. Additionally, a previously developed analytical model from the literature was used for photon therapy, allowing the dose and risk comparison between photon and proton therapies to be conducted without the use of Monte Carlo or a series of in-anthropomorphic phantom measurements. Furthermore, matched-computational phantoms were shown to effectively supplement missing out-of-field anatomy. In addition, the implementation of these phantoms has the potential to be automated. These methods, i.e., matched computationally phantoms combined with TPSs and analytical models to estimate therapeutic and stray radiation, have the potential to be developed such that full body dosimetry could be routinely performed in the clinic. Full body dosimetry in conjunction with long-term patient follow-up studies could lead to improvements in risk models and a better understanding of dose-response relationships. Additionally, full body dosimetry could be used to optimize treatment plans to minimize long-term side effects such as SMNs or compare different modalities.

Our neutron doses from PSPT may be compared to those of similar studies in the literature of pediatric patients with intracranial tumors. Zacharatou Jarlskog *et al* (44) calculated the treatment fields for a 9-year-old girl with an intracranial tumor onto a computational phantom representing an 8-year-old. They conducted Monte Carlo simulations to calculate equivalent dose from internal and external neutrons in the thyroid for several fields of varying

parameters. Field 7 was the most similar to our study, for which the equivalent dose in the thyroid was 0.16 mSv/Gy and 1.6 mSv/Gy from internal and external neutrons, respectively. For the 8-year-old boy in our study, the equivalent dose in the thyroid was 0.321 mSv/Gy and 4.79 mSv/Gy from internal and external neutrons, respectively. We can also compare our study to the Monte Carlo simulations by Matsumoto *et al* (22). They studied the total stray radiation from internal and external neutrons in a 5-year-old boy for whom they calculated 6.4 mSv/Gy in the thyroid. Similarly, the 4-year-old boy in our study received 5.13 mSv/Gy in the thyroid from both internal and external neutrons. In another study, Sayah *et al* (118) performed Monte Carlo simulations to study the total neutron equivalent dose in a 5-year-old girl for whom they calculated the total neutron equivalent dose to be 1.79 mSv/Gy in the thyroid. We calculated the total equivalent dose from internal and external neutrons in the 4-year-old girl to be 6.15 mSv/Gy in the thyroid. Overall, there were only slight deviations in neutron equivalent dose between these four studies.

The values for equivalent dose from neutrons between these four studies are close when considering the following. First, the external neutron production is heavily dependent on the treatment machine. Second, the internal neutron equivalent dose in the thyroid can vary considerably based on the proximity of the thyroid to the target volume as demonstrated in Manuscript 2. Third, the methods used to determine the radiation weighting factor varied between studies. Matsumoto *et al* determined the radiation weighting factor using the neutron spectrum impinging on the patient whereas Sayah *et al* and Zacharatou Jarlskog *et al* estimated the radiation weighting factor based on the neutron spectrum at each organ. The average radiation weighting factor calculated by Matsumoto *et al* was 11.34 whereas Sarah *et al* reported a radiation weighting factor varying between 4 and 10. In our study, the radiation weighting factor was 9.75 on average for external neutrons and 7.86 on average for internal neutrons. Similarity in methods contributes to the reason for our results more closely matching Matsumoto *et al*. Despite these variabilities, the neutron equivalent doses in our study were generally similar to the equivalent doses published in the literature.

The study that developed and applied the internal neutron model had several advantages. First, the model was inherently independent of proton facility, making it widely-

applicable. Second, the model was most accurate near the treatment field where the internal neutron doses were most meaningful for carcinogenesis and contributed to 25% of the total equivalent dose. For estimating low doses far from the treatment field the internal neutron model became less accurate. Third, the methods for developing this model may be applied to other treatment sites. Fourth, we demonstrated from previously-published Monte Carlo simulations for the intracranial fields of the 9-year-old girl that in the absence of external neutrons, internal neutrons became the major contributor to out-of-field equivalent dose. Specifically, internal neutrons accounted for 20% and 56% of the equivalent dose at 3 cm and 15 cm from the field edge, respectively. Excluding external neutrons generally approximates the case of PBSPT, for which internal neutrons become the major source of stray radiation as proton facilities transition to PBSPT. Given the wide applicability of this model, it would be of value for future studies to construct a library of models for various treatment sites and treatment parameters, e.g., nominal proton energy, SOBP, and aperture size. Another approach would be to generalize the model with additional parameters that take into account these factors.

Our validation of the external neutron analytical model also had several advantages. First, the studies from the literature for which the model and adjustment factors were based were of the same proton facility that the patients in this study received PSPT. Therefore, in the case of this study, the model was directly applicable to the cohort of children with intracranial tumors. Other strengths include that the combined use of all the adjustment factors applied to the analytical model achieved clinical realism and produced sufficient accuracy in the calculation of equivalent dose for both the girl and boy.

Some additional strengths of this study were that all cancer sites identified in the BEIR VII model were considered separately in the risk projection, and the risk of mortality was estimated instead of incidence. We considered estimating the risk of mortality as opposed to incidence as a strength because although the risk of incidence may be high for cancer sites such as NMSC or thyroid cancer, the survival rate is also high. Therefore, reporting a high risk of incidence could distract from the more meaningful results, i.e., those related to mortality or severe morbidity. To our knowledge, no other researchers have assessed the risk of mortality in pediatric patients with localized brain tumors. The risk of incidence has been researched but

not all cancer sites were investigated in those studies. For example, Athar and Paganetti (15) studied the risk of incidence but did not include cancer sites such as leukemia or other subsequent brain tumors, for which this dissertation has demonstrated to be of highest concern for pediatric survivors of localized brain tumors.

Another important strength of this dissertation was the physical location of the authors during the course of the study. The Department of Radiation Oncology at AUBMC graciously gave me the opportunity to study as a visiting research scientist for a total of 7 months. This allowed for a better understanding of the challenges that are faced by this particular institution in a LMIC. First of all, the radiation oncology staff was generally understaffed to manage its patient load. Attaining highly-specialized, educated and trained individuals is often difficult in LMICs. For example, no graduate program for medical physics exists in Lebanon. AUBMC has embraced this challenge by proposing a medical physics graduate program and recently starting a medical physics residency program. Resources were also limited. For instance, the service engineers in a HIC will generally stock various linear accelerator parts to minimize downtime. In LMICs, having back-up parts on-site is often limited. For many countries, a constant power supply is a challenge. Lebanon is one of those countries where daily scheduled power outages occur. To overcome this challenge, AUBMC uses its own generator. Although the challenges are many, AUBMC has impressively maintained its prominence as a premier research institution in the Middle East.

In addition to strengths, this study also had limitations. The limitations of this study included the uncertainty pertaining to the RBE of neutrons, and the high and unknown uncertainty in the risk model. The former uncertainty was addressed by using a conservative estimate of w_R as recommended by ICRP Publication 92 (108). The latter was addressed by using the ratio of the lifetime attributable risk of a fatal cancer to test our hypothesis. Other researchers have shown this to be an effective method to attain meaningful results for comparison studies (49,106,115–117). We also reported absolute risk to enhance our general understanding of the cancer sites of the greatest concern.

A source of error of this study was due to the difference in target volumes for proton and photon therapies. In general, the two therapies had different planning target volumes for

each patient due to the differing margins used to expand the clinical target volume to account for uncertainties in the respective treatments. To minimize this source of error and to avoid bias between the two modalities, we removed the 95% isodose volume (i.e., the treated volume) from the red bone marrow, remainder, and skin contours. This was done to eliminate the clinical target in the risk calculation and to avoid overestimation of the predicted risk. However, the target volumes of the 3.5-year-old girl varied considerably between the two therapies, for which the target volume in proton therapy volume was larger than the one used in photon therapy. This resulted in an overestimation of $RLAR_{total}$ for the girl. Despite this source of error, it did not impact our conclusions. If instead $RLAR_{total}$ for the 3.5-year-old girl was reduced to the average $RLAR_{total}$ of the rest of the cohort (i.e., 0.69), than the average $RLAR_{total}$ would have been 0.69 ± 0.14. Therefore, the conclusions of this study were unaltered by this source of error.

6.0 Conclusion

In our *in silico* clinical trial, we disproved our hypothesis that children treated with intracranial photon fields in low- to middle-income countries would not have a statistically-significant reduced risk of a fatal SMN if they were instead treated with intracranial proton fields. Additionally, the successful implementation of our methods indicated that applying supplemental anatomy and contours from generic computational phantoms and models of out-of-field dose may be used to determine organ doses in clinical and research radiotherapy studies when the actual patients' anatomies are not available. Furthermore, our methods demonstrated the feasibility of combining the algorithms of commercial TPSs with analytical models to quantify both therapeutic and stray radiation in proton and photon therapy. This ability introduces the possibility of quickly comparing different modalities or optimizing treatment plans to minimize long-term morbidities, such as SMNs. Notably, the internal neutron model we developed in this study was most accurate within 10 cm of the treatment fields, where the internal neutron dose contributed the most to overall exposures. Unlike the external neutron model, this model may be applied to any proton facility. Ongoing work includes programming the analytical models used in this study as add-ons for commercial TPSs and automating the fusion and matching process of the computational supplemental phantoms.

7.0 Bibliography

1. Armstrong, G. T. Long-term Survivors of Childhood Central Nervous System Malignancies: The Experience of the Childhood Cancer Survivor Study. *Eur. J. Paediatr. Neurol. EJPN Off. J. Eur. Paediatr. Neurol. Soc.* **14,** 298–303 (2010).

2. Siegel, R. & Jemal, A. *Cancer Facts & Figures 2014*. (The American Cancer Society, Inc., 2014).

3. Armstrong, G. T., Stovall, M. & Robison, L. L. Long-Term Effects of Radiation Exposure among Adult Survivors of Childhood Cancer: Results from the Childhood Cancer Survivor Study. *Radiat. Res.* **174,** 840–850 (2010).

4. NRCNA. *Health Risks from Exposure to Low Levels of Ionizing Radiation: BEIR VII Phase 2*. (National Academies Press, 2006).

5. ACS. *Global Cancer Facts & Figures*. (American Cancer Society, 2015).

6. Court, L. E. Evaluation of the dose calculation accuracy in intensity-modulated radiation therapy for mesothelioma, focusing on low doses to the contralateral lung. *J. Appl. Clin. Med. Phys.* **10,** (2009).

7. Howell, R. M., Scarboro, S. B., Kry, S. F. & Yaldo, D. Z. Accuracy of out-of-field dose calculations by a commercial treatment planning system. *Phys. Med. Biol.* **55,** 6999–7008 (2010).

8. Huang, J. Y., Followill, D. S., Wang, X. A. & Kry, S. F. Accuracy and sources of error of out-of field dose calculations by a commercial treatment planning system for intensity-modulated radiation therapy treatments. *J. Appl. Clin. Med. Phys. Am. Coll. Med. Phys.* **14,** 4139 (2013).

9. Jang, S. Y., Liu, H. H. & Mohan, R. Underestimation of Low-Dose Radiation in Treatment Planning of Intensity-Modulated Radiotherapy. *Int. J. Radiat. Oncol.* **71,** 1537–1546 (2008).

10. Joosten, A., Matzinger, O., Jeanneret-Sozzi, W., Bochud, F. & Moeckli, R. Evaluation of organ-specific peripheral doses after 2-dimensional, 3-dimensional and hybrid intensity modulated radiation therapy for breast cancer based on Monte Carlo and convolution/superposition algorithms: Implications for secondary cancer risk assessment. *Radiother. Oncol.* **106,** 33–41 (2013).

11. Taddei, P. J. *et al.* Analytical model for out-of-field dose in photon craniospinal irradiation. *Phys. Med. Biol.* **58,** 7463–7479 (2013).

12. Taylor, M. L. & Kron, T. Consideration of the radiation dose delivered away from the

treatment field to patients in radiotherapy. *J. Med. Phys. Assoc. Med. Phys. India* **36,** 59–71 (2011).

13. Taylor, M. L., Kron, T. & Franich, R. D. Assessment of Out-of-Field Doses in Radiotherapy of Brain Lesions in Children. *Int. J. Radiat. Oncol.* **79,** 927–933 (2011).

14. Agosteo, S., Birattari, C., Caravaggio, M., Silari, M. & Tosi, G. Secondary neutron and photon dose in proton therapy. *Radiother. Oncol.* **48,** 293–305 (1998).

15. Athar, B. S. & Paganetti, H. Comparison of second cancer risk due to out-of-field doses from 6-MV IMRT and proton therapy based on 6 pediatric patient treatment plans. *Radiother. Oncol. J. Eur. Soc. Ther. Radiol. Oncol.* **98,** 87–92 (2011).

16. Fontenot, J. *et al.* Equivalent dose and effective dose from stray radiation during passively scattered proton radiotherapy for prostate cancer. *Phys. Med. Biol.* **53,** 1677–1688 (2008).

17. Newhauser, W. D. *et al.* The risk of developing a second cancer after receiving craniospinal proton irradiation. *Phys. Med. Biol.* **54,** 2277–2291 (2009).

18. Taddei, P. J. *et al.* Reducing stray radiation dose to patients receiving passively scattered proton radiotherapy for prostate cancer. *Phys. Med. Biol.* **53,** 2131–2147 (2008).

19. Yan, X., Titt, U., Koehler, A. M. & Newhauser, W. D. Measurement of neutron dose equivalent to proton therapy patients outside of the proton radiation field. *Nucl. Instrum. Methods Phys. Res. Sect. Accel. Spectrometers Detect. Assoc. Equip.* **476,** 429–434 (2002).

20. Stovall, M. *et al.* Fetal dose from radiotherapy with photon beams: Report of AAPM Radiation Therapy Committee Task Group No. 36. *Med. Phys.* **22,** 63–82 (1995).

21. Pérez-Andújar, A., Newhauser, W. D. & Jr, P. M. D. Neutron production from beam-modifying devices in a modern double scattering proton therapy beam delivery system. *Phys. Med. Biol.* **54,** 993 (2009).

22. Matsumoto, S. *et al.* Secondary Neutron Doses to Pediatric Patients During Intracranial Proton Therapy: Monte Carlo Simulation of the Neutron Energy Spectrum and its Organ Doses. *Health Phys.* **110,** 380–386 (2016).

23. Turcotte, L. M. *et al.* Risk of Subsequent Neoplasms During the Fifth and Sixth Decades of Life in the Childhood Cancer Survivor Study Cohort. *J. Clin. Oncol. Off. J. Am. Soc. Clin. Oncol.* **33,** 3568–3575 (2015).

24. Ron, E., Modan, B. & Boice, J. D. Mortality after radiotherapy for ringworm of the scalp. *Am. J. Epidemiol.* **127,** 713–725 (1988).

25. Hall, E. J. Intensity-modulated radiation therapy, protons, and the risk of second cancers.

Int. J. Radiat. Oncol. **65,** 1–7 (2006).

26. Preston, D. L. *et al.* Effect of Recent Changes in Atomic Bomb Survivor Dosimetry on Cancer Mortality Risk Estimates. *Radiat. Res.* **162,** 377–389 (2004).

27. Brenner, D. J. *et al.* Cancer risks attributable to low doses of ionizing radiation: assessing what we really know. *Proc. Natl. Acad. Sci. U. S. A.* **100,** 13761–13766 (2003).

28. Sachs, R. K. & Brenner, D. J. Solid tumor risks after high doses of ionizing radiation. *Proc. Natl. Acad. Sci. U. S. A.* **102,** 13040–13045 (2005).

29. Sigurdson, A. J. *et al.* Primary thyroid cancer after a first tumour in childhood (the Childhood Cancer Survivor Study): a nested case-control study. *The Lancet* **365,** 2014–2023 (2005).

30. Diallo, I. *et al.* Frequency Distribution of Second Solid Cancer Locations in Relation to the Irradiated Volume Among 115 Patients Treated for Childhood Cancer. *Int. J. Radiat. Oncol.* **74,** 876–883 (2009).

31. Rheingold, S., Neugut, A. & Meadows, A. *Therapy-Related Secondary Cancers*. (2003).

32. Preston, D. L., Shimizu, Y., Pierce, D. A., Suyama, A. & Mabuchi, K. Studies of Mortality of Atomic Bomb Survivors. Report 13: Solid Cancer and Noncancer Disease Mortality: 1950–1997. *Radiat. Res.* **160,** 381–407 (2003).

33. Hall, E. J. Henry S. Kaplan Distinguished Scientist Award 2003. The crooked shall be made straight; dose-response relationships for carcinogenesis. *Int. J. Radiat. Biol.* **80,** 327–337 (2004).

34. Curtis, R. E. *et al.* Relationship of leukemia risk to radiation dose following cancer of the uterine corpus. *J. Natl. Cancer Inst.* **86,** 1315–1324 (1994).

35. Little, M. P. *et al.* Risks of leukemia in Japanese atomic bomb survivors, in women treated for cervical cancer, and in patients treated for ankylosing spondylitis. *Radiat. Res.* **152,** 280–292 (1999).

36. Boice, J. D. *et al.* Radiation dose and leukemia risk in patients treated for cancer of the cervix. *J. Natl. Cancer Inst.* **79,** 1295–1311 (1987).

37. Hawkins, M. M. *et al.* Epipodophyllotoxins, alkylating agents, and radiation and risk of secondary leukaemia after childhood cancer. *BMJ* **304,** 951–958 (1992).

38. Neglia, J. P. *et al.* New Primary Neoplasms of the Central Nervous System in Survivors of Childhood Cancer: a Report From the Childhood Cancer Survivor Study. *J. Natl. Cancer Inst.* **98,** 1528–1537 (2006).

39. Inskip, P. D. *et al.* Radiation Dose and Breast Cancer Risk in the Childhood Cancer Survivor Study. *J. Clin. Oncol.* **27,** 3901–3907 (2009).

40. Tucker, M. A. *et al.* Bone Sarcomas Linked to Radiotherapy and Chemotherapy in Children. *N. Engl. J. Med.* **317,** 588–593 (1987).

41. Berrington de Gonzalez, A. B. *et al.* Second solid cancers after radiotherapy: a systematic review of the epidemiological studies of the radiation dose-response relationship. *Int. J. Radiat. Oncol. Biol. Phys.* **86,** (2013).

42. Athar, B. S. & Paganetti, H. Neutron equivalent doses and associated lifetime cancer incidence risks for head & neck and spinal proton therapy. *Phys. Med. Biol.* **54,** 4907 (2009).

43. Athar, B. S., Bednarz, B., Seco, J., Hancox, C. & Paganetti, H. Comparison of out-of-field photon doses in 6 MV IMRT and neutron doses in proton therapy for adult and pediatric patients. *Phys. Med. Biol.* **55,** 2879–2891 (2010).

44. Zacharatou Jarlskog, C., Lee, C., Bolch, W. E., Xu, X. G. & Paganetti, H. Assessment of organ specific neutron equivalent doses in proton therapy using computational whole-body age-dependent voxel phantoms. *Phys. Med. Biol.* **53,** 693–717 (2008).

45. Lee, C., Williams, J. L., Lee, C. & Bolch, W. E. The UF series of tomographic computational phantoms of pediatric patients. *Med. Phys.* **32,** 3537–3548 (2005).

46. Xu, X. G., Chao, T. C. & Bozkurt, A. VIP-Man: an image-based whole-body adult male model constructed from color photographs of the Visible Human Project for multi-particle Monte Carlo calculations. *Health Phys.* **78,** 476–486 (2000).

47. Hall, E. J. & Wuu, C.-S. Radiation-induced second cancers: the impact of 3D-CRT and IMRT. *Int. J. Radiat. Oncol.* **56,** 83–88 (2003).

48. ICRP. 1990 Recommendations of the International Commission on Radiological Protection: ICRP Publication 60. *Ann ICRP* **21,** (1991).

49. Moteabbed, M., Yock, T. I. & Paganetti, H. The risk of radiation-induced second cancers in the high to medium dose region: a comparison between passive and scanned proton therapy, IMRT and VMAT for pediatric patients with brain tumors. *Phys. Med. Biol.* **59,** 2883 (2014).

50. Paganetti, H. *et al.* Assessment of radiation-induced second cancer risks in proton therapy and IMRT for organs inside the primary radiation field. *Phys. Med. Biol.* **57,** 6047 (2012).

51. Winkfield, K. M. *et al.* Modeling intracranial second tumor risk and estimates of clinical toxicity with various radiation therapy techniques for patients with pituitary adenoma.

Technol. Cancer Res. Treat. **10,** 243–251 (2011).

52. Schneider, U., Zwahlen, D., Ross, D. & Kaser-Hotz, B. Estimation of radiation-induced cancer from three-dimensional dose distributions: Concept of organ equivalent dose. *Int. J. Radiat. Oncol.* **61,** 1510–1515 (2005).

53. Arvold, N. D. *et al.* Projected Second Tumor Risk and Dose to Neurocognitive Structures After Proton Versus Photon Radiotherapy for Benign Meningioma. *Int. J. Radiat. Oncol.* **83,** e495–e500 (2012).

54. Dennis, E. R. *et al.* A comparison of critical structure dose and toxicity risks in patients with low grade gliomas treated with IMRT versus proton radiation therapy. *Technol. Cancer Res. Treat.* **12,** 1–9 (2013).

55. Miralbell, R., Lomax, A., Cella, L. & Schneider, U. Potential reduction of the incidence of radiation-induced second cancers by using proton beams in the treatment of pediatric tumors. *Int. J. Radiat. Oncol.* **54,** 824–829 (2002).

56. Armoogum, K. S. & Thorp, N. Dosimetric Comparison and Potential for Improved Clinical Outcomes of Paediatric CNS Patients Treated with Protons or IMRT. *Cancers* **7,** 706–722 (2015).

57. Schneider, C., Newhauser, W. & Farah, J. An Analytical Model of Leakage Neutron Equivalent Dose for Passively-Scattered Proton Radiotherapy and Validation with Measurements. *Cancers* **7,** 795–810 (2015).

58. Armstrong, G. T. *et al.* Late Mortality Among 5-Year Survivors of Childhood Cancer: A Summary From the Childhood Cancer Survivor Study. *J. Clin. Oncol.* **27,** 2328–2338 (2009).

59. Hasenbalg, F., Neuenschwander, H., Mini, R. & Born, E. J. Collapsed cone and analytical anisotropic algorithm dose calculations compared to VMC++ Monte Carlo simulations in clinical cases. *J. Phys. Conf. Ser.* **74,** 021007 (2007).

60. Stovall, M. *et al.* Dose Reconstruction for Therapeutic and Diagnostic Radiation Exposures: Use in Epidemiological Studies. *Radiat. Res.* **166,** 141–157 (2006).

61. Kry, S. F. *et al.* A Monte Carlo model for calculating out-of-field dose from a varian 6 MV beam. *Med. Phys.* **33,** 4405–4413 (2006).

62. Kry, S. F. *et al.* A Monte Carlo model for out-of-field dose calculation from high-energy photon therapy. *Med. Phys.* **34,** 3489–3499 (2007).

63. Lehmann, J. *et al.* Dosimetry for quantitative analysis of the effects of low-dose ionizing radiation in radiation therapy patients. *Radiat. Res.* **165,** 240–247 (2006).

64. Rijkee, A. G., Zoetelief, J., Raaijmakers, C. P. J., Marck, S. C. V. D. & Zee, W. V. D. Assessment of induction of secondary tumours due to various radiotherapy modalities. *Radiat. Prot. Dosimetry* **118,** 219–226 (2006).

65. Bednarz, B. & Xu, X. G. Monte Carlo modeling of a 6 and 18 MV Varian Clinac medical accelerator for in-field and out-of-field dose calculations: development and validation. *Phys. Med. Biol.* **54,** N43–N57 (2009).

66. Joosten, A. *et al.* Variability of a peripheral dose among various linac geometries for second cancer risk assessment. *Phys. Med. Biol.* **56,** 5131 (2011).

67. Chofor, N., Harder, D., Willborn, K. C. & Poppe, B. Internal scatter, the unavoidable major component of the peripheral dose in photon-beam radiotherapy. *Phys. Med. Biol.* **57,** 1733 (2012).

68. Francois, P., Beurtheret, C. & Dutreix, A. Calculation of the dose delivered to organs outside the radiation beams. *Med. Phys.* **15,** 879–883 (1988).

69. Benadjaoud, M. A. *et al.* A multi-plane source model for out-of-field head scatter dose calculations in external beam photon therapy. *Phys. Med. Biol.* **57,** 7725 (2012).

70. Bezin, J. V. *et al.* Field size dependent mapping of medical linear accelerator radiation leakage. *Phys. Med. Biol.* **60,** 2103 (2015).

71. Jagetic, L. J. & Newhauser, W. D. A simple and fast physics-based analytical method to calculate therapeutic and stray doses from external beam, megavoltage x-ray therapy. *Phys. Med. Biol.* **60,** 4753 (2015).

72. Stovall, M., Smith, S. A. & Rosenstein, M. Tissue doses from radiotherapy of cancer of the uterine cervix. *Med. Phys.* **16,** 726–733 (1989).

73. Stovall, M. *et al.* Genetic effects of radiotherapy for childhood cancer: Gonadal dose reconstruction. *Int. J. Radiat. Oncol.* **60,** 542–552 (2004).

74. Taddei, P. J. *et al.* Inter-Institutional Comparison of Personalized Risk Assessments for Second Malignant Neoplasms for a 13-Year-Old Girl Receiving Proton versus Photon Craniospinal Irradiation. *Cancers* **7,** 407–426 (2015).

75. Taddei, P. *et al.* Potential of proton therapy to lessen subsequent cancer risk for survivors of childhood medulloblastoma in low- and middle-income countries (Manuscript in Preparation). (2017).

76. Lunsford, T. & Lunsford, B. The Research Sample, Part I: Sampling. *Journal of Prosthetics and Orthotics* (1995).

77. Merchant, T. E., Haida, T., Wang, M.-H., Finlay, J. & Leibel, S. Anaplastic ependymoma:

treatment of pediatric patients with or without craniospinal radiation therapy. *J Neurosurg* **86,** 943–949 (1997).

78. Ahnesjö, A. Collapsed cone convolution of radiant energy for photon dose calculation in heterogeneous media. *Med. Phys.* **16,** 577–592 (1989).

79. Kessler, M. L. Image registration and data fusion in radiation therapy. *Br. J. Radiol.* **79 Spec No 1,** S99-108 (2006).

80. ICRU. *Dose Specification for Reporting External Beam Therapy with Photons and Electrons*. (International Commission on Radiation Units and Measurements, 1978).

81. CIRS. *ATOM® Dosimetry Phantoms: Models 700 – 705*. (Computerized Imaging Reference Systems, Inc., 2010).

82. Kry, S. F., Price, M., Followill, D., Mourtada, F. & Salehpour, M. The use of LiF (TLD-100) as an out-of-field dosimeter. *J. Appl. Clin. Med. Phys. Am. Coll. Med. Phys.* **8,** 2679 (2007).

83. Scarboro, S. B., Followill, D. S., Howell, R. M. & Kry, S. F. Variations in photon energy spectra of a 6 MV beam and their impact on TLD response. *Med. Phys.* **38,** 2619–2628 (2011).

84. ICRP. *ICRP Publication 103: Recommendations of the International Commission on Radiological Protection*. (2007).

85. NCRP. *National Council on Radiation Protection and Measurements Report No. 126: Uncertainties in fatal cancer risk estimates used in radiation*. (1997).

86. Xu, X. G., Bednarz, B. & Paganetti, H. A review of dosimetry studies on external-beam radiation treatment with respect to second cancer induction. *Phys. Med. Biol.* **53,** R193–R241 (2008).

87. Newhauser, W. *et al.* Anonymization of DICOM electronic medical records for radiation therapy. *Comput. Biol. Med.* **53,** 134–140 (2014).

88. Cristy, M. Active bone marrow distribution as a function of age in humans. *Phys. Med. Biol.* **26,** 389–400 (1981).

89. Brenner, D. J. Effective dose: a flawed concept that could and should be replaced. *Br. J. Radiol.* **81,** 521–523 (2008).

90. Jermann, M. Patient statistics per end of 2015. *Particle Therapy Co-Operative Group* (2016). Available at: https://www.ptcog.ch/index.php/patient-statistics. (Accessed: 25th April 2017)

91. Chang, A. L. *et al.* Pediatric Proton Therapy: Patterns of Care across the United States. *Int.*

J. Part. Ther. **1,** 357–367 (2014).

92. Brenner, D. J., Curtis, R. E., Hall, E. J. & Ron, E. Second malignancies in prostate carcinoma patients after radiotherapy compared with surgery. *Cancer* **88,** 398–406 (2000).

93. Newhauser, W. D. & Durante, M. Assessing the risk of second malignancies after modern radiotherapy. *Nat. Rev. Cancer* **11,** 438–448 (2011).

94. Geng, C. *et al.* Assessing the radiation-induced second cancer risk in proton therapy for pediatric brain tumors: the impact of employing a patient-specific aperture in pencil beam scanning. *Phys. Med. Biol.* **61,** 12–22 (2015).

95. Taddei, P. J. *et al.* Predicted risks of second malignant neoplasm incidence and mortality due to secondary neutrons in a girl and boy receiving proton craniospinal irradiation. *Phys. Med. Biol.* **55,** 7067–7080 (2010).

96. Taddei, P. J. *et al.* Stray radiation dose and second cancer risk for a pediatric patient receiving craniospinal irradiation with proton beams. *Phys. Med. Biol.* **54,** 2259–2275 (2009).

97. Eley, J. *et al.* Implementation of an Analytical Model for Leakage Neutron Equivalent Dose in a Proton Radiotherapy Planning System. *Cancers* **7,** 427–438 (2015).

98. Pérez-Andújar, A., Zhang, R. & Newhauser, W. Monte Carlo and analytical model predictions of leakage neutron exposures from passively scattered proton therapy. *Med. Phys.* **40,** (2013).

99. Zhang, R., Pérez-Andújar, A., Fontenot, J. D., Taddei, P. J. & Newhauser, W. D. An analytic model of neutron ambient dose equivalent and equivalent dose for proton radiotherapy. *Phys. Med. Biol.* **55,** 6975–6985 (2010).

100. ICRU. *ICRU Report 78: Prescribing, Recording, and Reporting Proton-Beam Therapy*. (International Commission on Radiation Units and Measurements, Inc., 2007).

101. Grahn, D., Lombard, L. S. & Carnes, B. A. The comparative tumorigenic effects of fission neutrons and cobalt-60 gamma rays in the B6CF1 mouse. *Radiat. Res.* **129,** 19–36 (1992).

102. Wolf, C., Lafuma, J., Masse, R., Morin, M. & Kellerer, A. M. Neutron RBE for Induction of Tumors with High Lethality in Sprague-Dawley Rats. *Radiat. Res.* **154,** 412–420 (2000).

103. Hollander, C. F., Zurcher, C. & Broerse, J. J. Tumorigenesis in high-dose total body irradiated rhesus monkeys--a life span study. *Toxicol. Pathol.* **31,** 209–213 (2003).

104. Kuhne, W. W. *et al.* Biological effects of high-energy neutrons measured in vivo using a vertebrate model. *Radiat. Res.* **172,** 473–480 (2009).

105. Brenner, D. J., Elliston, C. D., Hall, E. J. & Paganetti, H. Reduction of the secondary neutron dose in passively scattered proton radiotherapy, using an optimized pre-collimator/collimator. *Phys. Med. Biol.* **54,** 6065–6078 (2009).

106. Zhang, R. Quantitative comparison of late effects following photon versus proton external-beam radiation therapies: Toward an evidence-based approach to selecting a treatment modality. (The University of Texas Health Science Center at Houston Graduate School of Biomedical Sciences, 2011).

107. Pelowitz, D. *MCNPX User's Manual*. (Los Alamos National Lab, 2008).

108. ICRP. *ICRP Publication 92: Relative Biological Effectiveness (RBE), Quality Factor (Q), and Radiation Weighting Factor (Wr)*. (2003).

109. Zheng, Y., Newhauser, W., Fontenot, J., Taddei, P. & Mohan, R. Monte Carlo study of neutron dose equivalent during passive scattering proton therapy. *Phys. Med. Biol.* **52,** 4481–4496 (2007).

110. Zheng, Y., Fontenot, J., Taddei, P., Mirkovic, D. & Newhauser, W. Monte Carlo simulations of neutron spectral fluence, radiation weighting factor and ambient dose equivalent for a passively scattered proton therapy unit. *Phys. Med. Biol.* **53,** 187–201 (2008).

111. Wroe, A., Rosenfeld, A. & Schulte, R. Out-of-field dose equivalents delivered by proton therapy of prostate cancer. *Med. Phys.* **34,** 3449–3456 (2007).

112. Howell, R. M. & Burgett, E. A. Secondary neutron spectrum from 250-MeV passively scattered proton therapy: Measurement with an extended-range Bonner sphere system. *Med. Phys.* **41,** (2014).

113. ICRU. *ICRU Report 50: Prescribing, Recording, and Reporting Photon Beam Therapy*. (International Commission on Radiation Units and Measurements, Inc., 1993).

114. ICRU. *ICRU Report 49: Stopping Powers and Ranges for Protons and Alpha Particles*. (International Commission on Radiation Units and Measurements, Inc., 1993).

115. Nguyen, J., Moteabbed, M. & Paganetti, H. Assessment of uncertainties in radiation-induced cancer risk predictions at clinically relevant doses. *Med. Phys.* **42,** 81–89 (2015).

116. Fontenot, J. D., Bloch, C., Followill, D., Titt, U. & Newhauser, W. D. Estimate of the uncertainties in the relative risk of secondary malignant neoplasms following proton therapy and intensity-modulated photon therapy. *Phys. Med. Biol.* **55,** 6987–6998 (2010).

117. Kry, S. F. *et al.* Uncertainty of Calculated Risk Estimates for Secondary Malignancies After Radiotherapy. *Int. J. Radiat. Oncol.* **68,** 1265–1271 (2007).

118. Sayah, R. *et al.* Secondary neutron doses received by paediatric patients during

intracranial proton therapy treatments. *J. Radiol. Prot.* **34,** 279–296 (2014).